INTERCONNECT GEOMETRIC EFFECT ON PERFORMANCE OF SOLID OXIDE FUEL CELLS (SOFCS) RUNNING ON ALTERNATIVE FUELS

SUN QIONG

Ph.D

The Hong Kong Polytechnic University

2017

The Hong Kong Polytechnic University

Department of Building and Real Estate

Interconnect Geometric Effect on Performance of Solid Oxide Fuel Cells (SOFCs) Running on Alternative Fuels

SUN Qiong

A thesis submitted in partial fulfillment of the requirements for the degree of Doctor of Philosophy

August 2016

CERTIFICATE OF ORIGINALITY

I hereby declare that this thesis is my own work and that, to the best of my knowledge and belief, it reproduces no material previously published or written, nor material that has been accepted for the award of any other degree or diploma, except where due acknowledgement has been made in the text.

_____ (Signed)

_____ SUN_Qiong _____ (Name of student)

ABSTRACT

SOFC is attracting intensive attention in the area of clean energy conversion due to its high efficiency and environment-friendliness. The development of SOFCs stack is the key to commercialize SOFCs technology since single SOFCs must be connected into a stack to achieve a practical output voltage and high energy density for real applications. In a traditional planar type SOFC stack, the interconnect is an important component as it serves for several crucial functions, including collecting current, gas sealing and structurally forming flow channels for uniform gas distribution. The ribs of interconnect are defined as the part that separate any two neighboring fuel channels (or air channels at the cathode side). Due to the existence of interconnect ribs, the gas diffusion path and electron conducting path are strongly dependent on the interconnect rib width. As a result, the stack performance is sensitive to the interconnect rib width as the concentration loss and ohmic loss largely depend on the gas diffusion path and electron conducting path, respectively. However, there is dilemma in designing the value of interconnect rib width for the sake that concentration loss and ohmic loss are oppositely correlated to the width value: a smaller rib width is desired to reduce the concentration loss by shortening the gas diffusion path, while a larger

rib width is preferred to decrease the ohmic loss by shortening the electron conducting path and increasing the contact area of interconnect rib and electrode. Therefore, there should be an optimum interconnect rib width value for the overall performance of SOFC stack.

By reviewing literatures on geometrical optimization of planar SOFC stack by modeling, heat transfer is mostly neglected which could lead to inaccurate modeling results and misleading optimization suggestions, especially in the case of H_2 fed planar SOFC stack, of which the maximum temperature difference can reach 100K along the gas channels. The stack performance is vulnerable to such large temperature difference in terms of overwhelming thermal stress, material compatibility and durability. Thus, it is necessary to incorporate the heat transfer into the modeling of SOFC stack. Based on the previous models, a comprehensive three-dimensional (3D) model of a unit cell of planar SOFC stack is further developed, considering electrons and ions conducting, electrochemical reactions, chemical reactions, gas transport and heat transfer. This 3D model is used to investigate the optimum interconnect rib width by series of parametric studies. A dimensionless variable, Ra, defined as the ratio of interconnect rib width to the width of the whole unit cell, is proposed to characterize the rib geometry, which is an easy-to-use parameter for practical stack geometric design.

In addition, to generalize the results of optimum Ra, the SOFC stack fed with three different usual fuels (hydrogen, syngas and methane) are also modeled. Model validation is firstly conducted on the single cell level, and further validated in H_2 fed stack case, by the comparison of optimum Ra between the current model and other researcher's simulation works under the isothermal assumption.

For the planar SOFC stack fed by three different fuels, the relations between the optimum Ra and main factors (pitch width, cathode porosity, ASR) are found to be similar. Considering the large difference between fuel diffusion coefficient and oxygen diffusion coefficient in H_2 fed planar SOFC stack, an asymmetric design for the interconnect rib is proposed and the optimum anode Ra (Ra_a^{asym}) and optimum anode Ra (Ra_c^{asym}) are accordingly obtained. The simulated stack performance indicates that the SOFC stack benefits significantly from this novel asymmetric design. This asymmetric design is also applied in syngas or methane fed SOFC stack. However, there is only slight increase in stack performance when optimum asymmetric design is adopted in SOFC fed by syngas or by methane with internal reforming. Followed by parametric studies, empirical equations are derived to predict the optimum Ra of planar stack, which is a constructive guideline for practical geometric design of SOFC stack.

It is confirmed by experiments that CO electrochemical oxidation also occurs in H_2- H_2O-CO-CO_2 gas mixture system, therefore, it is unclear whether SOFC with proton ions conducting electrolyte (H-SOFC) is better than SOFC with oxygen ion conducting electrolyte (O-SOFC) in terms of maximum thermodynamic efficiency since CO electrochemical oxidation occurs in anode side of O-SOFC. In the later part of this thesis, a thermal dynamic study is conducted to investigate the effects of CO electrochemical oxidation on cell performance. It is shown that the maximum efficiency of H-SOFC is higher than that of O-SOFC when CO electrochemical reaction in O-SOFC is neglected, which is identical to the results in the previous literature. However, when CO electrochemical reaction in O-SOFC is involved, O-SOFC has higher maximum efficiency than H-SOFC.

LIST OF PUBLICATIONS

1. **Sun, Q.**, Zheng, K., & Ni, M. (2014). Thermodynamic analysis of methane-fueled solid oxide fuel cells considering CO electrochemical oxidation. Chinese Journal of Chemical Engineering, 22(9), 1033-1037.
2. **Sun, Q.**, Zheng, K., & Ni, M,. 3D modeling of internal reforming SOFC with a focus on the interconnector size effect. (poster, the 5th International Conference on "Fundamentals & Development of Fuel Cells", in Karlsruhe, Germany, April 16-18, 2013)
3. **Sun, Q.** & Ni, M.(2015). Three-dimensional Modeling of Internal Reforming SOFC with a Focus on the Interconnect Size Effect. ECS Transactions, 68 (1) 2317-2338.
4. **Sun, .Q.** &Ni, M. Three-dimensional modeling of hydrogen fed SOFC stacks with a focus on the optimal interconnect rib size. (oral presentation, 2016 Asian SOFC symposium, in Tokyo, Japan, September 4-7, 2016)
5. Yanxiang Zhang, **Qiong Sun**, Changrong Xia & Meng Ni (2013). Geometric Properties of Nanostructured Solid Oxide Fuel Cell Electrodes. Journal of The Electrochemical Society, 160(3), F278-F289.
6. Zheng, K., **Sun, Q.**, & Ni, M. (2013). Local non-equilibrium thermal

effects in solid oxide fuel cells with various fuels. Energy Technology, 1(1), 35-41.

7. Zheng, K., Ni, M., **Sun, Q.**, & Shen, L. (2013). Mathematical analysis of SOFC based on co-ionic conducting electrolyte. Acta Mechanica Sinica, 29(3), 388-394.
8. Zheng, K., Ni, M, & **Sun, Q.**. A detailed comparison of mass transport models for predicting concentration overpotential of SOFC electrodes. (oral presentation, the 5th International Conference on "Fundamentals & Development of Fuel Cells", in Karlsruhe, Germany, April 16-18, 2013)

ACKNOWLEDGEMENTS

I would like to take this opportunity to give my sincere thanks from the bottom of my heart to all the people who helped me and contributed to my PhD study.

Firstly, I sincerely thank my supervisor, Prof. NI Meng, for his consistent guidance and encouragement through the past five years. I am strongly inspirited by his research attitude and great personality. I always feel grateful for being a PhD student of my supervisor. Thanks are also extended to my co-supervisor, Prof. SHEN Liyin for his kind help in my study. I also sincerely appreciate Dr. Kevin Huang from University of South Carolina for providing me the opportunity to be an exchange student in University of South Carolina.

I also thank all the members in our research group for their selfless helps. Discussions with them inspired me a lot in my research. I also would like to express my sincere gratitude to Dr. Zhang Yanxiang for his great help at the very beginning of my PhD study and during my stay in University of South Carolina. Special thanks are given to Dr. Zheng Keqing for the help in proofreading and suggestions for this thesis. Also, I would like to thank Mr. Chen Bin for the discussions and suggestions in building models. I am also thankful for sharing all the memories, no matter good or bad, with colleagues and friends in Rooms

W606, ZN708 and ZN710.

Last but not least, I would like to thank my family. Without their understanding, encouragement and everlasting support, I definitely could not finish my study.

TABLE OF CONTENTS

LIST OF FIGURES

LIST OF TABLES

LIST OF ABBREVIATIONS

SOFC	solid oxide fuel cell
L	length
W	width
H	height
Ra_a	ratio of the anode interconnect rib width to the unit cell width
Ra_c	ratio of the cathode interconnect rib width to the unit cell width
E	voltage
G	Gibbs free energy
R	ideal gas constant, 8.3145 J mol^{-1} K^{-1}
T	temperature
n	number of electrons involved per electrochemical reaction
F	Faraday constant, 96485 C mol^{-1}
p	gas pressure
s	entropy
S_v	active specific area per electrode volume
i_0	exchange current density
k_e	pre-exponential factor

E_{act}	activation energy
r_{e}	radius of the electronic conductors
n_{t}	total number of particles per unit volume
n_{e}	number fractions of electronic conductor
n_{i}	number fractions of ionic conductor
Z_{e}	coordination numbers of electronic conductor
Z_{i}	coordination numbers of ionic conductor
P_{e}	probability of electronic conductors connected with porous media
P_{i}	probability of ionic conductors connected with porous media
ASR	area specific resistance
$\vec{F}$	vector of the volume force
ρ	density
$\vec{V}$	velocity vector
S_{m}	mass source
B_{p}	permeability coefficient of the porous electrodes
$\vec{J_{\mathrm{i}}}$	flux of gas diffusion of species i in the porous media
y_{i}	molar fraction of species i
w_{i}	mass fraction of species i
S_{i}	source term of the mass transport of species i

D	diffusion coefficient
M_{i}	molar mass of species i
v_{i}	diffusion volume of species i
$D_{\mathrm{m}}^{\mathrm{eff}}$	effective molecular diffusion coefficient
$D_{\mathrm{k}}^{\mathrm{eff}}$	Knudsen diffusion coefficient
d_{pore}	diameter of pore of electrodes
C_{p}	specific heat
S_{T}	heat source
κ_{g}	thermal conductivity of gas mixture
Q	generated heat source
MSR	methane steam reforming
WGSR	water gas shift reaction
H-SOFC	SOFC with proton ion conducting electrolyte
O-SOFC	SOFC with oxygen ion conducting electrolyte
ΔH^0	formation enthalpy of CH_4 at standard condition
q	electrical charge generated from SOFC

Greek symbols:

η_{act}	activation overpotential
η_{con}	concentration overpotential
η_{ohm}	ohmic overpotential
ϕ	electric potential
α	charge transfer coefficient
θ	contact angle between the electronic and ionic conducting particles
σ	electronic conductivity
μ	gas viscosity
ε	porosity of electrodes
τ	tortuosity of the porous electrodes
η	maximum efficiency of CH_4 fed SOFC

Subscripts:

rib	interconnect rib
a	anode
c	cathode
ch	channel
ASL	anode support layer

AAL	anode active layer
EL	electrolyte thickness
CCCL	cathode current collect layer
CAL	cathode active layer
υ	stoichiometric number
T	temperature
s	electron
l	ion
act	activation
con	concentration
ohm	ohmic
TPB	triple phase boundary
0	standard condition
Int	interconnect

Superscripts:

OCV	open circuit voltage
eff	effective
T	temperature

Chemical symbols:

YSZ	yttria-stabilized zirconia
LSM	lanthanum strontium manganite
Ni	nickel
H_2	hydrogen
H_2O	water
CO	carbon monoxide
CO_2	carbon dioxide
CH_4	methane
O_2	oxygen
N_2	nitrogen
e^-	electron
O^{2-}	oxygen ion
H^+	proton ion

CHAPTER 1 INTRODUCTION AND LITERATURE REVIEW

1.1 Fuel Cell introduction

1.1.1 Brief history of fuel cell

Fuel cell is energy conversion which can convert the chemical energy of fuel into electricity through electrochemical reactions. The first origin on fuel cell was reported that the German-Swiss chemist Christian Schönbein(1838)[1] discovered the electricity as two platinum wires surrounded with the atmosphere of hydrogen and oxygen respectively was put in an electrolyte solution. While, British chemist William Robert Grove[2] in 1839 demonstrated the first fuel cell which he called gas voltaic battery. This cell was operated with hydrogen and oxygen and used sulfuric acid solution as electrolyte solution. The solid oxide electrolytes discovered by Nernst in 1899[3] accelerated the arising of solid oxide fuel cells. The first SOFC operating at 1000℃ came up almost 100 years later than fuel cell, which was developed by Baur and Preis(1937)[4].

1.1.2 Fuel Cell Classification

Fuel cell can be classified by different electrolytes into five types: Alkaline Fuel Cell (AFC), Phosphoric Acid Fuel Cell (PAFC), Polymer Electrolyte

Membrane Fuel Cell (PEMFC), Solid Oxide Fuel Cell (SOFC), and Molten Carbonate Fuel Cell (MCFC). The characteristics of those five types of fuel cell are illustrated in Table 1.1.

Table 1.1 Characteristics of different types of fuel cells [5]

	AFC	PAFC	PEMFC	SOFC	MCFC
Electrolyte	Alkaline - potassium hydroxide	Phosphoric acid	Polymer acid	Ceramic membrane	Molten carbonate
Conducting ion	OH^-	H^+	H^+	O^{2-}	CO_3^{2-}
Operating temperature	50-200℃	∽220℃	70-100℃	500-1000℃	∽650℃
Current densities [A/cm^2]	0.1-0.4	0.15-0.4	0.4-0.9	0.3-1.0	0.1-0.2
Voltage [V]	0.85-0.6	0.8-0.6	0.75-0.95	0.95-0.6	0.95-0.75
Fuel	H_2	H_2	H_2	CH_4, H_2	CH_4, H_2
H_2	Fuel	Fuel	Fuel	Fuel	Fuel
CO	Poison	Poison	Poison	Fuel	Fuel
CH_4	Poison	Diluent	Diluent	Fuel	Diluent
CO_2&H_2O	Poison	Diluent	Diluent	Diluent	Diluent
S (H_2S & COS)	Poison	Poison	—	Poison	Poison

1.1.3 Fuel cell advantages and applications

Fuel cells have a lot of advantages compared to traditional power generators: higher power conversion efficiency, lower air pollutants, none movable components, less noise pollution, flexible power capacity and great potential for combined heat and power cogeneration. Fuel cells have a much higher efficiency than traditional power generators as the absence of the limitation by Carnot cycle

which presents in heat engines. In addition, fuel cells emit much lower air pollutants (NO_x, SO_x, CO_x etc.). The absence of movable components in fuel cells offers the potential of high stability and longevity. The flexible power capacity can meet various practical applications. The cogeneration systems of fuel cells and other energy devices (turbine, heat pumps, chillers etc.) can improve energy utilization and accordingly achieve energy saving.

With the aforementioned advantages and different types of fuel cells, the unceasing improvement and commercialization make the applications of full cells spread to a wide range of fields. Fuel cells can not only developed for stationary power generation, but also used in automotive and even portable devices. In stationary applications, fuel cells can be used not only in stationary combined heat and power (CHP) units, but also in the uninterruptible power supplies (UPS). Typically, fuel cell stationary power generator systems can offer electricity for off-grid remote regions with high economic efficiency. In portable applications, fuel cells can be adopted in laptop computers, mobile phones and other personal electronics. In transport applications, the world's major automotive manufacturers (Toyota, Mercedes-Benz, Honda, etc.) have already been on the way to the commercialization of fuel cell electric vehicles.

Fuel cells, as mentioned above, are widely used in terms of stationary

applications, and the fuel cell applications are to date dominated by over 50% stationary fuel cell systems in terms of megawatts, among which SOFC takes the largest proportion [6]. The wide and numerous usage of SOFC can be ascribed to the great advantages over other types of fuel cells: use of cheap metallic catalyst, high-grade exhaust heat for CHP, solid electrolyte and relatively high power density. Compared to fuel cells with the liquid electrolyte, the solid electrolyte fabricated SOFC can avoid suffering from material corrosion. SOFC commonly operates at high temperatures (500~1000℃) [5]. The high temperature brings SOFC with high theoretical efficiency, easy incorporation with CHP system, high fuel flexibility (hydrogen, hydrocarbons, ammonia, etc.), and efficient electrochemical reaction kinetics even with cheap catalyst such as Ni. Therefore, SOFC is the focus in this thesis work and will be discussed in following sections in detail.

1.2 Solid Oxide Fuel Cell Mechanism

Fuel cell is sandwich-like structure, assembled with anode and cathode which are separated by electrolyte. Fuel and oxidant take electrochemical reactions in anode and cathode electrodes respectively, and ions are conducted by electrolyte to connect the internal circuit. External circuit conducting electrons from anode to cathode can produce electricity. As demonstrated in Fig.1.1, Solid

Oxide Fuel Cells (SOFCs) consist of porous anode, porous cathode and dense ceramic electrolyte. In traditional SOFCs, yttrium stabilized zirconia (YSZ) with high oxygen ion conductivity is usually used as electrolyte material. Nickel mixed with YSZ (Ni/YSZ) as anode material has good electron and ion conductivity and high catalytic activity. In cathode, the typical material is lanthanum strontium manganite (LSM) also with good electron and ion conductivity and high catalytic activity. Fuel (i.e. H_2) is supplied into anode and reacts with oxygen ions to produce water and electrons. Electrons travel through the external circuit to arrive at cathode where oxygen reacts with electrons to produce oxygen ion. Produced oxygen ions can be transported to anode by oxygen ion-conducting electrolyte to complete the circuit.

Up to now, SOFCs normally operate at high temperatures (500~1000℃). The operation condition of high temperatures can achieve better electrochemical kinetics and high Nernst potential, therefore have high power density. In addition, SOFCs are flexible in fuel choice. The high temperature operation can also make it more efficient that the exhaust heat is applied in the system of combined heat and power generation.

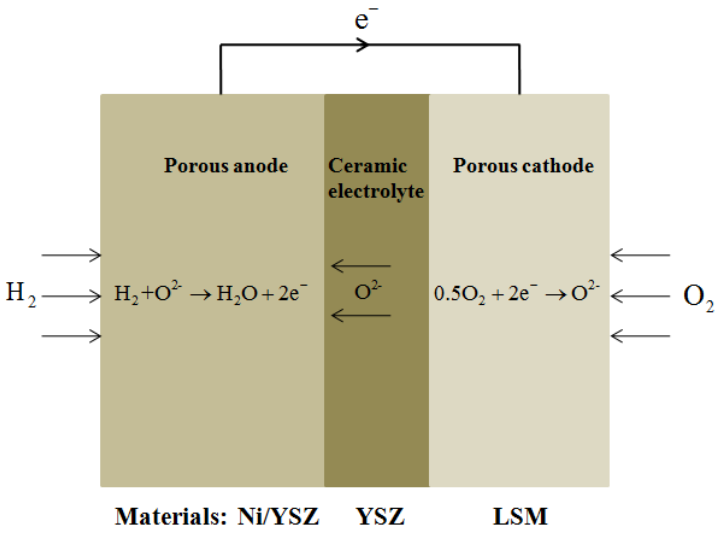

Figure 1.1 Diagram of the working mechanism of a typical hydrogen fed SOFC

1.3 Review of SOFC stacks

SOFC stack is an important component in practical applications. The open circuit voltage (OCV) of a single fuel cell at the value of around 1.0 V is limited. Single fuel cells are usually connected in series to produce stacks. Stacks can provide various voltages and power capacity to meet practical applications.

1.3.1 Modeling of SOFC stacks

In the study of fuel cells, modeling is normally adopted ascribed to the following main advantages over experimental methods: (1) cost saving and less time consuming; (2) detailed results of the parameters distribution inside cells; (3) effective parametric studies; (4) prediction and assistance for experiments.

There has been a great quantity of work on the modeling of SOFC stacks. The modeling studies on SOFC stacks can be summarized into three aspects: (1)

flow uniformity; (2) temperature distribution; (3) geometric design.

1.3.1.1 Flow uniformity

In planer SOFC stacks, a uniform flow distribution is desired to produce high performance of stacks. Kee et al. [7] developed a numerical model to predict the gas flow distribution in the channels network of planar SOFC stacks. In order to generalize the results, the governing equations are transformed by dimensionless variables and the solutions are summarized in two non-dimensional groups. A numerical code, written by Recknagle et al.[8] using STAR-CD, is a three-dimensional model of planar SOFC stacks. The modeling was conducted on co- counter- and cross- flow patterns. It was concluded that for similar geometries and operating temperature, the fuel utilization is similar no matter what type of flow pattern is used. Huang et al.[9] investigated the flow uniformity for stacks with different interconnect designs. A new design was proposed with guide vanes laying in the feed header in the module with double-inlet/single-outlet manifold and has good effect on the improvement of the flow uniformity. Moreover, a proper range between 20 and 50 for Reynolds number Re_{fuel} and a range between 200 and 300 for Re_{air} were identified in terms of smaller temperature gradient, reasonable fuel utilization and high power density. In design improvement of manifold configuration, Chen et al[10]

conducted modeling of a planar SOFC stack with 10 cells. The stack with a double-inlet/triple-outlet manifold design and counter-flow pattern has good flow uniformity and shows best performance. The influence of flow nonuniformity of planar SOFC stacks for different working conditions was investigated by Lin et al.[11] using a three-dimensional model, and the results show that the stack working under lower gas flow rate, lower voltage, using co-flow pattern or syngas has worse non uniform flow distribution.

1.3.1.2 Temperature distribution

In SOFC stacks, non uniform temperature distribution may bring severe local thermal stress so that it will break the stack. Thus, many researchers have done modeling to investigate the temperature distribution in stacks. In Recknagle's study[8], the temperature distribution in the stack is also investigated, and the result indicates that the temperature distribution of co-flow pattern is most uniform among co- counter- and cross- flow patterns. This result is also obtained by Wang et al.[12]. However, a numerical modeling of one cell in a planar SOFC stack was conducted by Xia et al.[13] and the results show that the temperature distribution of counter-flow stack is better than that of co-flow stack. To easily estimate the temperature gradient in the planar SOFC stacks, a simple equation was derived by Kulikovsky[14] and it has good

agreement with the result from other numerical modeling. A simulation study of a 3-cell planar SOFC stack configured with external manifolds was conducted by Yan et al.[15], and the results indicate that the performance variation between different cells in the stack is caused by the non uniform temperature distribution. Overall, the models mentioned above neglected the radiative heat transfer and only considered conductive and convective heat transfer. Seldom modeling included the radiative heat transfer. In the numerical study on the variations between cells in a planar SOFC stack by Burt et al.[16], the radiative heat transfer was also involved in model, and this model with the radiative heat transfer obtained more uniform temperature distribution than that only considering conductive/convective heat transfer. Above all, the temperature gradient is severe in planar SOFC stacks, and therefore heat transfer in the modeling of stack level must be considered. In this thesis, the heat transfer is included in all the models except for the model in Section 4.1(comparison between the model with heat transfer and the model without heat transfer).

1.3.1.3 Geometric design

Proper geometric deign can improve the performance the SOFC stacks, and therefore it is meaningful to conduct optimization studies on geometric deign of SOFC stacks. Wu et al.[17] used a three-dimensional model by ANSYS® CFX to

investigate the influence of geometries on gas flow uniformity in planar SOFC stacks. The results indicate that the ratio of the gas outlet manifold width to the gas inlet manifold width, α is the most key geometric parameter to flow uniformity and correspondingly to the stack performance. Furthermore, an analytical model was proposed to determine the optimum α and can be easily used for practical stack geometric design to improve the flow distribution and thus further increase the performance of planar stacks. In optimization of gas manifolds, it was pointed out by Chen et al.[10] that it is better to keep both inlet and outlet manifolds radius more than 5 mm for better flow uniformity.

Moreover, in the studies of planar SOFC stack geometric optimization, researchers also concentrated on the interconnect geometric size, and the performance of stacks can greatly benefit from this optimization. This is also the research focus in this thesis, and the details are discussed in the following section.

1.3.2 Optimization on geometric design of interconnect of SOFC stacks

In stacks, the component which is used to assemble the single cells to a stack is interconnect. According to the structure properties, stacks can be divided into tubular and planar stacks with various geometries ascribed to the fully solid structure as shown in Fig.1.2(a) and (b) respectively. Metal materials with high

electron conductivity (for example stainless steel) are normally used for interconnects [18-23]. Interconnects are the key components in both planar and tubular SOFC stacks regarding to their functions: high electric conductivity and good stability under the condition of reduction and oxidation reactions at high temperatures, as well as good compatibility of thermal expansion coefficient with other SOFC components (electrodes, electrolyte, etc.). Particularly in planar SOFC stacks, on one hand, interconnects are the key component of electron conducting; on the other hand, the gas flow channels are formed by interconnects together with electrodes as shown in Fig.1.2(b). Therefore, the interconnect geometries can not only influence the electron collecting but also the gas diffusion in electrodes. Because the electron conducting and gas distribution have significant impact on the performance of planar SOFC stacks, it is assured that the interconnect geometries have great effect on the performance of planar SOFC stacks. Also, it can be foreseen that there should be optimum interconnect geometry for best stack performance under the condition of determined stack shape sizes. Thus, the study on the optimization of interconnects geometries of planar SOFC stack is of great significance.

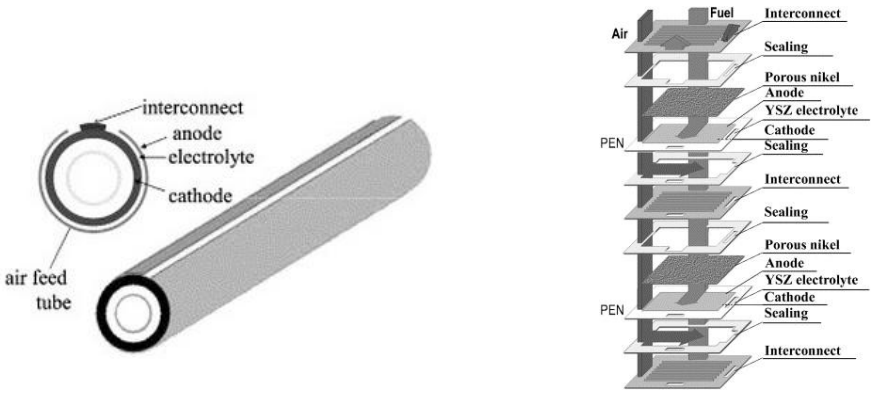

(a) (b)

Figure 1.2(a) Schematic diagram of a tubular SOFC stack[24]; (b) Schematic of a planar SOFC stack [25]

As mentioned above, the gas channels are formed by interconnects together with electrodes, namely, the geometric sizes of interconnects determine the gas channels. When the other geometric parameters of a SOFC stack maintain constant, the change of interconnect rib size will influence the electrons collecting path and gas diffusion path in electrodes, thereby influence the ohmic loss and gas uniformity respectively. Furthermore, when the interconnect rib size is bigger, the SOFC stack can obtain less ohmic loss ascribed to shorter electron conducting path, on the contrary, suffer from more concentration loss attributed by the higher gas diffusion resistance. However, when the interconnect rib size is smaller, the consequence turns out to just the opposite. Thus, the contradictory relationship remains between the ohmic loss by electron conducting and the concentration loss by the gas nonuniformity with the consideration of the change of the interconnect rib size. The investigations on the SOFC interconnect size are

normally conducted with the consideration of two factors: (1) electronic resistance; (2) gas diffusion resistance.

In the investigation of the optimization of SOFC interconnect geometric size, there were limited studies. In 2003, Lin et al. [26] built a concentration polarization model to investigate the influence of interconnect rib size on the concentration polarization in planar SOFCs. It is concluded that the uniformity of the gas concentration is good when the rib width is smaller than the characteristic penetration distance. Furthermore, with the consideration of both of the electrical resistance and concentration polarization, the optimal rib width was obtained, the ratio of which to the channel width should be from 1/3 to 2/3.

In order to study the prominent geometric parameter for the flow uniformity in planar SOFC stacks, 3D models were built and calculated by CFD method by Bi et al. [17] in 2009. It is discovered that the ratio of the outlet manifold width to that of inlet (α) is the key factor of the flow distribution uniformity. The stack flow with α larger than 1 is more uniform than that with α=1. Based the previous 2D models, a three-dimensional multi-physics numerical models were first developed by Liu et al. [27] in 2009 and used to optimize the rib widths in SOFC stacks with co-, counter-, and cross-flow designs. The optimal rib widths are very similar for the above three designs. In addition, the results of the optimal rib

widths by 3D models are quite similar to that by 2D models that can be adopted to simplify the further modeling work. Bi et al. [28] in 2010 researched on large size planar SOFCs with U-type flow field by realistic 3D models. The results show that the interconnect width ratio is the significant factor in determining the air flow uniformity. To examine the interconnect rib size effect on cathode supported SOFC stacks, a three-dimensional modeling of syngas supplied planar SOFC stack was conducted by Kong et al. [29]. The optimum interconnect rib size is sensitive to the structure of stacks. The optimum anode rib width of anode- or cathode supported SOFC stacks is different, and the optimum anode rib width of anode-supported SOFC stacks is much bigger than that of cathode-supported SOFC stacks. It is revealed that the optimum rib width for anode side and cathode side could be different and is dependent on the thickness of electrode thickness.

To conclude, it is sufficiently proved that the interconnect width size has great impact on planar SOFC stacks and there is optimum interconnect width size to achieve best stack performance under the condition of certain shape sizes of stacks. However, the proposed models still have many drawbacks that should be improved. Firstly, most of the models only consider the hydrogen as fuel. In fact, one of the most crucial advantages of SOFCs is fuel flexibility (hydrogen,

hydrocarbons, ammonia…) which makes SOFC remarkable in all types of fuel cells. Obviously, only consideration with hydrogen fed SOFC stacks limit the application of the results. Secondly, almost all the previous models except for Kong's model [29] only supposed that the temperature is uniform in the whole computing domains, namely, the temperature influence is neglected. Even though Kong et al [29] considered heat transfer in the model, the temperature influence was not stated. However, temperature as one of the important operating conditions has vital effect on the performance of SOFC stacks from different aspects: gas diffusion, electron and ion conducting, electrochemical kinetics, etc. As reported by Andersson [30], the maximum temperature difference in a hydrogen fed SOFC stack can reach as high as 136K. Furthermore, the temperature distribution in hydrocarbons or syngas supplied SOFC stacks is more complicated due to the potential endothermic reforming reactions and exothermic gas shift reactions. Therefore, thermal transfer resulting in the temperature distribution should be involved in modeling for more convincing results. Thirdly, carbon monoxide (CO) electrochemical reaction normally was neglected in previous models. In hydrocarbons fed SOFCs, hydrocarbons are usually first diverted to H_2 and CO to anticipate the electrochemical reactions. It was reported from Matsuzaki's experiments, when hydrogen and CO are

synchronously present in anode electrode, that CO electrochemical reaction rate at the interface of YSZ electrolyte and Ni/YSZ electrode can be around 1/2 to 1/3 of that of H_2 when the temperatures shift from 1023K and 1273K[31]. Although the CO reaction rate is much smaller than that of H_2, it should not be neglected in modeling. Fourthly, the present models, no matter 2D or 3D, only adopt plug flow, that is the gases inlet is at the interface channels and electrodes and the inlet flow direction is vertical to the interface of channels and electrodes. The plug flow assumption neglects the gases flow in the channels which is much disparate from the factual gas flow in a SOFC stack. In fact, the gases first flow into the channels from inlets and then diffuse into the porous electrodes; also the exhaust gases are removed from the outlets. Therefore, the continuity and momentum equations must be employed in simulating the gases flowing in channels.

1.4 Review of SOFC fed by different fuels

SOFC has great advantage of fuel flexibility attributed to high operating temperatures (500-1000℃). Not only hydrogen but also hydrocarbons (i.e. syngas, methane and ethanol) can be used in SOFC to generate electricity power. To generalize the optimization results on interconnect for SOFC stacks fed by different fuels, models in this thesis considered three widely used fuels: hydrogen (**Chapter 3**), syngas(**Chapter 4**) and methane(**Chapter 5**).

1.4.1 SOFC fed by Hydrogen

Hydrogen is an attractive fuel to SOFC because of high energy density and no emission. Thus, hydrogen is mostly widely used nowadays. The methods of hydrogen production are electrolysis of water/steam, thermochemical decomposition of water, conversion of hydrocarbons, biogas method and radiolysis of water[32, 33].

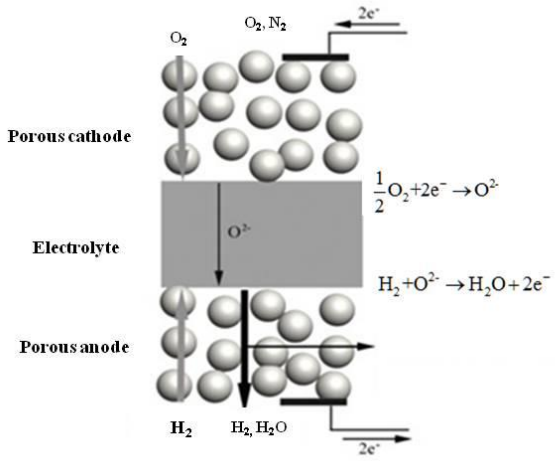

Figure 1.3 Schematic diagram of H_2 fed SOFC

In hydrogen fed SOFCs, the schematic diagram is shown in Fig.1.3[34]. The hydrogen is delivered to anode, and then transported through the porous electrode to the zone nearby the interface of anode and electrolyte, where hydrogen reacts with oxygen ions and produces electrons and water. Electrons go through the external circuit and arrive at interface of cathode and electrolyte, where electrons react with oxygen to produce oxygen ions. Then the produced

oxygen ions are transported to anode through electrolyte. The electrochemical reactions occur at anode and cathode TPB are expressed as Eq.(1-1) and (1-2), respectively.

$$H_2 + O^{2-} \leftrightarrow H_2O + 2e^- \quad (1\text{-}1)$$

$$\frac{1}{2}O_2 + 2e^- \leftrightarrow O^{2-} \quad (1\text{-}2)$$

1.4.2 SOFC fed by syngas

Syngas is a mixture gas mainly consisting of H_2, CO and sometimes H_2O/CO_2. Syngas production is normally by the technologies of reforming of hydrocarbons, partial oxidation of hydrocarbons, electrolysis, and biomass gasification (coal, coke)[35-40].

The schematic diagram of syngas fed SOFC is shown in Fig.1.4[40]. In syngas fed SOFCs, water gas shift reaction (WGSR) is considered occurring in anode, and the expression is as follows.

$$CO + H_2O \leftrightarrow H_2 + CO_2 \quad (1\text{-}3)$$

The electrochemical reactions, summarized as Eqs.(1-4a) and (1-5b) for anode and Eq.(1-5) for cathode, are similar to H_2 fed SOFC except for the consideration of CO electrochemical reaction in anode. It was reported by Matsuzaki et al. [31]in 2000 that the electrochemical rate of CO is about 1/3 to 1/2 of that of H_2 in the electrochemical oxidation reactions of a H_2-H_2O-CO-CO_2

system. Therefore, although the reaction rate of CO is much smaller than that of H_2, the electrochemical oxidation of CO is obvious and should be involved. This consideration can also be found in models from literatures[41] [30, 42, 43].

$$H_2 + O^{2-} \leftrightarrow H_2O + 2e^- \quad (1\text{-}4a)$$

$$CO + O^{2-} \leftrightarrow CO_2 + 2e^- \quad (1\text{-}4b)$$

$$\frac{1}{2}O_2 + 2e^- \leftrightarrow O^{2-} \quad (1\text{-}5)$$

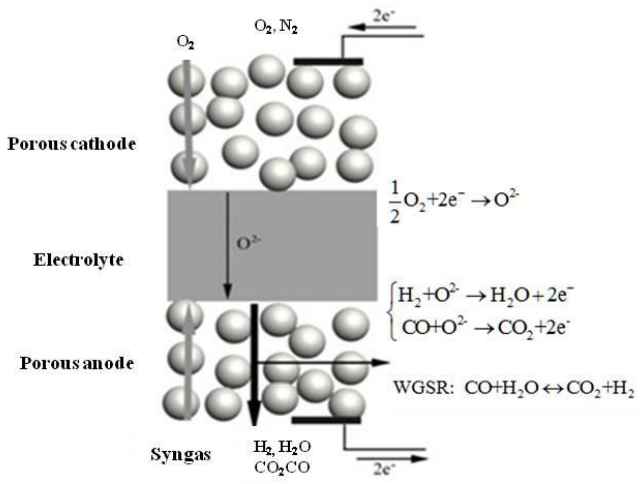

Figure 1.4 Schematic diagram of syngas fed SOFC

1.4.3 SOFC fed by Methane with internal reforming

Methane is a promising alternative fuel for SOFC with advantages of accessibility, easy storage and relatively high energy density among hydrocarbons. Methane is normally reformed when used in SOFC. The SOFC with internal reforming has the merits of simple fuel cell system compared to

external internal reforming (without auxiliary reforming device) and cooling effect due to the endothermic reaction of methane reforming, which is friendly to temperature uniformity in the whole cell stack, and thus this utilization attracted a lot of attention[42, 44-55]. Note that the SOFC fed by Methane with internal reforming is investigated as well in this thesis (**Chapter 5**).

In methane fed SOFCs, internal reforming reaction consists of direct informing reaction (DIR) and water gas shift reaction (WGSR) which occurs with the catalysis of nickel (Ni) in anode, as expressed in Equation (1-6), (1-7) respectively.

$$CH_4 + H_2O \leftrightarrow 3H_2 + CO \quad (1\text{-}6)$$

$$CO + H_2O \leftrightarrow H_2 + CO_2 \quad (1\text{-}7)$$

The electrochemical reactions, similar to syngas fed SOFC mentioned above, occur at the TPB of anode and cathode can be expressed as Equation (1-8), (1-9), respectively.

$$H_2 + O^{2-} \leftrightarrow H_2O + 2e^- \quad (1\text{-}8a)$$

$$CO + O^{2-} \leftrightarrow CO_2 + 2e^- \quad (1\text{-}8b)$$

$$\frac{1}{2}O_2 + 2e^- \leftrightarrow O^{2-} \quad (1\text{-}9)$$

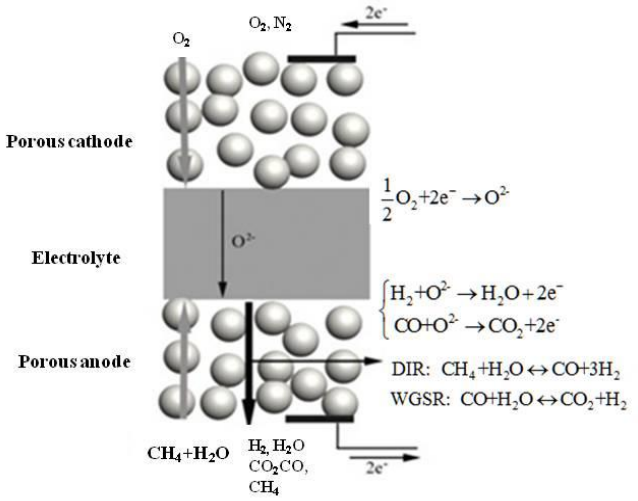

Figure 1.5 Schematic of methane fed SOFC with DIR and WGSR

The performance of methane fed SOFC is influenced by the inlet fuel composition (steam-to-carbon ratio). Joonguen Park et al. [54] developed a 3D model of methane fed internal reforming SOFCs to predict the cell performance. It was found that a low steam-to-carbon ratio increased current density. However, too low steam- to-carbon ratio may result in carbon deposition in anode which will block gas diffusion and deteriorate electrochemical activity. Therefore, the inlet steam fraction should be increased from the viewpoint of elimination of the carbon deposition [56]. This was also suggested by the analysis of Yang et al.[57] that it is important to select proper inlet H_2O/CH_4 ratio considering both of H_2 yield and carbon deposition. Basing on the above analysis, in this thesis (**Chapter 5**) the inlet steam-to-carbon ratio ranges from 1:1 to 3:1.

1.5 Research method of SOFC stack modeling

Through reviewing literatures mentioned above, numerical modeling is determined to solve the fully coupled problems of SOFC stack. A comprehensive three-dimensional (3D) model of anode supported SOFC stack with co-flow pattern is developed including sub-models of electrons and ions transport, electrochemical reactions, chemical reactions if needed, momentum transport, mass transport and heat transfer (described in **Chapter 2** in detail). The fuels fed to SOFC are H_2, syngas and CH_4, respectively. This 3D model is built on and solved by COMSOL Multiphysics®.

1.6 Review of thermodynamic analysis of CH_4 fed SOFC with internal reforming

As mentioned above, hydrocarbon fuels, such as methane and methanol, can be used in SOFC with internal reforming reaction in SOFC porous anode electrode. In SOFC, electrolyte is an important component. There are two types of electrolyte usually used in SOFC. One is oxygen ion conducting electrolyte such as yttria-stabilized zirconia (YSZ) which is also used as the electrolyte for 3D SOFC stack modeling in this thesis. The other is proton conducting electrolyte (i.e. $BaCeO_3$ doped with Gd or Nd). SOFC with different electrolytes has not only different ohmic losses, but has different electrochemical reactions in

two sides of electrodes which influences gas diffusion in porous electrodes. In H-SOFC, steam is produced in cathode which blocks the oxygen diffusion to the interface of electrolyte and cathode[42, 58].

Thermodynamic analyses of both H_2 and hydrocarbon fed SOFCs have been conducted to distinguish the performance of H-SOFC and O-SOFC and to find out the influence on the performance of SOFCs caused by using different types of electrolyte. The first thermodynamic study on the maximum efficiencies of H-SOF and O-SOFC with hydrogen as fuel was conducted by Demin et al. in 2001[59]. It was uncovered that compared with O-SOFC, hydrogen fueled H-SOFC shows better performance because H-SOFC has higher fuel concentration in the porous anode. Based on this study, a model of methane fueled H-SOFC and O-SOFC was developed[60]. It was revealed that methane fed H-SOFC showed higher maximum efficiency than methane fed O-SOFC. Similar results were also concluded through thermodynamic studies of SOFCs fueled by ammonia or ethanol [61-63].

However, in previous thermodynamic analyses on SOFCs fueled by methane or ethanol, CO electrochemical reaction was neglected in O-SOFC and only H_2 electrochemical reaction was involved. As mentioned above (Section 2.6), it has been proved by experiments that CO electrochemical reaction also

occurs in O-SOFC and the electrochemical rate of CO is about 1/3 to 1/2 of that of H_2 in the electrochemical oxidation reactions of a H_2-H_2O-CO-CO_2 system[31]. It is still not confirmed that the H-SOFC fueled by methane has larger maximum efficiency than O-SOFC since CO electrochemical oxidation could occur in O-SOFC while not in H-SOFC. Therefore, the comparison between methane fed H-SOFC and O-SOFC needs further analyses when CO electrochemical reaction is also considered in O-SOFC. Based on the previous models, a thermodynamic model considering CO electrochemical oxidation is developed and used to analyze the maximum efficiency difference between methane fed H-SOFC and O-SOFC (**Chapter 6**).

1.7 Study objectives

This research work consists of 2 parts. In part one, the study objective is to investigate the effect of interconnect geometry on SOFC stack performance. SOFC can run on varieties of fuels (i.e. hydrogen, hydrocarbons…) due to the high operating temperature. The mechanism of electrochemical reactions and chemical reactions (if occur) in porous anode depends on fuels. Therefore, part one can further be divided into 3 parts concerning different fuels utilized in SOFC. In part two, the work is to conduct a primary thermodynamic study on methane fed SOFC with different electrolytes considering different mechanism

of electrochemical reactions.

Part 1: A comprehensive three-dimensional (3D) model of planar SOFC is developed in **Chapter 2**. This 3D model involves electrochemical reactions, electrons and ions transport, mass transport, gas diffusion, chemical reactions (if any) and heat transfer. In **Chapter 3**, this 3D model is used to investigate the effect of interconnect geometry on hydrogen fed SOFC stack performance. This study is used to compare with the previous study on hydrogen fed SOFC stack reported in literature. In **Chapter 4**, the investigation is extended to syngas fed SOFC stack which involves CO electrochemical oxidation and water gas shift reaction in porous anode. In **Chapter 5**, the effect of interconnect geometry on methane fed SOFC stack with internal reforming is conducted.

Part 2: Basing on previous models, a simple thermodynamic model is developed to investigate the difference between methane fed H-SOFC and O-SOFC with internal reforming considering different mechanism of electrochemical reactions in porous anode. This is the main content in **Chapter 6**.

CHAPTER 2 MODEL DEVELOPMENT

2.1 Geometric model

A typical planar SOFC stack is shown in Fig.2.1[64]. It consists of a number of repeating sections which contains 4 functional layers. These functional layers include anode interconnect, porous anode, electrolyte, porous cathode, cathode interconnect and sealing. Interconnect is used to separate fuel and gas, form the gas channels and collect electrons. Note that interconnect is also the research focus in this thesis.

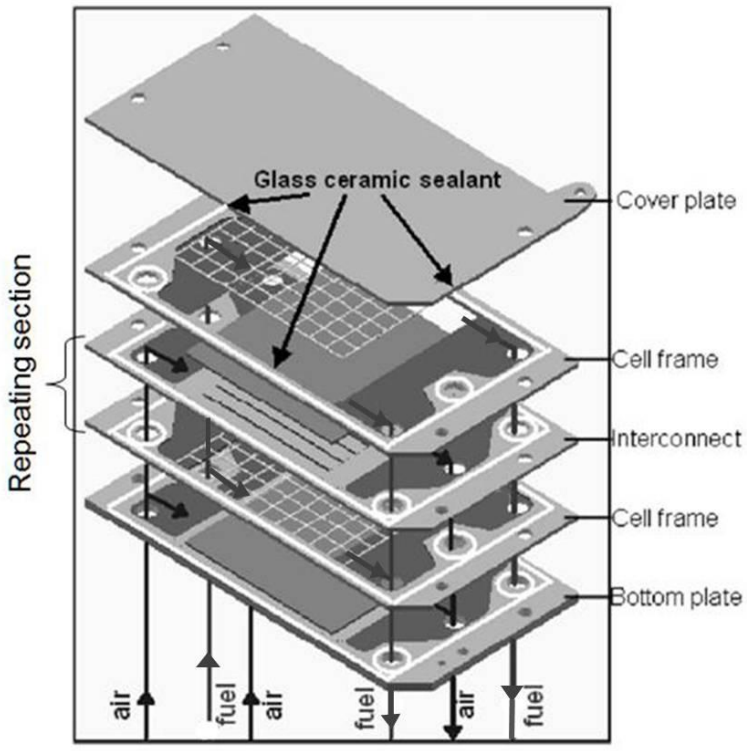

Figure 2.1 The schematic diagram of a typical planar SOFC stack

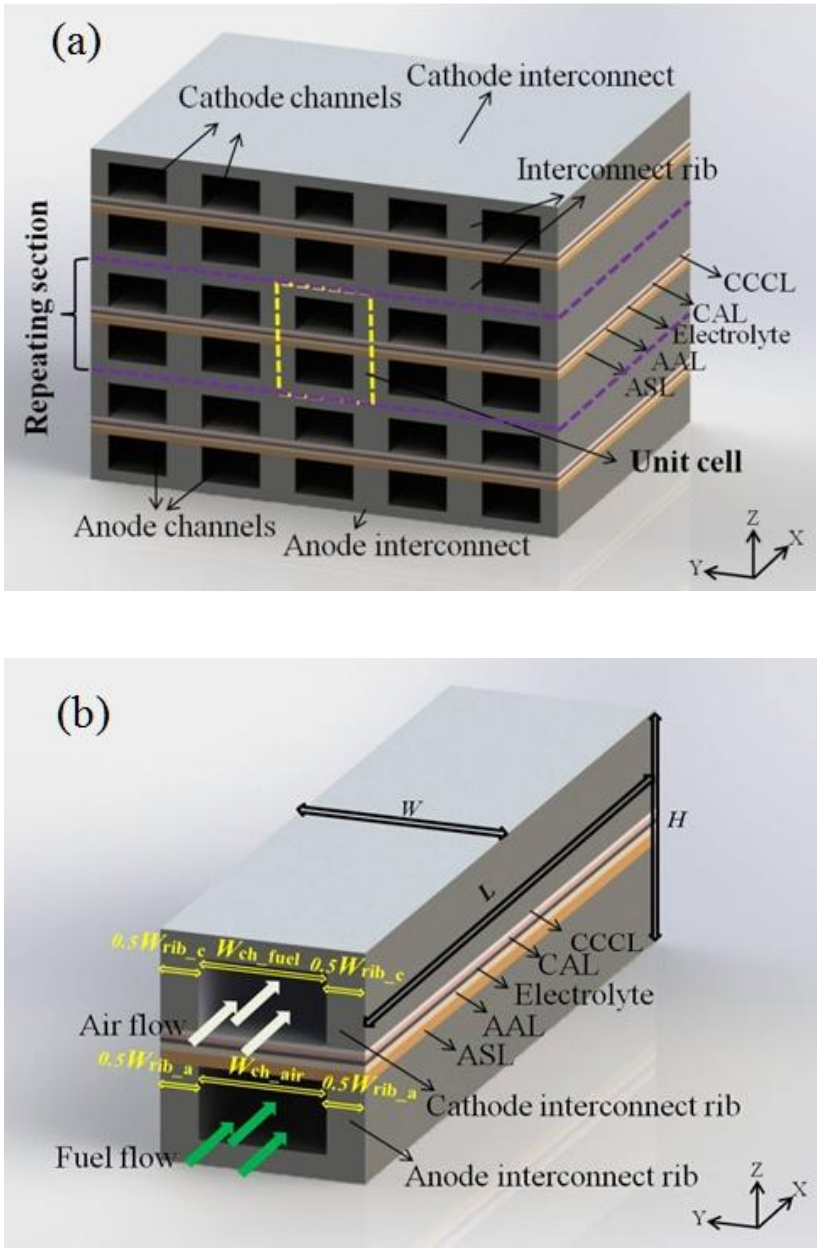

Figure 2.2 The geometric model of a planar SOFC stack: (a) a complete planer SOFC stack model; (b) a unit cell model

A cube with corresponding functional layers is developed to model the stack as shown in Fig.2.2. Fig.2.2(a) is the schematic diagram of a complete planar SOFC stack. It contains a number of repeating sections which are connected in parallel. Assuming that the stack is symmetric, the massive geometric model can

be simplified as a smallest repeating unit as Fig 2.2(b) shows. The complete geometric model not only takes a large amount of time, but needs excessive computer capacity to calculate. Therefore, the repeating unit cell is normally used to model the stack even though the complete geometric model is more accurate. The repeating unit cell, which consists of one air channel, one fuel channel, cathode, electrolyte, anode, anode interconnect, and cathode interconnect, is used as the calculation domain in this thesis's models. The unit cell geometry used in this thesis is listed in Table 2.1. Here, Ra_a and Ra_c, two dimensionless variables, are defined as the ratio of the anode interconnect rib width to the unit cell width and the ratio of cathode interconnect rib width to the unit cell width, respectively, and given by

$$Ra_a = \frac{W_{rib\_a}}{W} \tag{2-1a}$$

$$Ra_c = \frac{W_{rib\_c}}{W} \tag{2-1b}$$

These dimensionless variables are used in the following parametric studies on the interconnect rib size, and this dimensionless method can make the parametric studies more easier to conduct, make comparison between cells with different pitch width more effective, and provide a simple optimum parameter for practical stack designs.

Table 2.1 Unit Cell geometry

Component	Parameters
Length, L	10 cm
Width, W	1,2,3 mm
Fuel channel height, H_{ch_fuel}	0.5 mm
Air channel height, H_{ch_air}	0.5 mm
Anode support layer thickness, H_{ASL}	735 μm
Anode active layer thickness, H_{AAL}	15 μm
Electrolyte thickness, H_{EL}	50 μm
Cathode current collect layer thickness, H_{CCCL}	40 μm
Cathode active layer thickness, H_{CAL}	10 μm
Anode interconnect thickness, H_{Int_a}	150 μm
Cathode interconnect thickness, H_{Int_c}	150 μm
Fuel channel width, W_{ch_fuel}	$(1 - Ra) \times W$
Air channel width, W_{ch_air}	$(1 - Rc) \times W$
Anode interconnect rib width, W_{rib_a}	$Ra \times W$
Cathode interconnect rib width, W_{rib_c}	$Rc \times W$

2.2 Mathematical model

2.2.1 Electrochemical model

The open circuit voltage (OCV) is the equivalent equilibrium potential and can be expressed by Nernst equations[65],

$$E^{\mathrm{OCV}} = \frac{-\Delta G}{nF} = E_{\mathrm{T}} - \frac{RT}{nF} \ln \frac{\prod a_{\mathrm{products}}^{\nu_i}}{\prod a_{\mathrm{reactants}}^{\nu_i}} \tag{2-2}$$

$$E_{\mathrm{T}} = E_0 + \frac{\Delta s}{nF}(T - T_0) \tag{2-3}$$

where E^{OCV} represents the open circuit voltage under working conditions, ΔG is the change of Gibbs free energy of electrochemical reactions, R is the ideal gas constant (8.3145J mol^{-1} K^{-1}), T is temperature (K), F is the Faraday constant (96485 C mol^{-1}), n is the number of electrons involved per

electrochemical reaction. The symbol a is the activation of species and the activation of gas can be determined by $a = p/p_0$ where p is the gas partial pressure and p_0 is the standard pressure (1 atm). E_0 is the equilibrium potential at the standard conditions (T_0 =25℃, p_0 =1atm), and Δs is the entropy difference of electrochemical reactions.

(1) Hydrogen(H_2) electrochemical reaction

The H_2 electrochemical reaction can be expressed as

$$H_2 + \frac{1}{2}O_2 \leftrightarrow H_2O \quad (2\text{-}4a)$$

$$H_2 + O^{2-} \leftrightarrow H_2O + 2e^- \quad (2\text{-}4b)$$

$$\frac{1}{2}O_2 + 2e^- \leftrightarrow O^{2-} \quad (2\text{-}4c)$$

The total OCV of H_2 can be calculated by Nernst equation and be written as [66]

$$E_{H_2}^{OCV} = E_{T,H_2} - \frac{RT}{nF}\ln\frac{a_{H_2O}}{a_{H_2}a_{O_2}^{0.5}} \quad (2\text{-}5)$$

$$E_{T,H_2} = 1.253 - 2.4516 \times 10^{-4}T \quad (2\text{-}6)$$

(2) Carbon monoxide (CO) electrochemical reaction

The CO electrochemical reaction can be expressed as

$$CO + \frac{1}{2}O_2 \leftrightarrow CO_2 \quad (2\text{-}7a)$$

$$CO + O^{2-} \leftrightarrow CO_2 + 2e^- \quad (2\text{-}7b)$$

$$\frac{1}{2}O_2 + 2e^- \leftrightarrow O^{2-} \quad (2\text{-}7c)$$

The total OCV of CO can be calculated by Nernst equation and be written as[40]

$$E_{\mathrm{CO}}^{\mathrm{OCV}} = E_{\mathrm{T,CO}} - \frac{RT}{nF}\ln\frac{a_{\mathrm{CO}_2}}{a_{\mathrm{CO}}\, a_{\mathrm{O}_2}^{0.5}} \tag{2-8}$$

$$E_{\mathrm{T,CO}} = 1.46713 - 4.527\times10^{-4}T \tag{2-9}$$

(3) Overpotentials

The actual cell potential (V) is smaller than OCV because of the existence of resistance and overpotentials. The overpotentials consist of activation overpotential, concentration overpotential and ohmic overpotential. Therefore, the actual cell potential can be calculated as

$$V = E^{\mathrm{OCV}} - \eta_{\mathrm{act}} - \eta_{\mathrm{con}} - \eta_{\mathrm{ohm}} \tag{2-10}$$

where η represents the overpotentials. In models, the activation overpotentials in anode and cathode are defined by Eq.(2-11) and Eq.(2-12) respectively,

$$\eta_{\mathrm{act,a}} = \phi_{\mathrm{s}} - \phi_{\mathrm{l}} - E_{\mathrm{a}}^{\mathrm{OCV}} \tag{2-11}$$

$$\eta_{\mathrm{act,c}} = \phi_{\mathrm{s}} - \phi_{\mathrm{l}} - E_{\mathrm{c}}^{\mathrm{OCV}} \tag{2-12}$$

where ϕ is the electric potential, the subscripts s and l represent the electron and ion respectively and the E^{OCV} can be derived from Eq.(2-5) and (2-8) and can be written as following equations

$$E_{\mathrm{a,H_2}}^{\mathrm{OCV}} = -(1.253 - 2.4516\times10^{-4}T) + \frac{RT}{nF}\ln\frac{p_{\mathrm{H_2O}}}{p_{\mathrm{H_2}}} \tag{2-13}$$

$$E_{\mathrm{a,CO}}^{\mathrm{OCV}} = -(1.46713 - 4.527\times10^{-4}T) + \frac{RT}{nF}\ln\frac{p_{\mathrm{CO_2}}}{p_{\mathrm{CO}}} \tag{2-14}$$

$$E_{\mathrm{c,O_2}}^{\mathrm{OCV}} = -\frac{RT}{nF}\ln\left(\frac{p_{\mathrm{atm}}}{p_{\mathrm{O_2}}}\right)^{0.5} \quad (2\text{-}15)$$

a) Concentration overpotential

The concentration overpotentials can be expressed as [21-22]:

$$\eta_{\mathrm{con,a}}^{\mathrm{H_2}} = \frac{RT}{2F}\ln\left(\frac{p_{\mathrm{H_2}}}{p_{\mathrm{H_2,TPB}}}\frac{p_{\mathrm{H_2O,TPB}}}{p_{\mathrm{H_2O}}}\right)^{0.5} \quad (2\text{-}16a)$$

$$\eta_{\mathrm{con,a}}^{\mathrm{CO}} = \frac{RT}{2F}\ln\left(\frac{p_{\mathrm{CO}}}{p_{\mathrm{CO,TPB}}}\frac{p_{\mathrm{CO_2,TPB}}}{p_{\mathrm{CO_2}}}\right)^{0.5} \quad (2\text{-}16b)$$

$$\eta_{\mathrm{con,c}} = \frac{RT}{4F}\ln\frac{p_{\mathrm{O_2}}}{p_{\mathrm{O_2,TPB}}} \quad (2\text{-}17)$$

where $p_{\mathrm{H_2,TPB}}$, $p_{\mathrm{H_2O,TPB}}$, $p_{\mathrm{CO,TPB}}$, $p_{\mathrm{CO_2,TPB}}$, $p_{\mathrm{O_2,TPB}}$ represent the partial pressure of H_2, H_2O, CO and CO_2 at the anode TPB and the partial pressure of O_2 at cathode TPB, respectively.

Substituting Eqs.(2-16a), (2-16b) and (2-17) to Eqs.(2-13), (2-14) and (2-15) respectively, the local E^{OCV} at the active TPB locations can be rewritten to

$$E_{\mathrm{TPB,H_2}}^{\mathrm{OCV}} = -(1.253 - 2.4516\times10^{-4}T) + \frac{RT}{2F}\ln\frac{p_{\mathrm{H_2O,TPB}}}{p_{\mathrm{H_2,TPB}}} \quad (2\text{-}18)$$

$$E_{\mathrm{TPB,CO}}^{\mathrm{OCV}} = -(1.46713 - 4.527\times10^{-4}T) + \frac{RT}{2F}\ln\frac{p_{\mathrm{CO_2,TPB}}}{p_{\mathrm{CO,TPB}}} \quad (2\text{-}19)$$

$$E_{\mathrm{TPB,O_2}}^{\mathrm{OCV}} = -\frac{RT}{2F}\ln\left(\frac{p_{\mathrm{atm}}}{p_{\mathrm{O_2,TPB}}}\right)^{0.5} \quad (2\text{-}20)$$

b) Activation overpotential

The activation overpotentials can be calculated by the Butler-Volmer equations [41, 67] as

$$i_{\mathrm{a,H_2}} = S_{\mathrm{V}}\cdot i_{0,\mathrm{a}}\left[\frac{c_{\mathrm{H_2,TPB}}}{c_{\mathrm{H_2,bulk}}}\exp\left(\frac{\alpha nF\eta_{\mathrm{act,a}}}{RT}\right) - \frac{c_{\mathrm{H_2O,TPB}}}{c_{\mathrm{H_2O,bulk}}}\exp\left(\frac{(1-\alpha)nF\eta_{\mathrm{act,a}}}{RT}\right)\right] \quad (2\text{-}21a)$$

$$i_{\mathrm{a,CO}} = S_{\mathrm{V}}\cdot i_{0,\mathrm{a}}\left[\frac{c_{\mathrm{CO,TPB}}}{c_{\mathrm{CO,bulk}}}\exp\left(\frac{\alpha nF\eta_{\mathrm{act,a}}}{RT}\right) - \frac{c_{\mathrm{CO_2,TPB}}}{c_{\mathrm{CO_2,bulk}}}\exp\left(\frac{(1-\alpha)nF\eta_{\mathrm{act,a}}}{RT}\right)\right] \quad (2\text{-}21b)$$

$$i_{\mathrm{c}} = S_{\mathrm{V}}\cdot i_{0,\mathrm{c}}\left[\exp\left(\frac{\alpha nF\eta_{\mathrm{act,c}}}{RT}\right) - \frac{c_{\mathrm{O_2,TPB}}}{c_{\mathrm{O_2,bulk}}}\exp\left(\frac{(1-\alpha)nF\eta_{\mathrm{act,c}}}{RT}\right)\right] \quad (2\text{-}21c)$$

$$i_0 = \frac{RT}{nF} \cdot k_{\mathrm{e}} \cdot \exp\left(\frac{-E_{\mathrm{act}}}{RT}\right) \tag{2-21d}$$

where η_{act} is the activation overpotential, n is the electron number per reaction, α is recommended to 0.5 , and S_{V} is the active specific area per electrode volume and can be determined according to the binary random packing theories. i_0 is the exchange current density and can be predicted by Eq.(2-21d), where k_{e} is the pre-exponential factor ($6.54 \times 10^{11}\Omega^{-1}\mathrm{m}^{-2}$ for anode and $2.35 \times 10^{11}\Omega^{-1}\mathrm{m}^{-2}$ for cathode[68]), and E_{act} is the activation energy which is the property of electrodes. A proper range of E_{act} can be summarized from the previous studies [30, 69]. For anode, $E_{\mathrm{act,a}}$ is between 110 and 140 kJ mol^{-1}, and $E_{\mathrm{act,c}}$ for cathode changes from 130 to 190 kJ mol^{-1}.

The binary random packing theories [70-74] were used to model the composite porous electrodes, and S_{V} can be calculated as

$$S_{\mathrm{V}} = \pi \sin^2\theta\, r_{\mathrm{e}}^2 n_{\mathrm{t}} n_{\mathrm{e}} n_{\mathrm{i}} \frac{Z_{\mathrm{e}} Z_{\mathrm{i}}}{6} P_{\mathrm{e}} P_{\mathrm{i}} \tag{2-22a}$$

$$n_{\mathrm{t}} = \frac{1-\varepsilon}{(4/3)\pi r_{\mathrm{e}}^3 [n_{\mathrm{e}} + (1-n_{\mathrm{e}})(r_{\mathrm{i}}/r_{\mathrm{e}})^3]} \tag{2-22b}$$

$$P_{\mathrm{e}} = \left[1 - \left(\frac{3.764 - Z_{\mathrm{e,e}}}{2}\right)^{2.5}\right]^{0.4} \tag{2-22c}$$

$$P_{\mathrm{i}} = \left[1 - \left(\frac{3.764 - Z_{\mathrm{i,i}}}{2}\right)^{2.5}\right]^{0.4} \tag{2-22d}$$

where θ is the contact angle between the electronic and ionic conducting particles; r_{e} the radius of the electronic conductors; n_{t} the total number of particles per unit volume; n_{e} and n_{i} the number fractions of electronic and

ionic conductor, respectively; Z_e and Z_i the coordination numbers of electronic and ionic conductors, respectively; P_e is the probability of electronic conductors connected with the porous media; and P_i is the probability of ionic conductors connected with the porous media.

c) Ohmic overpotential

The governing equations of electron and ion conducting can be written as follows

$$\nabla \cdot \vec{i_s} = -i,\ \vec{i_s} = -\sigma_s \nabla \phi_s \tag{2-23a}$$

$$\nabla \cdot \vec{i_l} = i,\ \vec{i_l} = -\sigma_s \nabla \phi_l \tag{2-23b}$$

where ϕ is the electric potential, σ is the electronic conductivity, i is the current density and the subscripts s and l represent the electron and ion respectively. The electronic conductivity is the intrinsic physical property of material. In this study, yttria stabilized zirconia (YSZ) is used for electrolyte, the compound of Sr-doped lanthanum manganite (LSM) and YSZ is adopted in cathode and Ni-YSZ is utilized in anode. The electronic conductivities of the above electronic conducting materials can be calculated by [30, 75]

$$\sigma_{s,Ni} = \frac{9.5\times10^7}{T}\exp\left(\frac{-1150}{T}\right) \tag{2-24a}$$

$$\sigma_{s,LSM} = \frac{4.2\times10^7}{T}\exp\left(\frac{-1200}{T}\right) \tag{2-24b}$$

$$\sigma_{l,YSM} = 3.34\times10^4\exp\left(\frac{-10300}{T}\right) \tag{2-24c}$$

$$\sigma_{\mathrm{s,Int}} = 9.3 \times 10^5 \exp\left(\frac{-1100}{T}\right) \tag{2-24d}$$

The above equations are the expressions of the pure material conductivities. The effective conductivities of porous electrodes are also related to the composition of the electrodes and the micro structures. Therefore, the effective conductivities of porous electrodes, which consider not only the composition fraction of conducting material (V) but the structural parameters, porosity (ε) and tortuosity (τ), can be implemented as

$$\sigma_{\mathrm{s,a}}^{\mathrm{eff}} = \sigma_{\mathrm{s,Ni}} \cdot (1 - \varepsilon_{\mathrm{a}}) \cdot \frac{V_{\mathrm{Ni}}}{\tau_{\mathrm{a}}} \tag{2-25a}$$

$$\sigma_{\mathrm{s,c}}^{\mathrm{eff}} = \sigma_{\mathrm{s,LSM}} \cdot (1 - \varepsilon_{\mathrm{c}}) \cdot \frac{V_{\mathrm{LSM}}}{\tau_{c}} \tag{2-25b}$$

$$\sigma_{\mathrm{l,a}}^{\mathrm{eff}} = \sigma_{\mathrm{l,YSZ}} \cdot (1 - \varepsilon_{\mathrm{a}}) \cdot \frac{V_{\mathrm{YSZ}}}{\tau_{\mathrm{a}}} \tag{2-25c}$$

$$\sigma_{\mathrm{l,c}}^{\mathrm{eff}} = \sigma_{\mathrm{l,YSZ}} \cdot (1 - \varepsilon_{\mathrm{c}}) \cdot \frac{V_{\mathrm{YSZ}}}{\tau_{\mathrm{c}}} \tag{2-25d}$$

Due to the existence of interconnects in stacks, the bad contact between interconnects and electrodes can cause contact resistance which also decrease the stack performance. In order to simplify the calculation of the ohmic loss caused by contact resistance on the interface of interconnects and electrodes, the equivalent interconnect conductivity is derived in terms of the equivalent circuit,

$$\sigma_{\mathrm{s,Int}}^{\mathrm{eq}} = \frac{\mathrm{H_{rib}}}{\mathrm{ASR} + \frac{\mathrm{H_{rib}}}{\sigma_{\mathrm{s,Int}}}} \tag{2-26}$$

where $\sigma_{\mathrm{s,Int}}^{\mathrm{eq}}$ represents the equivalent interconnect conductivity adopted in modeling and $\mathrm{H_{rib}}$ is the height size of interconnect rib. The contact resistance

ASR is the contact resistance which is influenced by the contact of interconnects and electrodes. The value of ASR varies from 10 to 100 $\mathrm{m\Omega\,cm^2}$ reported by literatures [26, 76].

2.2.2 Momentum transport in channels and porous electrodes

The gas transport in channels and porous electrodes consists of convection and diffusion.

(1) Gas flow in channels

In channels, the gas flow obeys mass and momentum conservation, the mass conservation equation is written as Eq.(2-27) and the momentum conservation can be described by the Navier-Stokes equation as Eq.(2-28)

$$\nabla \cdot \left(\rho \vec{V}\right) = 0 \tag{2-27}$$

$$\rho\left(\vec{V} \cdot \nabla\right)\vec{V} = \nabla \cdot \left[-p\mathbf{I} - \frac{2}{3}\mu\left(\nabla \cdot \vec{V}\right)\mathbf{I}\right] + \vec{F} \tag{2-28}$$

where $\vec{F}$ is the vector of the volume force.

(2) Gas flow in porous electrodes

In porous electrodes, mass balance equation accounting for the mass source from electrochemical reactions can be written as

$$\nabla \cdot \left(\rho \vec{V}\right) = S_{\mathrm{m}} \tag{2-29}$$

where S_{m} is mass source and determined by the electrochemical reaction rate.

Darcy-Brinkman equation [77, 78] is utilized to describe the phenomena of

the momentum transport in porous media, therefore the momentum equation in porous electrodes can be transformed to

$$\frac{\rho}{\varepsilon}\left(\vec{V}\cdot\nabla\right)\frac{\vec{V}}{\varepsilon}=\nabla\cdot\left[-p\mathbf{I}-\frac{2}{3}\frac{\mu}{\varepsilon}\left(\nabla\cdot\vec{V}\right)\mathbf{I}\right]-\frac{\mu}{B_{\mathrm{p}}}\vec{V}+\vec{F} \tag{2-30}$$

here, ε is the porosity of electrodes, μ viscosity of the mixture of gases, and B_{p} is the permeability coefficient of the porous electrodes.

2.2.3 Mass transport

2.2.3.1 Governing equations

The mass transport in porous electrode are governed by the mass diffusion and convection equations and the governing equations can be written as

$$\frac{\varepsilon}{RT}\frac{\partial(x_{\mathrm{i}}p)}{\partial t}=-\nabla\cdot\overrightarrow{N_{\mathrm{i}}}+S_{\mathrm{i}} \tag{2-31}$$

In this steady state model, the left hand term can be neglected, and the Eq.(2-31) can be simplified as

$$\nabla\cdot\overrightarrow{N_{\mathrm{i}}}=\nabla\cdot\vec{J_{\mathrm{i}}}+\nabla\cdot\rho\vec{u}w_{\mathrm{i}}+S_{\mathrm{i}} \tag{2-32}$$

where $\nabla\cdot\vec{J_{\mathrm{i}}}$ is the flux of mass transfer of species i, $\vec{J_{\mathrm{i}}}$ is the flux of gas diffusion of species i in the porous media, x_{i} and w_{i} is the molar fraction and mass fraction of species i respectively, and S_{i} is the source term of the mass transport of species i and determined by the reaction rates of species in the porous electrodes.

For the gas transport in porous media, Fick's model is widely used to describe the flux of mass transfer of species with the advantages of simplicity and high accuracy[79]. The governing equations can be expressed as

$$\vec{J_{\mathrm{i}}} = -\frac{1}{RT}\sum D_{\mathrm{i}}^{\mathrm{eff}}\nabla(x_{\mathrm{i}}p) - D_{\mathrm{i}}^{\mathrm{T}}\frac{\nabla T}{T} \tag{2-33}$$

Where D^{eff} and D^{T} are the total effective diffusion coefficient and the thermal diffusion coefficient (considered to be zero in this thesis), respectively.

The total gas diffusion coefficient involves molecular diffusion coefficient and Knudsen diffusion coefficient, and can be calculated by Eq.(2-34)[80]

$$D_{\mathrm{ij}}^{\mathrm{eff}} = \left(\frac{1}{D_{\mathrm{m,ij}}^{\mathrm{eff}}} + \frac{1}{D_{\mathrm{k,i}}^{\mathrm{eff}}}\right)^{-1} \tag{2-34}$$

where $D_{\mathrm{m}}^{\mathrm{eff}}$ and $D_{\mathrm{k}}^{\mathrm{eff}}$ are the effective molecular diffusion coefficient and effective Knudsen diffusion coefficient, respectively. $D_{\mathrm{m}}^{\mathrm{eff}}$ can be determined by the following expression[81]

$$D_{\mathrm{m,ij}}^{\mathrm{eff}} = \frac{\varepsilon}{\tau}D_{\mathrm{m,ij}} = \frac{\varepsilon}{\tau}\frac{1.43\times10^{-3}T^{1.75}}{pM_{\mathrm{n}}^{1/2}\left(v_{\mathrm{i}}^{1/3}+v_{\mathrm{j}}^{1/3}\right)} \tag{2-35a}$$

$$M_{\mathrm{n}} = 2\left[\frac{1}{M_{\mathrm{i}}} + \frac{1}{M_{\mathrm{j}}}\right]^{-1} \tag{2-35b}$$

where ε and τ are porosity and tortuosity of the porous electrodes, respectively. v_{i} is the diffusion volume of species i, and summarized in Table 2.2 basing on the previous literature[81]. M_{i} is the molar mass of species i.

Table 2.2 Gas diffusion volume: ν_{i}

Species	Gas diffusion volume: ν_{i} $(\mathrm{mol/m^3})$
H_2	7.07×10^{-6}
H_2O	12.7×10^{-6}
N_2	17.9×10^{-6}
CO	18.9×10^{-6}
CO_2	26.9×10^{-6}
CH_4	23.2×10^{-6}
O_2	16.6×10^{-6}

The effective Knudsen diffusion coefficient $D_{\mathrm{k}}^{\mathrm{eff}}$ can be expressed as[82]

$$D_{\mathrm{k,i}}^{\mathrm{eff}} = \frac{\varepsilon}{\tau}\frac{d_{\mathrm{pore}}}{3}\sqrt{\frac{8RT}{\pi M_{\mathrm{i}}}} \tag{2-36}$$

where d_{pore} is the diameter of pore of electrodes.

2.2.3.2 Chemical reactions model

(1) Syngas fueled SOFC

For syngas fueled SOFC, the water gas shift reaction (WGSR) should be considered, and he formula is shown in Eq.(2-37).

$$\mathrm{CO} + \mathrm{H_2O} \leftrightarrow \mathrm{H_2} + \mathrm{CO_2} \tag{2-37}$$

The reaction rate of WGSR can be estimated with high accuracy by Young's model[40, 41, 83, 84]. The equations of reaction rate of WGSR are expressed as Eq.(2-38).

$$R_{\mathrm{WGSR}} = K_{\mathrm{sf}}\left(p_{\mathrm{H_2O}}p_{\mathrm{CO}} - \frac{p_{\mathrm{H_2}}p_{\mathrm{CO_2}}}{K_{\mathrm{ps}}}\right)\ (\mathrm{mol\ m^{-3}\ s^{-1}}) \tag{2-38a}$$

$$K_{\mathrm{sf}} = 0.0171\exp\left(\frac{-103191}{RT}\right)\ (\mathrm{mol\ m^{-3}\ Pa^{-2}\ s^{-1}}) \tag{2-38b}$$

$$K_{\mathrm{ps}} = \exp(-0.2935Z^3 + 0.6351Z^2 + 4.1788Z + 0.316) \quad \text{(2-38c)}$$

$$Z = \frac{1000}{T(\mathrm{K})} - 1 \quad \text{(2-38d)}$$

(2) Methane fueled SOFC

For methane fueled SOFC, not only methane steam reforming (MSR) reaction (mentioned above in Section 1.6.3) is involved in porous electrodes, but also WGSR should be considered. The formula of MSR reaction is expressed as follows

$$\mathrm{CH_4 + H_2O \leftrightarrow 3H_2 + CO} \quad \text{(2-39)}$$

The reaction rate of MSR reaction can also be calculated by the Young's model which was commonly used in modeling [40, 41, 83, 84]. The expressions of the MSR rate can be written as shown in Eq.(2-40)

$$R_{\mathrm{MSR}} = K_{\mathrm{rf}}\left(p_{\mathrm{CH_4}}p_{\mathrm{H_2O}} - \frac{(p_{\mathrm{H_2}})^3 p_{\mathrm{co_2}}}{K_{\mathrm{pr}}}\right) (\mathrm{mol\ m^{-3}\ s^{-1}}) \quad \text{(2-40a)}$$

$$K_{\mathrm{rf}} = 2395 \exp\left(\frac{-231266}{RT}\right) (\mathrm{mol\ m^{-3}\ Pa^{-2}\ s^{-1}}) \quad \text{(2-40b)}$$

$$K_{\mathrm{pr}} = 1.0267 \times 10^{10} \exp(-0.2513Z^4 + 0.3665Z^3 + 0.581Z^2 - 27.13Z + 3.277) (\mathrm{Pa^2}) \quad (2-40c)$$

2.2.4 Heat transfer

2.2.4.1 Governing equation

The general form of the governing equation for the heat transfer among the whole SOFC stack can be generalized as

$$\rho C_{\mathrm{p}} \vec{u} \cdot \nabla T = \nabla \cdot (k \nabla T) + S_{\mathrm{T}} \tag{2-41}$$

where C_{p} is the specific heat, k is the thermal conductivity, and S_{T} is the heat source contributed by all the losses, electrochemical reactions, and even electrochemical reactions.

The expression of the specific heat of gas mixture is

$$C_{\mathrm{p,g}} = \sum_{\mathrm{i}} (x_{\mathrm{i}} \cdot C_{\mathrm{p,i}}) \tag{2-42}$$

Here, the specific heat of single gas species i, $C_{p,i}$ can be calculated by [85]

$$C_{\mathrm{p,i}} = \sum_{k=1}^{7} a_{\mathrm{k}} \cdot (\frac{T}{1000})^{k} \tag{2-43}$$

where a_{k} is the parameter depending on the species and can be found in [85].

In the porous electrodes, the local temperature equilibrium is adopted which assumes that there is no temperature difference between solid phases and gas phases. Therefore, the first term can be neglected, and the governing equation for porous electrodes, interconnect and dense electrolyte can be simplified as

$$\nabla \cdot (-k \nabla T) = S_{\mathrm{T}} \tag{2-44}$$

The thermal conductivity k of porous electrodes can be given by

$$k = \varepsilon k_{\mathrm{g}} + (1 - \varepsilon) k_{\mathrm{s}} \tag{2-45}$$

where k_{g} is the thermal conductivity of gas mixture, given by

$$k_{\mathrm{g}} = \sum_{\mathrm{i}} (x_{\mathrm{i}} \cdot k_{\mathrm{i}}) \tag{2-46}$$

Here, the thermal conductivity of single gas species i, k_{i} can be estimated by

$$k_{\mathrm{i}} = 0.01 \cdot \sum_{k=1}^{7} c_{\mathrm{k}} \cdot \left(\frac{T}{1000}\right)^{k} \tag{2-47}$$

where c_{k} depending on species is given by[85].

Table 2.3 Physical parameters of solid components

	Specific heat ($\mathrm{J\ kg^{-1}\ K^{-1}}$)	Thermal conductivity ($\mathrm{W\ m^{-1}\ K^{-1}}$)
Anode	450	11
Cathode	430	6
Electrolyte	470	2.7
Interconnect	550	20

The specific heat[46] and thermal conductivity[86] of solid components are listed in Table 2.3.

2.2.4.2 Heat sources

Heat generated by the electrochemical reactions and the overpotentials in active electrodes are given by

$$Q_{\mathrm{er}} = \left(\phi_{\mathrm{s}} - \phi_{\mathrm{l}} - E_0^{\mathrm{OCV}} + T\frac{\Delta S_{\mathrm{er}}}{nF}\right) i \tag{2-48}$$

where ΔS_{er} is the enthalpy change of the electrochemical reactions. Here, the first term, as defined ahead, is the overpotential and stands for the irreversible losses, and the last term, which is the reversible loss, represents the heat produced by the electrochemical reactions.

Heat is also produced by the ohmic losses in other electronic conducting

solids, and expressed as

$$Q_{\text{ohm}} = \frac{\text{H}}{\sigma_{\text{eff}}} |\vec{i}|^2 \quad (2\text{-}49)$$

where H is the thickness of components and σ_{eff} is the effective conductivity and can be found in Eqs.(2-25) and (2-26).

Heat can be produced or consumed when there are chemical reactions in the stack. In syngas fed SOFC stacks, heat will be produced by the exothermic WGSR, and the heat can be calculated by

$$Q_{\text{WGSR}} = R_{\text{WGSR}} \times (-10.5 \times T + 4.5065 \times 10^4) \text{ (J/mol)} \quad (2\text{-}50)$$

In methane fed SOFCs, heat will not only be produced by the exothermic WGSR, but consumed by endothermic methane steam reforming reaction, and the heat can be expressed as

$$Q_{\text{MSR}} = R_{\text{MSR}} \times (0.0424 \times T - 226.5107) \times 10^3 \text{ (J/mol)} \quad (2\text{-}51)$$

2.3 Methods and model validation

2.3.1 Methods

The above governing equations are solved by Finite Element Method (FEM). The convergence condition is defined as the relative error below 0.001. The grid independence checking was conducted to maintain the variable difference between two cases below around 0.1%, and the final grid consists of 220,000

elements for the stack of 2mm width. The number of grid elements is linear with the stack width. The grid of a 2mm wide stack model is shown in Fig.2.3.

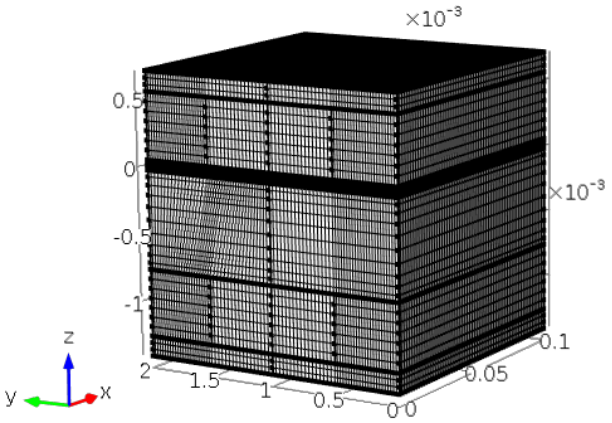

Figure 2.3 Grid of a 2mm wide stack model

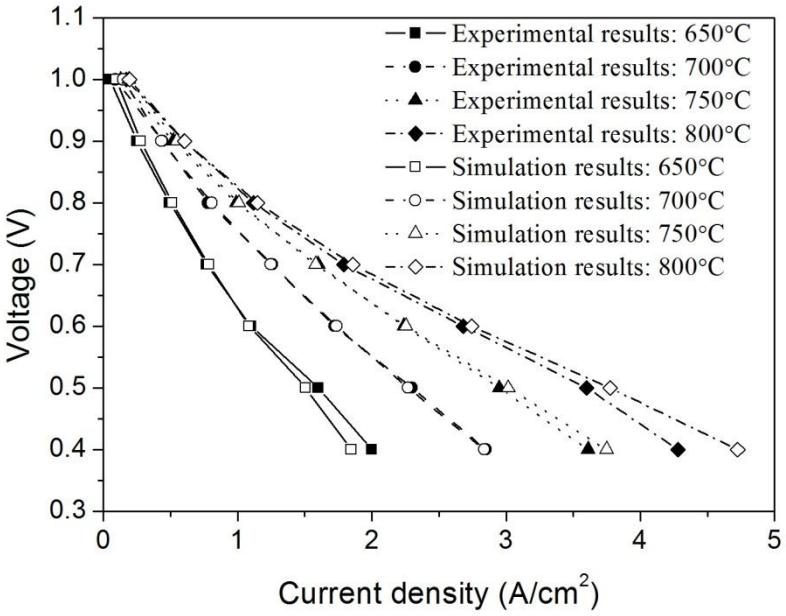

Figure 2.4 Comparison between simulation results and experimental results with temperatures from 650℃ to 800 ℃

2.3.2 Validation of electrochemical model

The hydrogen fed single SOFC model's numerical results are used to

validate the electrochemical model with the experimental data[87]. In the experiment, the thickness of Ni-YSZ anode, YSZ electrolyte and LSM + YSZ cathode is 750μm, 10μm and 50μm, respectively. The porosity of anode and cathode is 0.38 and 0.3 respectively. Hydrogen mixed with steam is fed to anode, and the hydrogen molar fraction of 0.9 is used in the model validation. Ambient air flows naturally onto the cathode surface and diffused to active sites through porous cathode. The validated models considered operation temperatures varying from 650 to 800℃. However, the temperature for one case is assumed to be constant for the whole cell domain since the cell is located in an oven and the oven keeps temperature constant during testing. The comparison between the results of modeling and experiments is illustrated in Fig.2.4. It indicates that the modeling results have good agreement with the experiment results over the voltage range of 0.9 to 0.6V (these voltages are normally used in practical applications and 0.7V is usually used for modeling). In addition, the agreement is also good for different operating temperatures.

CHAPTER 3 INTERCONNECT GEOMETRIC EFFECT ON HYDROGEN FED PLANAR SOFC STACKS

The three-dimensional model developed in Chapter 2 is used to model the hydrogen fed SOFC stack. The geometries of unit cell model are shown in Table 2.1 (Chapter 2). Co-flow pattern is adopted in this thesis. Fuel is consisted of 97% hydrogen and 3% water steam. Air is supplied in cathode channel. To maintain the fuel utilization and oxygen utilization at around 75% and 20% respectively, the proper fuel and air inlet flow rates at standard pressure and temperature (1atm, 25℃) are defined in Table 3.1 except for the parametric studies in Section 3.3.2. A symmetric interconnect design is applied in modeling, excluding the studies in Section 3.3.6. The operating parameters of the SOFC stack are illustrated in Table 3.2.

Table 3.1 The fuel and air inlet flow rates supplied to SOFC stack

Gas inlet flow rates, Q (ml/min)	W=2mm, Q^{ref}	W≠2mm
Fuel, Q_f	4.5	$W/2 \times Q_f^{ref}$
Air, Q_{air}	39	$W/2 \times Q_{air}^{ref}$

Table 3.2 Parameters used in modeling

Parameters	Values
Inlet temperature boundary	700℃
Inlet fuel and air pressure	1 atm
Cell voltage	0.7 V
Anode inlet fuel composition, $x_{H_2} + x_{H_2O}$	97% H_2+3% H_2O
Cathode inlet air composition, $x_{O_2} + x_{N_2}$	21% O_2+79% N_2
Anode porosity	0.38
Cathode porosity	0.3
ASR	$0.05\Omega cm^2$

3.1 Interconnect effect on stack performance

Comparing to the single cells, interconnects exist in SOFC stacks. As the existence of interconnect, the gas distributions and current density distribution will be strongly influenced. The gas distributions, temperature distribution and current density of a SOFC stack with 2 mm width and Ra of 0.5 are illustrated in Figs.3.1-3.5, respectively. Note that the SOFC stack with 2mm width, in this thesis, is supposed as a standard cell to demonstrate the stack performance.

As shown in Fig.3.1, hydrogen molar fraction decreases along gas flow direction (x direction) as hydrogen is consumed by electrochemical oxidation. H_2 molar fraction decreases gradually from channel to porous anode. As interconnect rib exists in stack, in porous anode H_2 molar fraction underneath the

interconnect rib is a little lower than that underneath the channel. Conversely, H_2O molar fraction underneath the interconnect rib is a little higher than that underneath the channel.

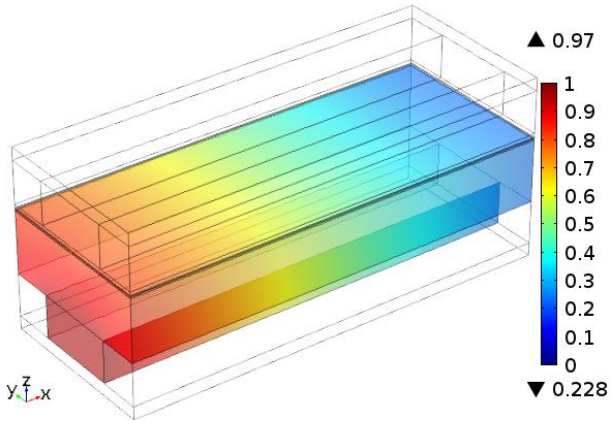

(a)

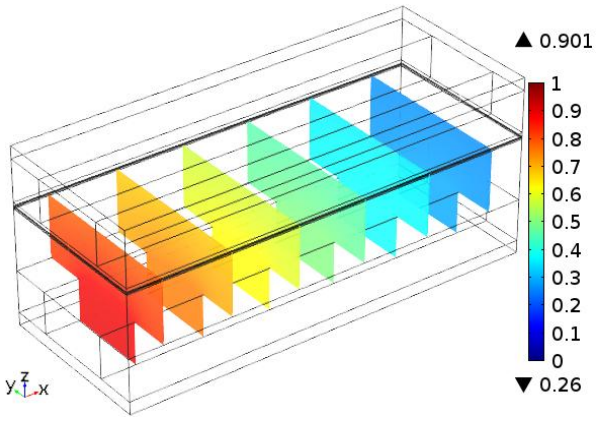

(b)

Figure 3.1 Hydrogen molar fraction: (a) volume, (b) slice

On the contrary to H_2, H_2O molar fraction increases along the gas flow direction (x direction) as it is produced by the electrochemical oxidation of H_2 (shown in Fig.3.2). In addition, H_2O molar fraction increases from the channel to the interface of anode and electrolyte, where H_2O is produced.

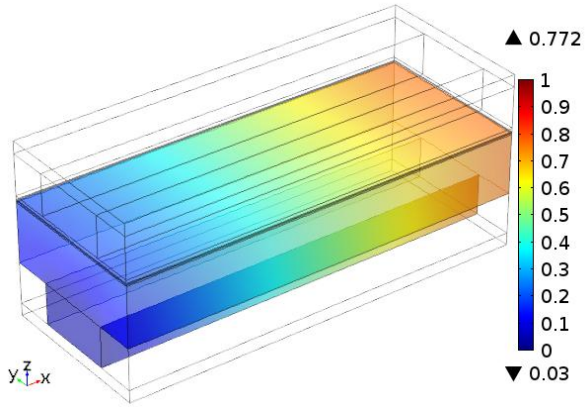

(a)

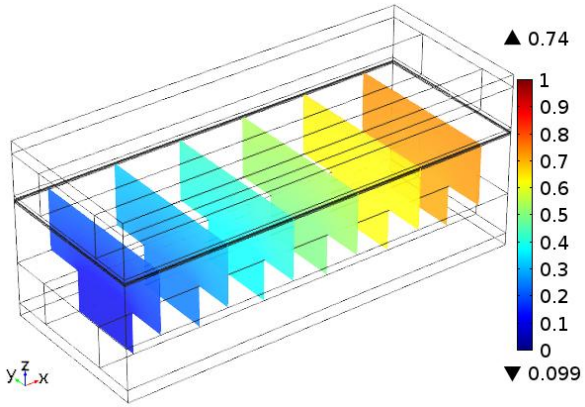

(b)

Figure 3.2 H_2O molar fraction: (a) volume, (b) slice

Similarly to H_2, O_2 molar fraction decreases along the gas flow direction (x direction) because O_2 is consumed by the electrochemical reaction. As interconnect exists in stack, in porous cathode, O_2 molar fraction underneath interconnect rib is obviously lower than that underneath channel as shown in Fig.3.3.

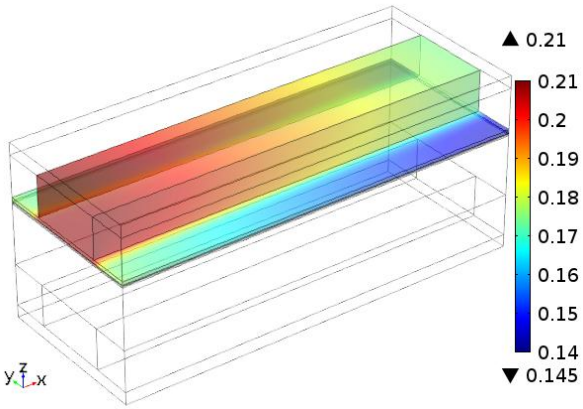

(a)

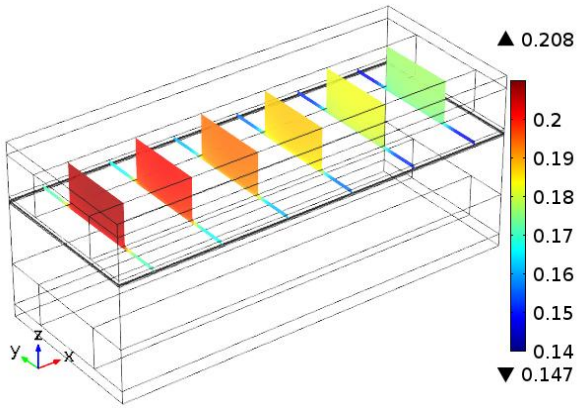

(b)

Figure 3.3 Oxygen molar fraction: (a) volume, (b) slice

As shown in Fig.3.4, temperature is comparatively uniform in the direction of cell thickness and width. However, temperature obviously increases along the gas flow direction (x direction) and the maximum temperature difference can reach about 80K. This temperature increase is big enough so that it should be considered. This temperature distribution indicates that the heat transfer should be considered in modeling of SOFC stack.

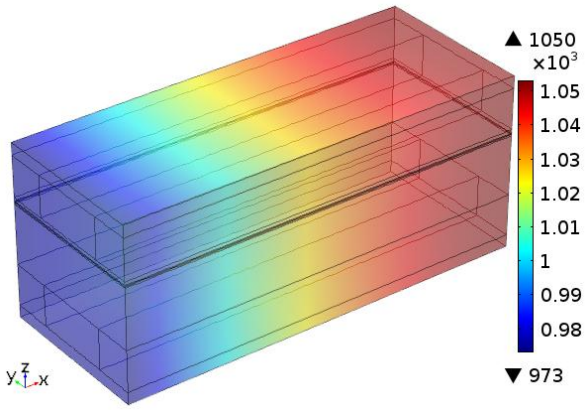

(a)

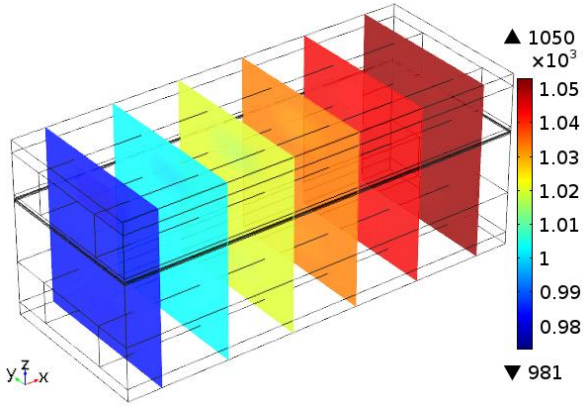

(b)

Figure 3.4 Temperature distribution (K): (a) volume, (b) slice

The influence on the stack performance caused by existence of interconnect rib can be reflected on the current density distribution. As shown in Fig.3.5, the current density underneath interconnect rib is much lower than that underneath channel. It may be caused by the lower H_2 and O_2 molar fraction underneath interconnect rib (referring to Figs.3.1 and 3.2).

In addition, along the gas channel (x direction), the current density firstly increases and then decreases gradually. The increase surrounding the inlet is

mainly contributed by the temperature increase. However, even though the temperature is still increasing, the current density further decreases gradually because the dramatic decrease of both of H_2 and O_2 molar fraction and increase of H_2O molar fraction lower the cell OCV (referring to Eq.(2-2))and also increase concentration loss (referring to Eqs.(2-16) and (2-17)).

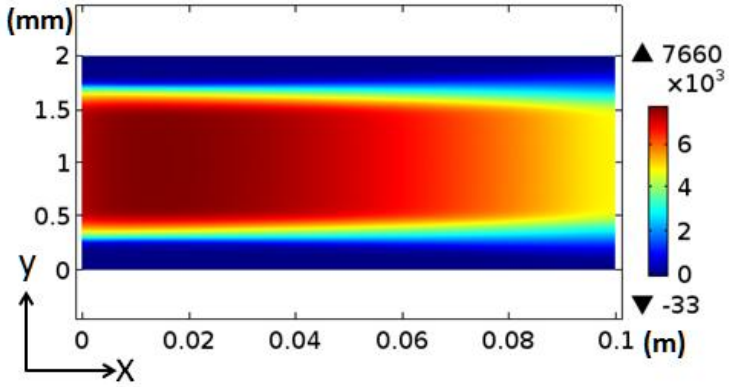

Figure 3.5 Current distribution on the interface of electrode and electrolyte (A/m^2)

3.2 Interconnect rib width effect on stack performance

Since interconnect rib width influences the gas diffusion path and electrons conducting path, when interconnect rib width varies, the gas diffusion resistance and electrons conducting resistance will correspondingly be influenced. Therefore, the stack performance will be influenced by interconnect rib width.

To primarily test the influence of interconnect rib width on the performance of SOFC stack, the fundamental parametric study on a standard cell is conducted and the results are demonstrated in Fig.3.6. In addition, a comparison study is conducted between models without heat transfer and with heat transfer.

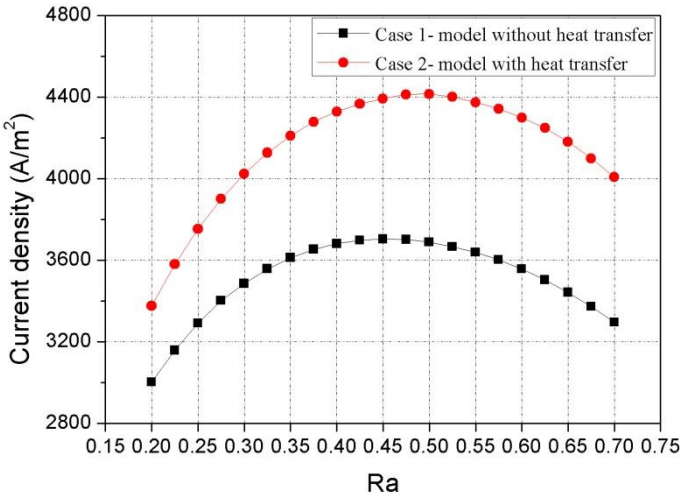

Figure 3.6 Effect of interconnect rib width Ra on current density of SOFC stack with 2mm width

As shown in Fig.3.6, the current density firstly increases gradually and then decreases with Ra in both cases. It turns out that the stack performance with optimum Ra can be improved by almost 30% compared to Ra of 0.2 in case 2. In addition, the peak current density of case 2 is about 19% higher than that of case 1 because the stack average temperature obtained by the model with heat transfer is higher than the operating temperature as mentioned in Fig.3.4. It also shows that the optimum Ra of 0.45 from the model without heat transfer is similar to the pervious result obtained by Liu et al [88], which can further validate the present model to some extent. However, when the operating temperatures are the same as high as 700℃, the optimum Ra of 0.5 obtained by the model with heat transfer is comparably larger than that obtained by the model without heat transfer. This can be explained from two aspects. On one hand, when the heat transfer is involved

in model, the cell temperature is increased along the channel with an increase of around 80K as shown in Fig.3.4. As mentioned above, the average current density obtained by the model with heat transfer is obviously bigger than that by the model without heat transfer which neglects the enhancement of the increase of temperature on the current density. Since the ohmic loss from the contact resistance between electrodes and interconnect ribs is increased with the increased average current density, a larger interconnect rib size is preferred to balance this increased ohmic loss by the contact resistance. On the other hand, the concentration loss is decreased by the increased temperature which provides the interconnect rib size space for becoming larger to balance ohmic loss. Overall, the optimum interconnect rib becomes larger when the model with heat transfer is applied. Furthermore, this result indicates that temperature change should be considered in SOFC stack modeling and the maximum temperature difference along the channel can reach around 80K.

The influence of interconnect rib size on stack performance can be reflected by the change of current density distribution on the surface of electrode as shown in Fig.3.7. Current density underneath interconnect is much lower than that underneath channel as mentioned in Section 3.1. Moreover, current density underneath interconnect decreases with Ra because concentration overpotential is

increased caused by the increase of reactant composition and the decrease of product composition. On the contrary, current density underneath channel increases with Ra. Therefore, current density distribution becomes more and more nonuniform when Ra increases.

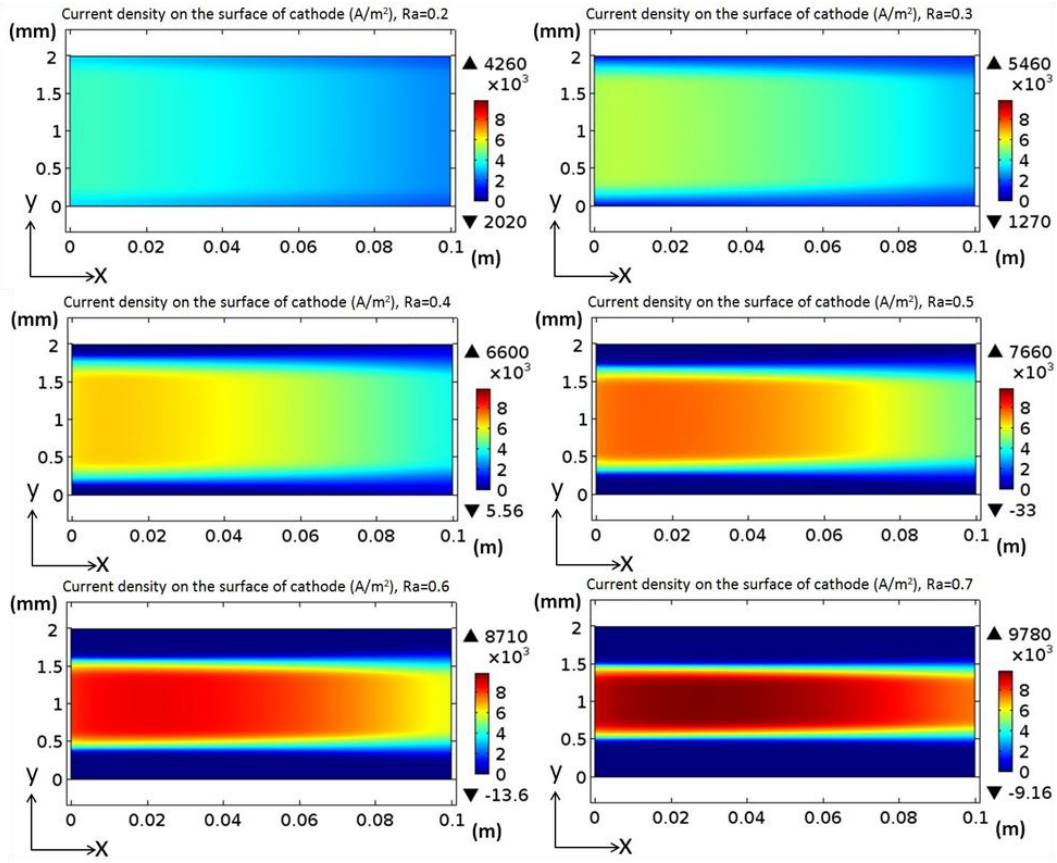

Figure 3.7 Current density distributions on the surface of cathode for stack with Ra varying from 0.2 to 0.7

3.3 Parametric studies

Since the optimum Ra is influenced by the geometric and operating parameters (i.e. porosity, gas inflow rates) of SOFC stack, parametric studies are conducted to find out the main factors effect on optimum Ra.

3.3.1 Optimum rib width Ra versus gas inlet flow rates

A parametric study of gas inlet flow rates was conducted and the results are shown in Fig.3.8. When both of fuel and air inlet flow rates vary in a proper range (0.8Q~1.2Q), the optimum Ra for stacks with different pitch width W is constant as shown in Fig.3.8(a). It indicates that when inlet flow rates in a proper range, the optimum Ra is independent on the inlet flow rates. As fuel utilization u_f and oxygen utilization u_a, dimensionless variables, are directly dependent on fuel inlet flow rates and air inlet flow rates respectively, it is reasonable to utilize u_f and u_a to represent the fuel inlet flow rates and air inlet flow rates respectively, in order to generalize this relationship between the optimum Ra and gas inlet flow rates. As shown in Fig.3.8, when both fuel and air inlet flow rate increase from 0.8Q to 1.2Q, u_f and u_a also increase. The u_f and u_a values for SOFC stack with 2mm width are between 0.65 and 0.88, and between 0.17 and 0.23 respectively. Therefore, when variation ranges of fuel utilization u_f and oxygen utilization u_a maintain around 10% and 3% respectively, the optimum Ra is independent on the gas inlet flow rates. Similarly, when gas inlet flow rates maintain constant for a SOFC stack with different interconnect rib width, the influence of variation of u_f and u_a on optimum Ra can also be neglected when u_f ($u_f \pm 10\%$) and u_a ($u_a \pm 3\%$) are in proper ranges.

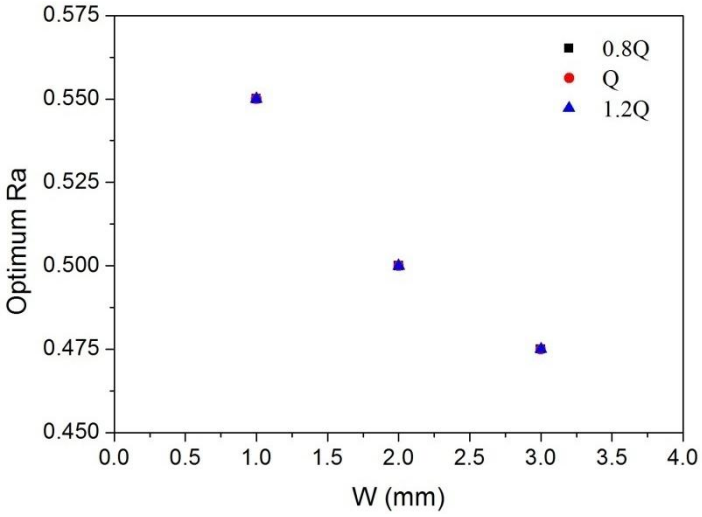

(a)

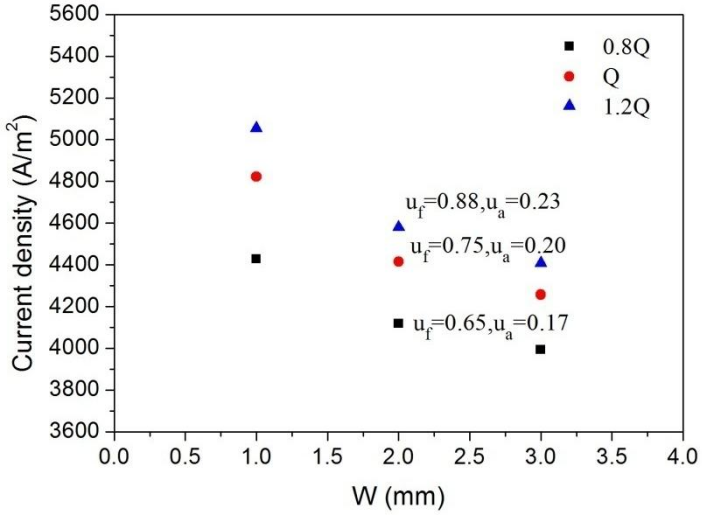

(b)

Figure 3.8 (a) Optimum Ra vs. width for different inlet flow rates, (b) current density for stacks with optimum Ra supplied by different inlet flow rates

3.3.2 Pitch width effect on optimum Ra

The optimum Ra, as shown in Fig.3.9 (a), decreases with pitch width when pitch width W $\leqslant$ 2.5mm, while it maintains constant when W > 2.5mm. As shown in Fig.3.9(b), u_f (around 0.75) and u_a (around 0.2) changes in a narrow range. According to the analysis in Section 3.3.1, the gas flow rates have no obvious effect on optimum Ra when gas utilization is in a proper range. When W

increases, the gas diffusion is more difficult from the area underneath channels to the area underneath interconnect rib since the gas flow distance becomes longer. Therefore, the interconnect rib width should become smaller to balance the increase of gas diffusion resistance caused by the increased pitch width.

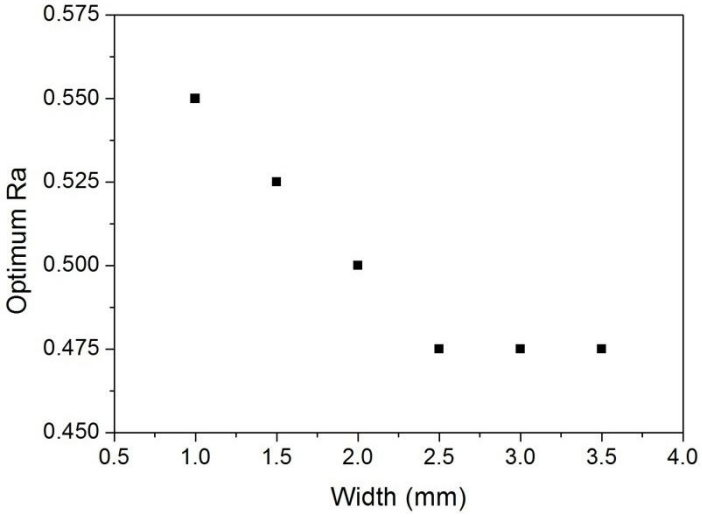

(a)

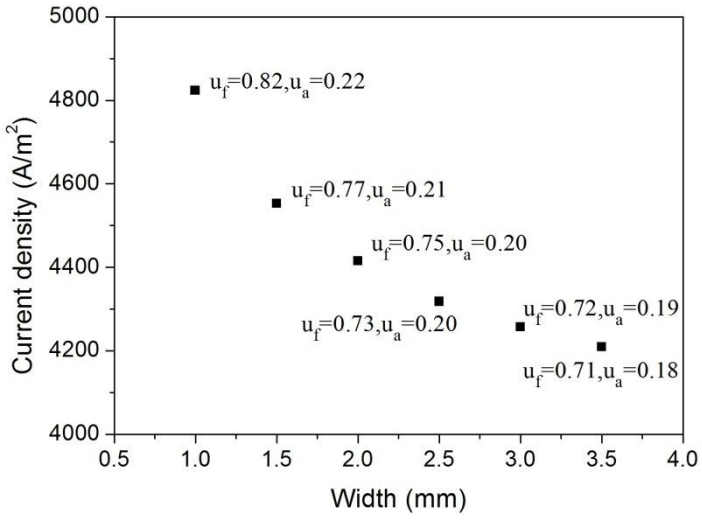

(b)

Figure 3.9 (a) Optimum Ra with stack pitch width, (b) current density of stacks with corresponding optimum Ra

In addition, the relationship between optimum Ra is linear with pitch width W for W≤ 2.5mm. While the optimum Ra is constant for W>2.5mm, it may be

because that the change of optimum rib width ratio is smaller than the interval of rib width ratio which is 0.025 used in this parametric study.

3.3.3 Optimum rib width Ra versus ASR

When ASR increases, the current density decreases due to the increase in ohmic loss as shown in Fig.3.10 (b).

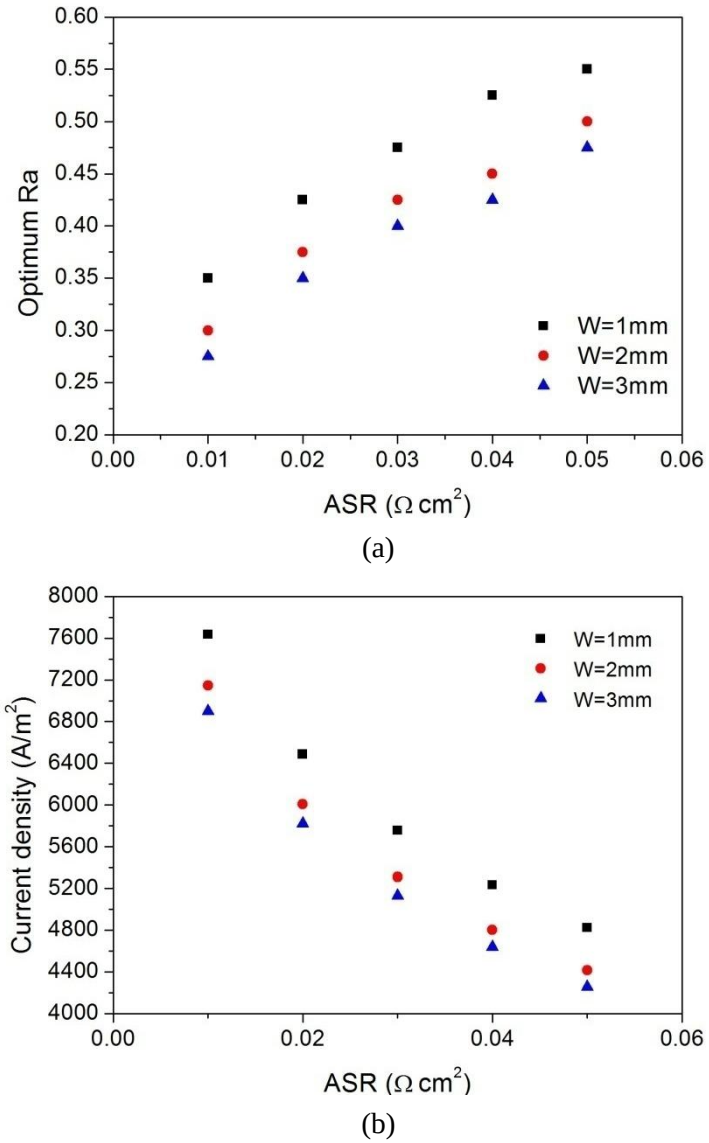

Figure 3.10 (a) Optimum Ra with ASR, (b) current density for stacks with optimum Ra

As aforementioned in Section 3.3.2, to exclude the influence of gas inlet

flow rates, the supplied gas inlet flow rates are correspondingly decreased with ASR to maintain u_f and u_a in suitable ranges. Due to the increase of ohmic loss with ASR, the interconnect rib width should become larger to balance the increased ohmic loss caused by the increase of ASR. Therefore, as shown in Fig.3.10 (a), the optimum Ra is increasing with ASR. In addition, the relationship between the optimum Ra and ASR is similarly linear.

3.3.4 Optimum rib width Ra with cathode porosity

Although the electric conductivity of electrodes decreases with porosity, the current density increases with cathode porosity increasing because the gas diffusion resistance is decreased with porosity increases, as shown in Fig.3.11(b). Since effective electric conductivity of electrode is decreasing when porosity increases (referring to Eq.(2-25)). Therefore, the electron conducting resistance becomes bigger when porosity is increasing. In the meanwhile, the ohmic loss caused by contact resistance between electrode and electrolyte also increases when current density increasing. Therefore, the total ohmic loss will be increased when porosity increases. However, the gas diffusion resistance will be decreased when porosity increases because the effective gas diffusion coefficient is increasing with porosity (referring to Eqs.(2-35) and (2-36)). On one hand, when porosity increases, the increased electron conducting resistance prefers larger

interconnect rib width to balance the increased ohmic loss. On the other hand, the decreased gas diffusion resistance has some space for interconnect rib width to become larger. Therefore, the optimum Ra increases with the cathode porosity increasing as shown in Fig.3.11 (a) and there is linear relationship between the optimum Ra and the cathode porosity.

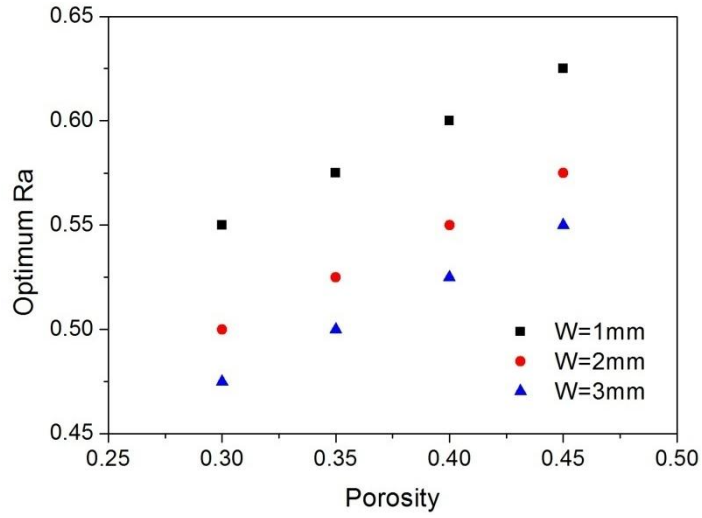

(a)

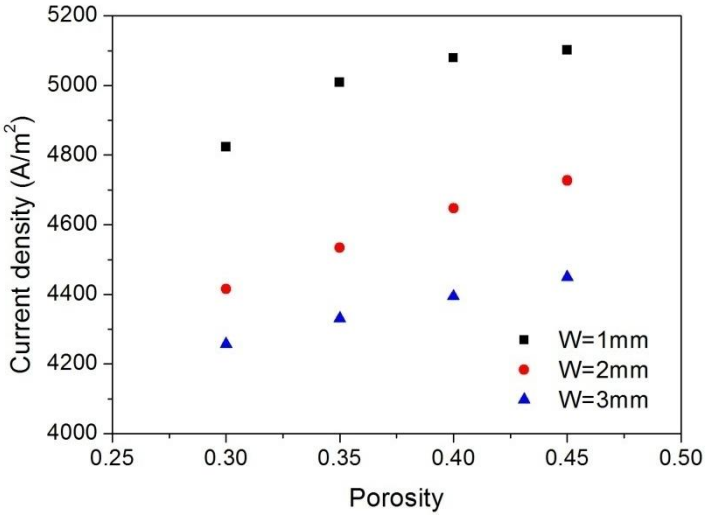

(b)

Figure 3.11 (a) Optimum Ra versus cathode porosity, (b) current density of SOFC stacks with corresponding Optimum Ra changing with cathode porosity

3.3.5 Optimum rib width Ra_a and Ra_c for stacks with asymmetric geometries

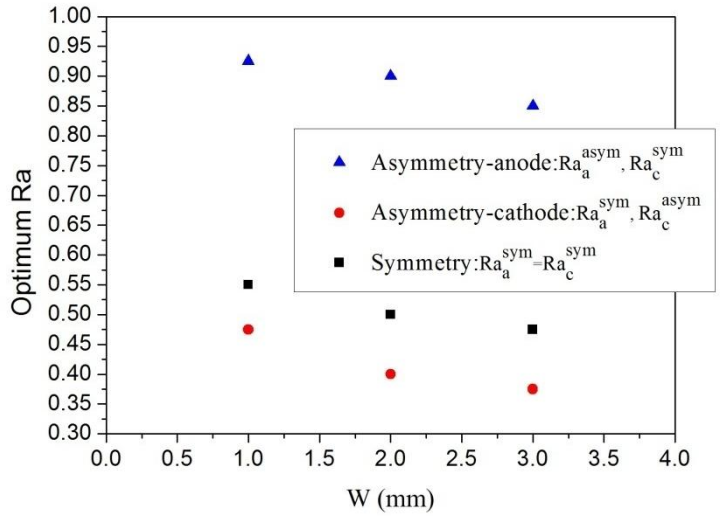

(a)

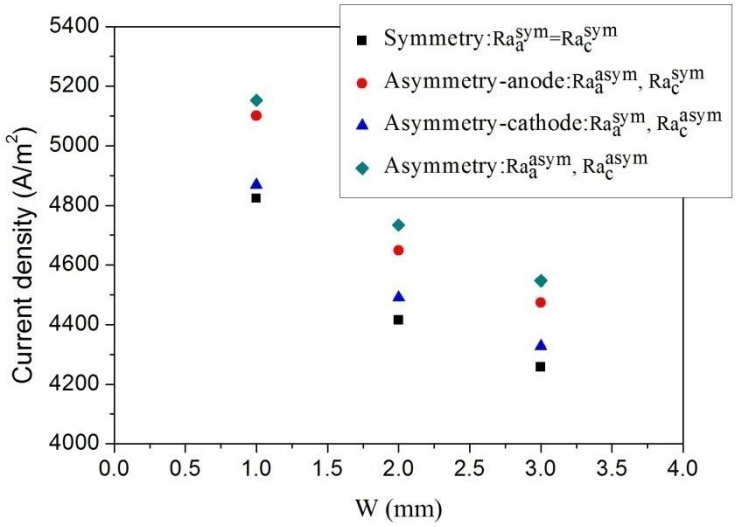

(b)

Figure 3.12 (a) Optimum Ra versus pitch width W for SOFC stacks with symmetric or asymmetric designs, (b) current density of SOFC stacks with corresponding Optimum Ra

As mentioned above, the optimum Ra is influenced by both the gas diffusion resistance and electron conducting resistance. For gas diffusion resistance, both anode and cathode gas diffusion contribute to this resistance.

However, the difference between gas diffusion resistance in anode and cathode is huge due to different gas species exist in anode side and cathode side respectively. The gas diffusion coefficient of H_2 and H_2O in anode side is larger compared to that of O_2 in cathode side as H_2 and H_2O have smaller molar mass (referring to Eqs.(2-35) and (2-36)). Therefore, considering this difference of gas diffusion coefficient between gas species on anode side and cathode side respectively, the optimum Ra for anode and cathode interconnect rib width may be different. Based on the above analysis, an asymmetric geometry design of interconnect rib in SOFC stack fed by H_2, which may probably further improve the stack performance, is proposed.

Parametric studies of SOFC stacks with asymmetric interconnect rib design are conducted. To find out the optimum anode interconnect rib of asymmetric designed SOFC stack Ra_a^{asym}, the cathode interconnect rib is optimum cathode interconnect rib of symmetric designed SOFC stack Ra_c^{sym}. Similarly, the anode interconnect rib is optimum anode interconnect rib of symmetric designed stack Ra_a^{sym} in the parametric study of cathode interconnect rib Ra_c^{asym} for asymmetric designed SOFC stack. Since the gas diffusion coefficient of H_2 and H_2O is relatively larger, the variation of the gas diffusion loss with interconnect rib width is smooth. On the contrary, the influence of interconnect rib width on

the electron conducting loss may be relatively stronger. Therefore, on the anode side, the SOFC stack performance (Fig.3.12(b)) can benefit by further increasing the anode interconnect rib width Ra_a due to the largely decreased electron conducting loss although there is a little increase in gas diffusion loss. It can also be found that in Fig.3.12(a) the optimum Ra_a^{asym} is larger than the optimum Ra_a^{sym}. However, it is contrary to the cathode side that the optimum Ra_c^{asym} is larger than the optimum Ra_c^{sym} as shown in Fig.3.12(a). Because the gas diffusion coefficient of O_2 is relatively small, the gas diffusion loss on the cathode side is sensitive to the interconnect rib width. Therefore, the cathode interconnect rib width can further be decreased to decrease the gas diffusion loss with sacrifice of slightly increased electron conducting loss in order to improve the SOFC stack performance as shown in Fig.3.12(b). So the optimum Ra_c^{asym} is smaller than the optimum Ra_c^{sym}. As shown in Fig.3.12(b), the SOFC stack achieves best performance when both of optimum anode rib width Ra_a^{asym} and cathode rib width Ra_c^{asym} are utilized in SOFC stack. Compared to symmetric design, this asymmetric design can further improve the stack performance by as high as 7%.

3.3.6 Empirical equations for predicting optimum Ra

Basing on the above parametric studies, empirical equations as shown in

Eq.(3-1) and (3-2) are derived to predict optimum Ra.

For H_2 fed SOFC stack with symmetric design, the optimum Ra can be estimated by

$$\mathrm{Ra} = \begin{cases} -0.05\mathrm{W} + 0.25\varepsilon_c - 5\mathrm{ASR} + 0.775, & \text{for W} \le 2.5\ \text{mm} \\ 0.65 + 0.25\varepsilon_c - 5\mathrm{ASR}, & \text{for W} > 2.5mm \end{cases} \quad (3\text{-}1)$$

where the pitch width W and area specific resistance ASR should be in units of mm and $\Omega\,\mathrm{cm}^2$, respectively and ε_c is cathode porosity.

Similarly, for H_2 fed SOFC stack with asymmetric design, the optimum Ra can be estimated by

$$\mathrm{Ra_a} = \begin{cases} -0.05\mathrm{W} + 0.25\varepsilon_c - 5\mathrm{ASR} + 1.175, & \text{for W} \le 2.5\ \text{mm} \\ 1.05 + 0.25\varepsilon_c - 5\mathrm{ASR}, & \text{for W} > 2.5mm \end{cases} \quad (3\text{-}2a)$$

$$\mathrm{Ra_c} = \begin{cases} -0.05\mathrm{W} + 0.25\varepsilon_c - 5\mathrm{ASR} + 0.675, & \text{for W} \le 2.5\ \text{mm} \\ 0.55 + 0.25\varepsilon_c - 5\mathrm{ASR}, & \text{for W} > 2.5mm \end{cases} \quad (3\text{-}2b)$$

3.4 CONCLUSIONS

The modeling of planar SOFC stack fed by H_2 is conducted in this chapter. As existence of interconnect rib in SOFC stack, both of gas diffusion and electron conducting are influenced. To optimize the interconnect rib width Ra, series of parametric studies are conducted. The findings are as follows.

(1) A comparative study between the model with heat transfer and the model without heat transfer is conducted, and the present study clearly indicates that heat transfer in SOFC stack modeling needs to be

considered for SOFC stack design optimization.

(2) Stack performance can be improved by almost 30% by optimizing the interconnect rib size.

(3) The optimum Ra is linear with pitch width W for W$\leqslant$ 2.5mm, while the optimum Ra is constant for W>2.5mm.

(4) The fuel utilization u_f and oxygen utilization u_a are utilized to clarify the influence of gas inlet flow rates on the optimum Ra. When u_f ($u_f\pm10\%$) and u_a ($u_f\pm3\%$) are in proper ranges, the optimum Ra is independent on the gas inlet flow rates.

(5) The optimum Ra is increasing with ASR and the relationship between the optimum Ra and ASR is similarly linear.

(6) The optimum Ra is increased with the cathode porosity increasing and there is linear relationship between the optimum Ra and the cathode porosity.

(7) A novel rib design (asymmetric interconnect rib design) is proposed in SOFC stack fed by H_2 considering the difference of gas diffusion coefficient between gas species in anode side and cathode side respectively. The optimum Ra_a^{asym} is larger than the optimum Ra_a^{sym}, while the optimum Ra_c^{asym} is smaller than the optimum Ra_c^{sym}. The

SOFC stack can obviously benefit when both of the optimum Ra_a^{asym} and Ra_c^{asym} are utilized in the asymmetric design. Compared to symmetric design, this asymmetric design can further improve the stack performance by as high as 7%.

(8) Simple empirical equations are derived to predict the optimum Ra, which make it convenient for practical geometric design of SOFC stack.

CHAPTER 4 INTERCONNECT GEOMETRIC EFFECT ON SYNGAS FED PLANAR SOFC STACKS

The three-dimensional model developed in Chapter 2 is used to model the syngas fed SOFC stack. In order to compare with H_2 fed SOFC stack, the geometries of unit cell model are same with H_2 fed SOFC stack shown in Table 2.1 (Chapter 2). Co-flow pattern is adopted in this thesis. Syngas consists of 45% H_2, 45% CO, 5% H_2O and 5% CO_2 in models excluding the parametric study model of syngas composition in Section 4.2.2. Air is supplied in cathode channel. Similarly to H_2 fed SOFC stack, to maintain the fuel utilization and oxygen utilization at around 75% and 20% respectively, the proper syngas and air inlet flow rates at standard pressure and temperature (1atm, 25℃) are defined in Table 4.1 except for the parametric studies in Section 4.3.2. A symmetric interconnect design is applied in modeling. The operating parameters of the SOFC stack are illustrated in Table 4.2.

Table 4.1 The fuel and air inlet flow rates supplied to SOFC stack

Gas inlet flow rates, Q (ml/min)	W=2mm, Q^{ref}	W≠2mm
Fuel, Q_f	4.4	$W/2 \times Q_f^{ref}$
Air, Q_{air}	35.4	$W/2 \times Q_{air}^{ref}$

Table 4.2 Parameters used in modeling

Parameters	Values
Inlet temperature boundary	700℃
Inlet fuel and air pressure	1 atm
Cell voltage	0.7 V
Anode inlet fuel composition, $x_{H_2} + x_{CO} + x_{H_2O} + x_{CO_2}$	45% H_2+45% CO +5% H_2O+5% CO_2
Cathode inlet air composition, $x_{O_2} + x_{N_2}$	21% O_2+79% N_2
Anode porosity	0.38
Cathode porosity	0.3
ASR	0.05Ωcm^2

4.1 Interconnect effect on stack performance

As mentioned above in section 4.1, the existence of interconnect in SOFC stacks has great effect on the gas distributions and current density distribution. The gas distributions, temperature distribution and current density of a SOFC stack with 2 mm width and Ra of 0.475 are illustrated in Figs.4.1-4.8, respectively.

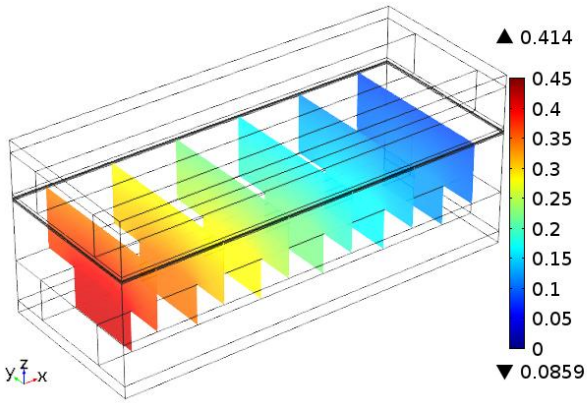

(a)

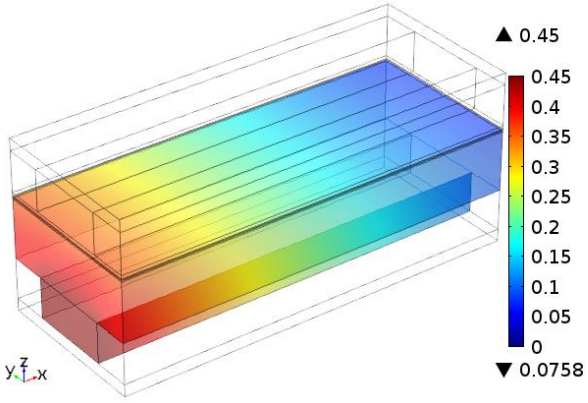

(b)

Figure 4.1 Hydrogen molar fraction: (a) volume, (b) slice

As shown in Fig.4.1, hydrogen molar fraction decreases along gas flow direction (x direction) as hydrogen is consumed by electrochemical oxidation. Although hydrogen is produced by water gas shift reaction, the rate of water gas shift reaction is greatly lower than that of H_2 electrochemical reaction. Therefore, H_2 molar fraction decreases along flow direction. On the contrary, H_2O molar fraction increases along the gas flow direction (x direction) as water is produced by the electrochemical oxidation of H_2 (shown in Fig.4.3) even though H_2O is also consumed by water gas shift reaction at a relatively low rate. H_2 molar

fraction decreases gradually from channel to porous anode. As interconnect rib exists in stack, in porous anode, H_2 molar fraction underneath the interconnect rib is a little lower than that underneath the channel. Conversely, H_2O molar fraction underneath the interconnect rib is a little higher than that underneath the channel.

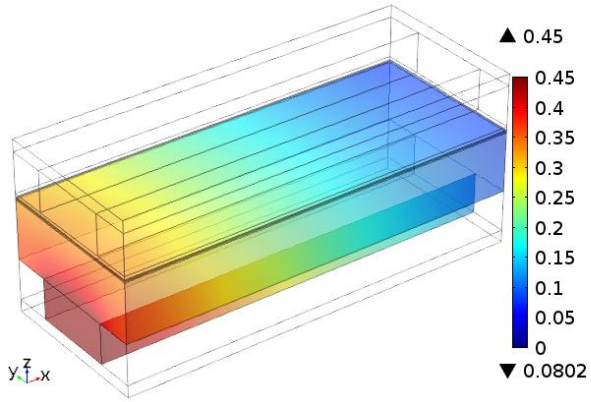

(a)

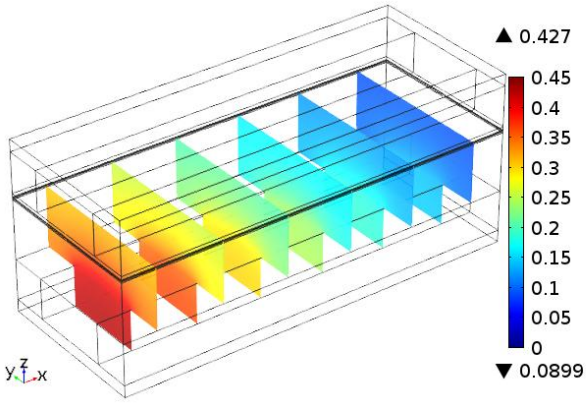

(b)

Figure 4.2 CO molar fraction: (a) volume, (b) slice

It is similar to H_2 that CO molar fraction decreases gradually along the fuel channel (x direction). However, CO is not only consumed by electrochemical

oxidation but also water gas shift reaction. As the product of CO electrochemical oxidation and gas shift reaction, CO_2 molar fraction increases along the fuel channel shown in Fig.4.4.

H_2 distribution in anode electrode is more uniform than CO, because H_2 has bigger gas diffusion coefficient and in the meanwhile H_2 is produced by water shift reaction in the whole anode.

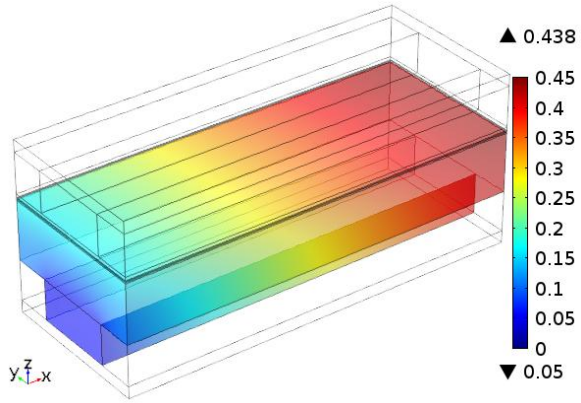

(a)

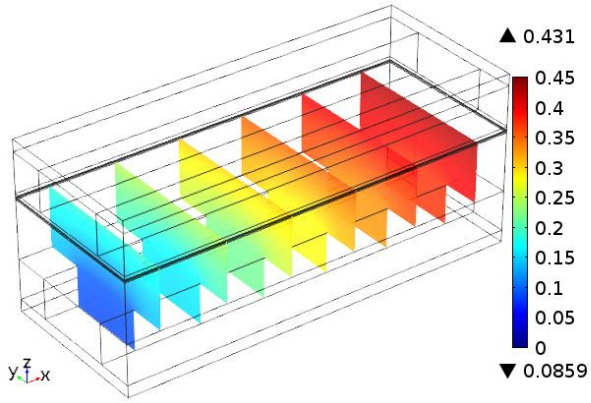

(b)

Figure 4.3 H_2O molar fraction: (a) volume, (b) slice

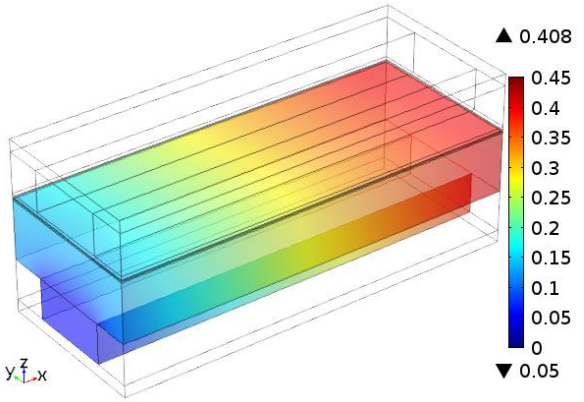

(a)

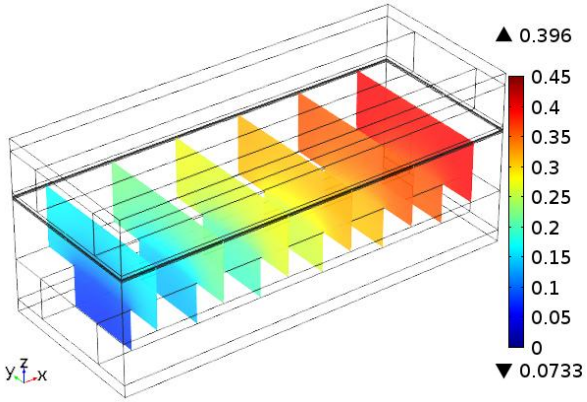

(b)

Figure 4.4 CO_2 molar fraction: (a) volume, (b) slice

As mentioned above, CO_2 is the product of CO electrochemical reaction and water shift reaction. Therefore, CO_2 increases along the gas flow direction and has higher molar fraction near the interface of anode and electrolyte where both reactions occur.

O_2 molar fraction decreases along the gas flow direction (x direction) because O_2 is consumed by the electrochemical reaction. As interconnect exists

in stack, in porous cathode, O_2 molar fraction underneath interconnect rib is obviously lower that underneath channel as shown in Fig.4.5. Also, O_2 molar fraction is lower near the interface of cathode and electrolyte where O_2 is consumed by electrochemical reaction.

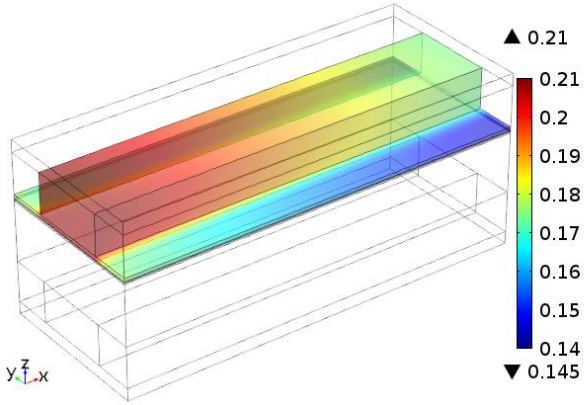

(a)

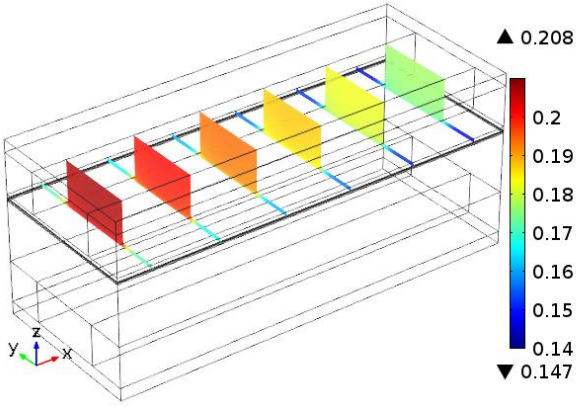

(b)

Figure 4.5 Oxygen molar fraction: (a) volume, (b) slice

As shown in Fig.4.6, temperature is uniform in the directions of cell thickness and width. However, temperature obviously increases along the gas flow direction (x direction) and the maximum temperature difference can reach almost 90K. The temperature increase is contributed by all the losses and the heat

released by water gas shift reaction. The temperature increase is big enough so that it should be considered. This temperature distribution further confirms that the heat transfer should be considered in modeling of SOFC stack.

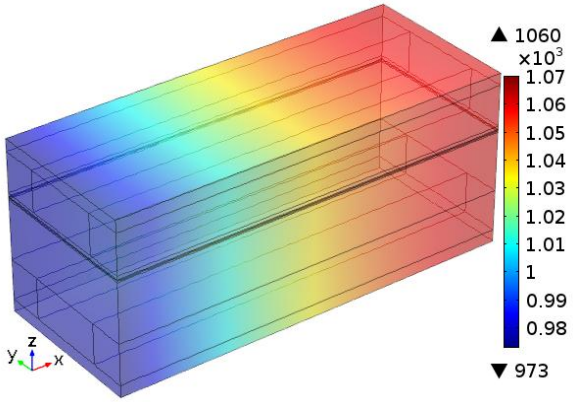

(a)

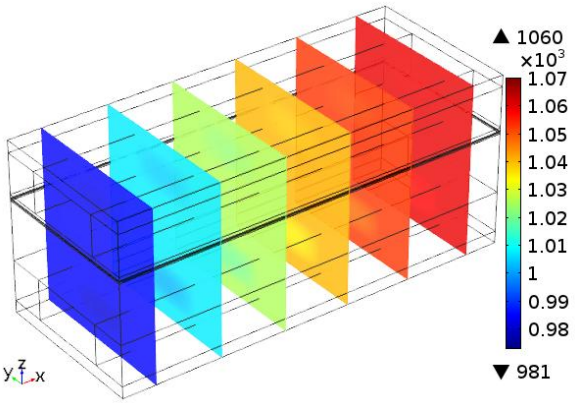

(b)

Figure 4.6 Temperature distribution (K): (a) volume, (b) slice

Fig.4.7 shows the rate of water gas shift reaction in the whole anode. The reaction rate is much higher near the interface of anode and electrolyte where fast consumption of H_2 and production of H_2O can promote this reaction. However,

the reaction rate is much lower underneath the interconnect rib where low CO molar fraction (as shown in Fig.4.2) deteriorates this chemical reaction.

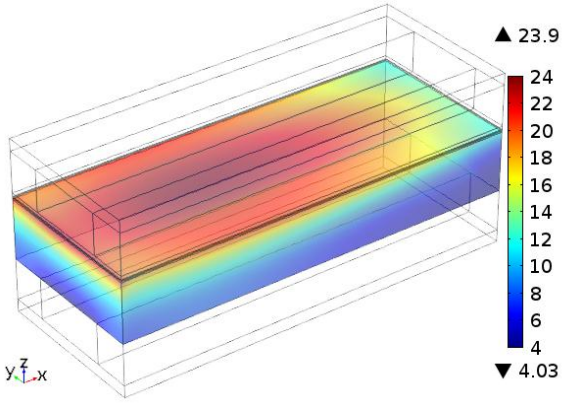

(a)

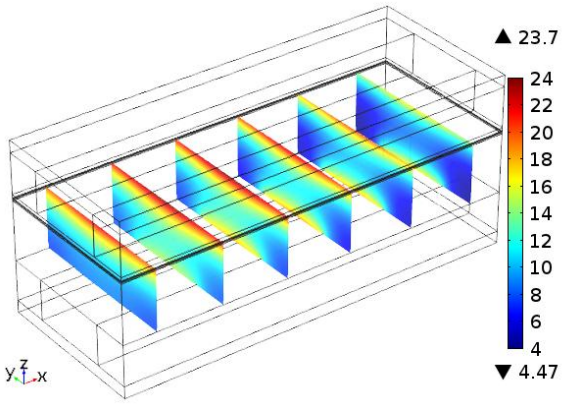

(b)

Figure 4.7 Rate of water gas shift reaction, R_{WGSR} (mol/s/m^3): (a) volume, (b) slice

The existence of interconnect rib also influences the current density distribution. As shown in Fig.4.8, the current density underneath interconnect rib is much lower than that underneath channel. It may be caused by the lower H_2, CO and O_2 molar fraction underneath interconnect rib (referring to Figs.4.1, 4.2

and 4.4).

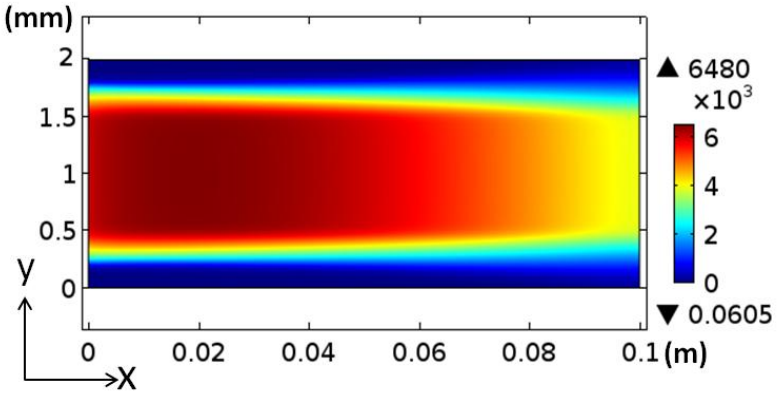

Figure 4.8 Current distribution on the interface of electrode and electrolyte (A/m^2)

In addition, along the gas channel (x direction), the current density firstly increases and then decreases gradually. The increase near the inlet is mainly contributed by the temperature increase. However, even though the temperature is still increasing, the current density further decreases gradually because both of the dramatic decrease in molar fractions of reactants (H_2, CO and O_2) and increase in molar fractions of products (H_2O and CO_2) lower the cell OCV (referring to Eq.(2-2))and also increase the concentration loss (referring to Eqs.(2-16) and (2-17)).

4.2 Parametric studies

4.2.1 Pitch width effect on optimum Ra

As shown in Fig.4.9(a), the variation tendency of optimum Ra for syngas

fed SOFC stack is similar with that for H_2 fed SOFC stack. When pitch width W $\leqslant$2.5mm, the optimum Ra is linear with W, while the optimum Ra keeps constant when W >2.5mm.

However, the optimum Ra of syngas fed SOFC stack is a little smaller than that of hydrogen fed SOFC stack. On one hand, compared to H_2, syngas has smaller gas diffusion coefficient due to bigger molar mass which results in bigger concentration loss (referring to Eqs.(2-34)-(2-36)). Thus, in terms of concentration loss, syngas fed SOFC stack desires slightly smaller interconnect rib width. On the other hand, since the current density of syngas fed SOFC is smaller than that of hydrogen fed SOFC as shown in Fig.4.9(b)) , the ohmic loss caused by contact resistance between interconnect ribs and electrodes is smaller, which further allows interconnect rib to become a little smaller in order to balance the increased concentration loss. From both perspectives of concentration loss and ohmic loss, the optimum Ra for syngas fed SOFC stack is a little smaller compared to that for H_2 fed SOFC stack.

The current density decreases with pitch width both for H_2 and CO as fuel (shown in Fig.4.9(b)), because both of the gas diffusion resistance and electron conducting resistance increase with pitch width increasing.

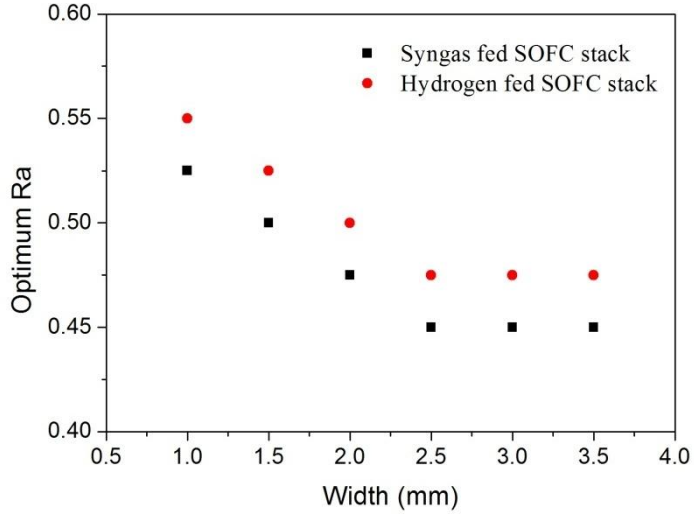

(a)

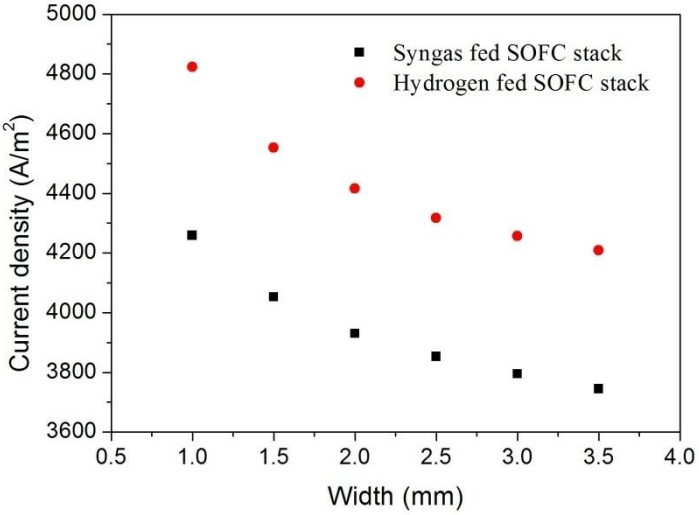

(b)

Figure 4.9 (a) Effect of pitch width W on optimum Ra, (b) the current density of SOFC stack with the corresponding optimum Ra

4.2.2 Syngas composition effect on optimum Ra

Syngas composition is normally changeable, so it is meaningful to investigate whether the optimum Ra is influenced by syngas composition especially the fuel composition (H_2 and CO) in syngas.

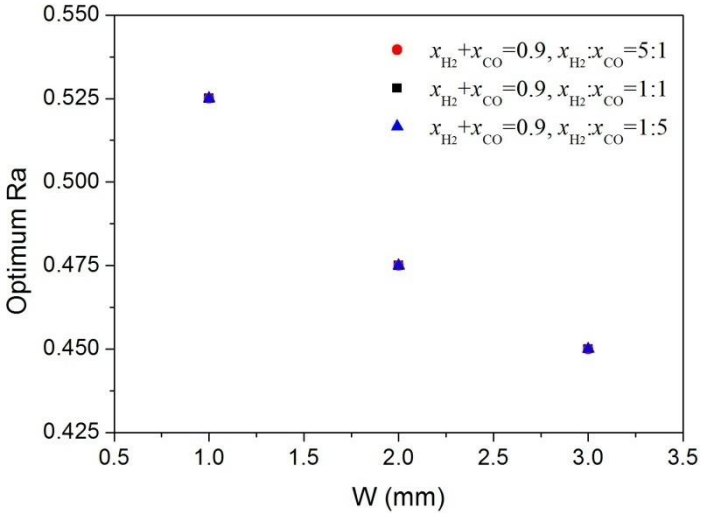

(a)

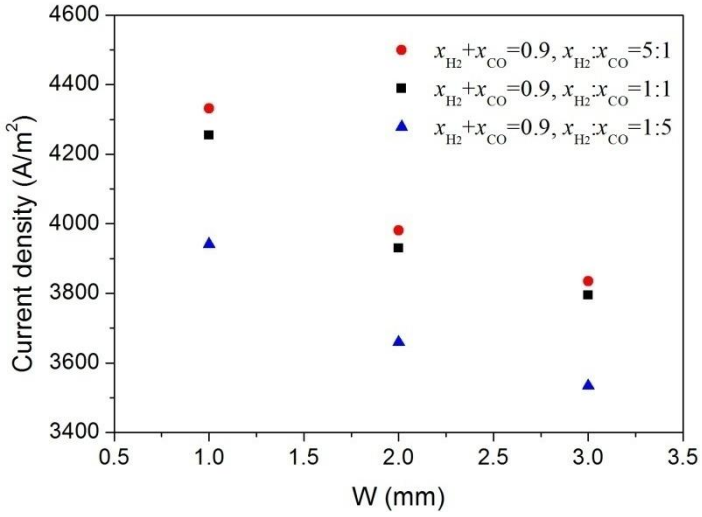

(b)

Figure 4.10 (a) Effect of syngas composition on optimum Ra, (b) current density of SOFC stack with corresponding optimum Ra

To find out the effect of syngas composition on the optimum Ra, parametric studies were conducted by varying the molar fraction ratio of H_2 to CO, $x_{H_2}:x_{CO}$, from 5:1 to 1:5 and keeping the total molar fraction of H_2 and CO, $x_{H_2}+x_{CO}$, at 0.9. When the molar fraction varies in a large range with H_2 from 0.75 to 0.15 and correspondingly CO from 0.15 to 0.75, the optimum Ra is not influenced.

Therefore, the effect of syngas composition on optimum Ra can be neglected. As shown in Fig.4.10(b), it is easy to understand that the current density increases with H_2 molar fraction increasing mainly because H_2 has higher electrochemical reaction rate and bigger diffusion coefficient compared with CO.

4.2.3 ASR effect on optimum Ra

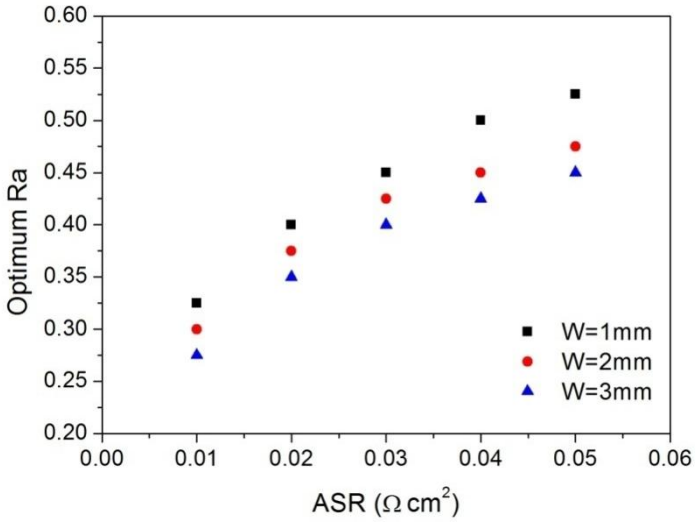

(a)

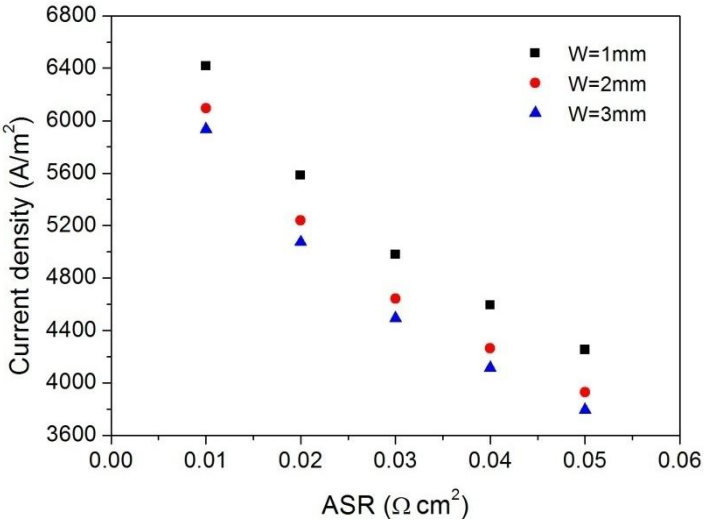

(b)

Figure 4.11 (a) Effect of ASR on optimum Ra, (b) current density of SOFC stack with corresponding optimum Ra with different ASR

When ASR increases, the current density decreases due to the increase in

ohmic loss as shown in Fig.4.11 (b). The ohmic loss increases with ASR increasing although the current density decreases with ASR. Due to the increase of ohmic loss with ASR increasing, the interconnect rib width should become larger to balance the increased ohmic loss caused by the increase of ASR. Therefore, as shown in Fig.4.11 (a), the optimum Ra is increasing with ASR. In addition, the relationship between the optimum Ra and ASR can be considered as approximately linear.

4.2.4 Cathode porosity effect on optimum Ra

As shown in Fig.4.12 (b), the current density increases with cathode porosity increasing because the gas diffusion resistance is decreasing with porosity, even though there is slight decrease in electric conductivity.

Since effective electric conductivity of electrode is decreasing when porosity increases (referring to Eq.(2-25)). Therefore, the electron conducting resistance becomes bigger when porosity is increasing. In the meanwhile, the ohmic loss caused by contact resistance between electrode and electrolyte also increases when current density increasing. Therefore, the total ohmic loss will be increased when porosity increases (referring to Eqs.(2-35) and (2-36)). However, the gas diffusion resistance will be decreased when porosity increases because the effective gas diffusion coefficient is increasing with porosity. On one hand,

when porosity increases, the increased electron conducting resistance prefers larger interconnect rib width to balance the increased ohmic loss. On the other hand, the decreased gas diffusion resistance has some space for interconnect rib width to become larger. Therefore, the optimum Ra increases with the cathode porosity increasing as shown in Fig.4.12 (a) and there is linear relationship between the optimum Ra and the cathode porosity.

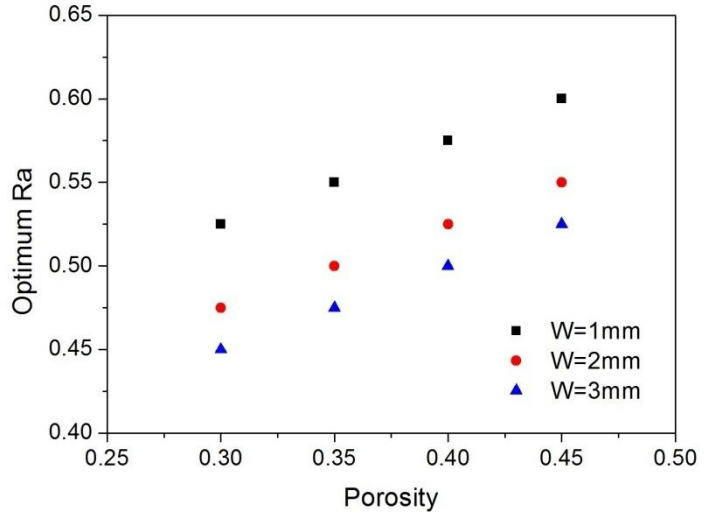

(a)

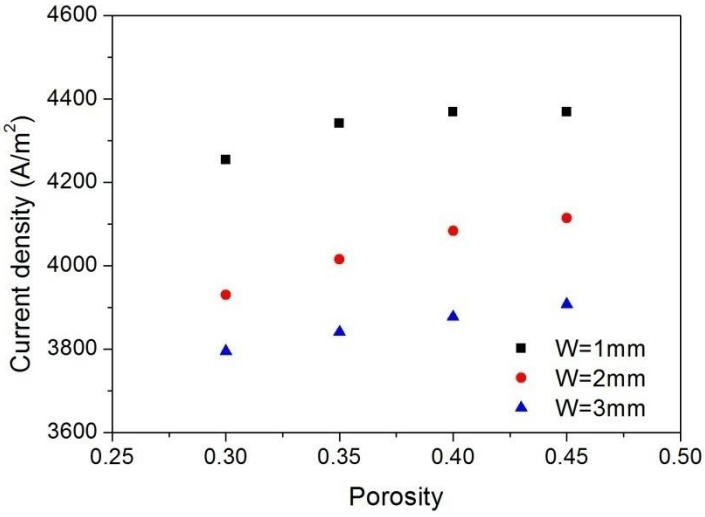

(b)

Figure 4.12 (a) Effect of cathode porosity on optimum Ra, (b) current density of SOFC stack with different cathode porosity and corresponding optimum Ra

4.2.5 Optimum rib width Ra_a and Ra_c for stacks with asymmetric geometries

The stack performance of SOFC fed by hydrogen can significantly benefit from the novel asymmetric geometric design as mentioned in Section 3.3.5. In this section, the asymmetric geometric design is also adopted in syngas fed SOFC stack and the optimization work of interconnect rib size is conducted.

Similarly to hydrogen fed SOFC stack, the optimum Ra_a^{asym} is larger than the optimum Ra_a^{sym} and the optimum Ra_c^{asym} is smaller than the optimum Ra_c^{sym}. Also, the SOFC stack achieves best performance when both of optimum anode rib width Ra_a^{asym} and cathode rib width Ra_c^{asym} are utilized in SOFC stack. The asymmetric geometric design can improve syngas fed SOFC stack by 1.5% compared to symmetric design. However, this improvement extent by adopting asymmetric geometry in syngas fed SOFC stack is much smaller than that in hydrogen fed SOFC stack. In syngas fed SOFC the difference of concentration overpotential between anode and cathode is smaller compared to hydrogen fed SOFC stack because anode concentration overpotential is larger in syngas fed SOFC stack. Therefore, the value of $Ra_a^{asym} - Ra_c^{asym}$ of syngas fed SOFC is smaller than that of hydrogen fed SOFC. This is the main reason why asymmetric geometric design has less improvement on syngas fed SOFC stack.

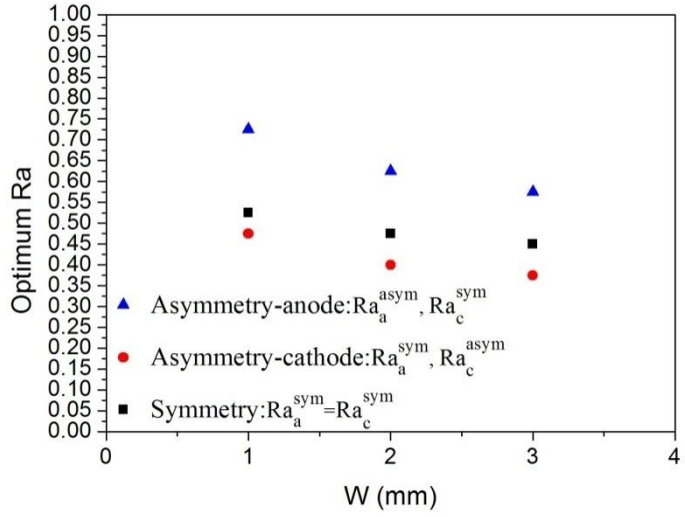

(a)

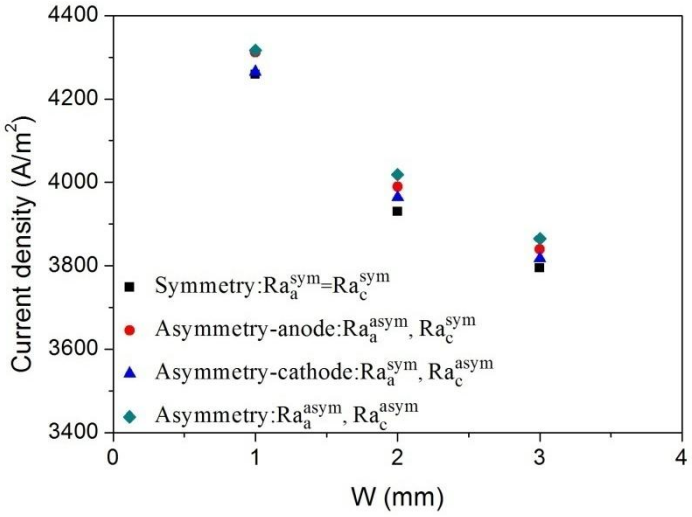

(b)

Figure 4.13 (a) Optimum Ra versus pitch width W for SOFC stacks with symmetric or asymmetric designs, (b) current density of SOFC stacks with corresponding Optimum Ra

4.2.6 Empirical equations for predicting optimum Ra

In order to provide an easy-to-use method for practical geometric designs of syngas fed SOFC stack, empirical equations are obtained basing on the above parametric studies, written in Eq.(4-1).

$$\mathrm{Ra} = \begin{cases} -0.05\mathrm{W} + 0.25\varepsilon_c - 5\mathrm{ASR} + 0.75, & \text{for W} \le 2.5\ \text{mm} \\ 0.625 + 0.25\varepsilon_c - 5\mathrm{ASR}, & \text{for W} > 2.5mm \end{cases} \quad (4\text{-}1)$$

where the units of the pitch width W and area specific resistance ASR are mm and $\Omega\,\mathrm{cm}^2$, respectively, and ε_c is cathode porosity.

Similarly, for syngas fed SOFC stack with asymmetric design, the optimum Ra can be estimated by

$$\mathrm{Ra_a} = \begin{cases} -0.1\mathrm{W} + 0.25\varepsilon_c - 5\mathrm{ASR} + 1, & \text{for W} \le 2.5\ \text{mm} \\ 0.75 + 0.25\varepsilon_c - 5\mathrm{ASR}, & \text{for W} > 2.5mm \end{cases} \quad (4\text{-}2a)$$

$$\mathrm{Ra_c} = \begin{cases} -0.05\mathrm{W} + 0.25\varepsilon_c - 5\mathrm{ASR} + 0.675, & \text{for W} \le 2.5\ \text{mm} \\ 0.55 + 0.25\varepsilon_c - 5\mathrm{ASR}, & \text{for W} > 2.5mm \end{cases} \quad (4\text{-}2b)$$

4.3 Conclusions

The modeling of planar SOFC stack fed by syngas is conducted in this chapter. As existence of interconnect rib in SOFC stack, both of the gas diffusion and electron conducting are influenced. To optimize the interconnect rib width Ra, series of parametric studies are conducted. The findings are as follows.

(1) The optimum Ra of syngas fed SOFC stack is a little smaller than that of H_2 fed SOFC stack.

(2) Similarly to H_2 fed SOFC stack, the optimum Ra is linear with pitch width W for W$\leqslant$ 2.5mm, while the optimum Ra is constant for W>2.5mm.

(3) Syngas composition has no influence on optimum Ra.

(4) The optimum Ra is increasing with ASR and the relationship between the optimum Ra and ASR is similarly linear.

(5) The optimum Ra is increased with the cathode porosity increasing and there is linear relationship between the optimum Ra and the cathode porosity.

(6) The asymmetric geometric design can improve syngas fed SOFC stack by 1.5% compared to symmetric design. However, this improvement extent by adopting asymmetric geometry in syngas fed SOFC stack is much smaller than that in hydrogen fed SOFC stack.

(7) Empirical equations are obtained to predict optimum Ra of syngas fed SOFC stack, which provides an easy-to-use method for practical geometric designs of syngas fed SOFC stack.

CHAPTER 5 INTERCONNECT GEOMETRIC EFFECT ON METHANE FED PLANAR SOFC WITH INTERNAL REFORMING

The three-dimensional model described in Chapter 2 is extended to model the methane fed SOFC stack with internal reforming. In order to compare results with that obtained in Chapter 3 and 4, the geometries of unit cell model are same with H_2 fed SOFC stack shown in Table 2.1 (Chapter 2). Co-flow pattern is adopted in this thesis. Considering eliminating the carbon deposition phenomenon in anode electrode, the gas mixture consisting of 33% CH_4 and 67% H_2O (molar fraction) is supplied to SOFC stack excluding the parametric study of inlet fuel composition in Section 5.2.2. Air is supplied in cathode channel. Since internal reforming is involved, the fuel utilization is much lower compared to hydrogen or syngas fed SOFC. The proper syngas and air inlet flow rates at standard pressure and temperature (1atm, 25℃) are defined in Table 5.1. Considering the temperature effect on the internal reforming reaction (referring to Eq.(2-40) in Chapter 2), CH_4 fed SOFC with internal reforming prefers higher operating temperatures. Thus, the inlet temperature of 800℃ is used in this modeling. A symmetric interconnect design is applied in modeling. The operating parameters of the SOFC stack are illustrated in Table 5.2.

Table 5.1 The fuel and air inlet flow rates supplied to SOFC stack

Gas inlet flow rates, Q (ml/min)	W=2mm, Q^{ref}	W≠2mm
Fuel, Q_f	3	$W/2 \times Q_f^{ref}$
Air, Q_{air}	30	$W/2 \times Q_{air}^{ref}$

Table 5.2 Parameters used in modeling

Parameters	Values
Inlet temperature boundary	8000℃
Inlet fuel and air pressure	1 atm
Cell voltage	0.7 V
Anode inlet fuel composition, $x_{CH_4} + x_{H_2O}$	33% CH_4+67% H_2O
Cathode inlet air composition, $x_{O_2} + x_{N_2}$	21% O_2+79% N_2
Anode porosity	0.38
Cathode porosity	0.3
ASR	0.05Ωcm^2

5.1 Interconnect effect on stack performance

As mentioned above in sections 3.1 and 4.1, the existence of interconnect in SOFC stacks has great effect on the gas distributions, current density distribution, temperature distribution and even chemical reactions (if any). Modeling of a

2mm wide SOFC stack with Ra of 0.5 is conducted to investigate the effect of interconnect on the performance of stack.

CH_4 is supplied to SOFC from the inlet and then diffuses to porous anode where with the catalysis of Ni it reacts with H_2O by methane steam reforming reaction. Therefore, as shown in Fig.5.1, CH_4 decreases gradually along the gas flow direction.

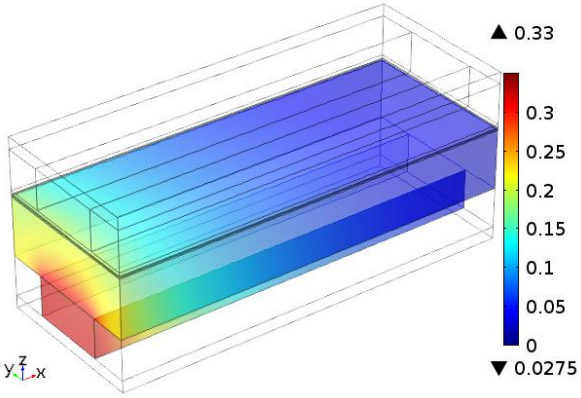

(a)

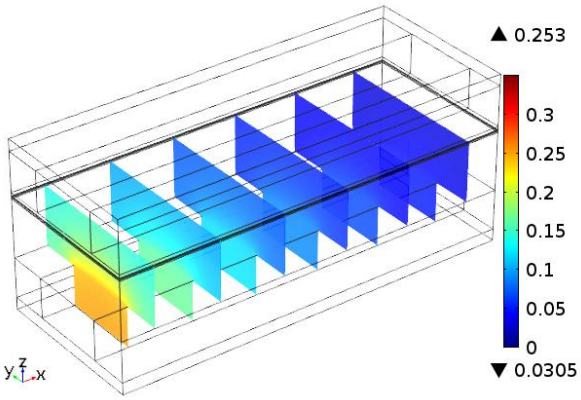

(b)

Figure 5.1 CH_4 molar fraction: (a) volume, (b) slice

In addition, CH_4 molar fraction underneath interconnect is much lower than that underneath channel because CH_4 needs to overcome bigger diffusion

resistance to reach that location.

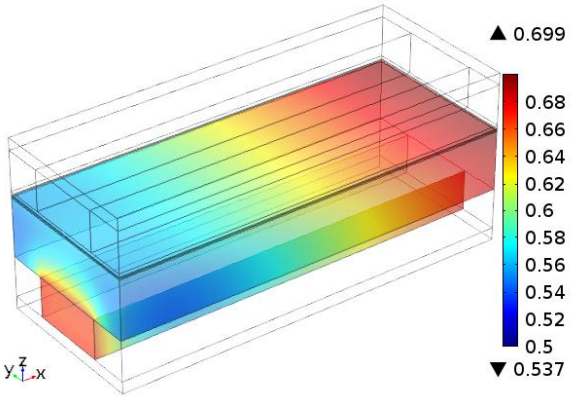

(a)

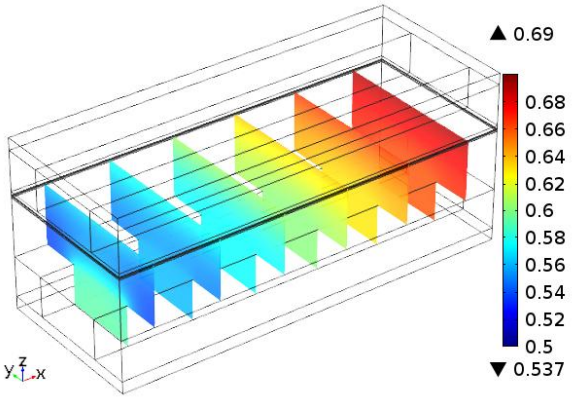

(b)

Figure 5.2 H_2O molar fraction: (a) volume, (b) slice

H_2O molar fraction distribution is shown in Fig.5.2. H_2O distribution along the channel can be clearly divided into two stages considering the H_2O consumption by MSR and WGSR and H_2O production by H_2 electrochemical oxidation. In the first stage, the channel has higher H_2O molar fraction than anode. H_2O diffuses into anode where dramatic MSR and WGSR occur (shown

in Figs.5.8 and 5.9) to produce large amount of H_2 and CO. Then, the produced H_2 and CO react with O^{2-} near the anode-electrolyte interface. In the second stage, conversely, H_2O molar fraction near anode-electrolyte interface is higher than that in the channel, because H_2O is produced and accumulates near the anode-electrolyte interface.

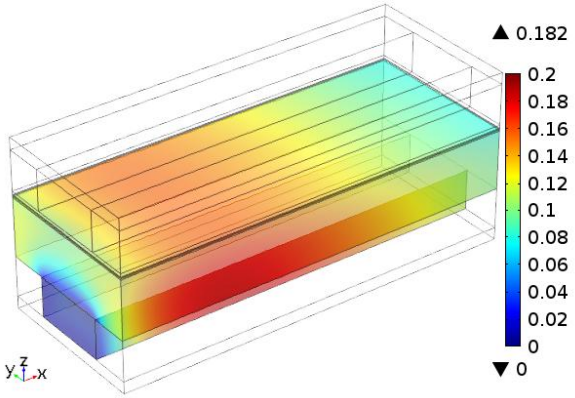

(a)

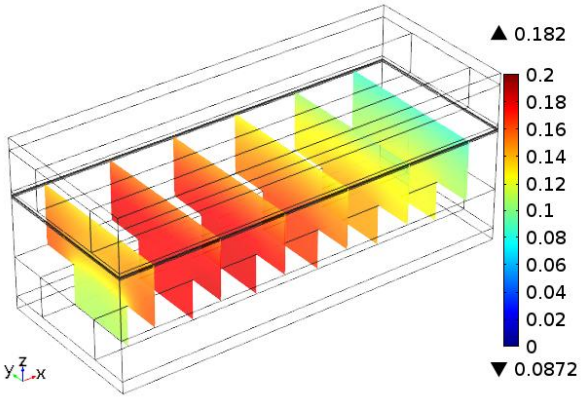

(b)

Figure 5.3 H_2 molar fraction: (a) volume, (b) slice

The distribution of H_2 molar fraction is rightly opposite with H_2O, because H_2 and H_2O always play opposite roles (reactant or product) in all involved reactions (MSR reaction, WGSR and H_2 electrochemical oxidation). Along gas

flow direction (x direction), H_2 firstly increases and then decreases in Fig.5.6. It is interesting to find that in the inlet part of anode H_2 underneath the interconnect shows higher molar fraction than that underneath channel. Therefore, in anode side, interconnect rib effect on concentration loss is weak. This is mainly resulted in by the extremely low electrochemical reaction rate of H_2 underneath the interconnect rib as illustrated in Fig.5.10 and relatively uniform H_2 production rate from MSR reaction and WGSR (shown in Figs.5.8 and 5.9, respectively).

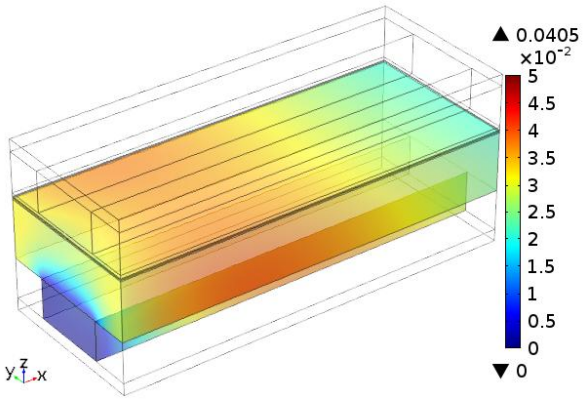

(a)

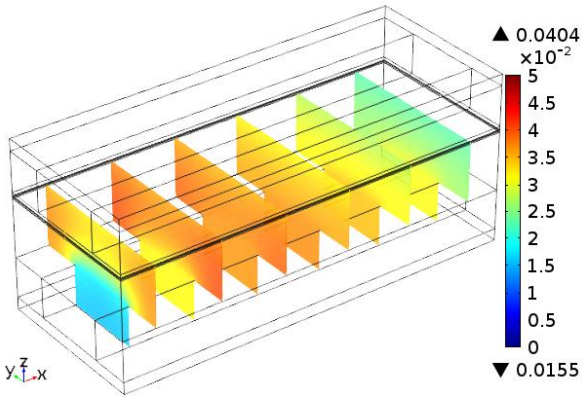

(b)

Figure 5.4 CO molar fraction: (a) volume, (b) slice

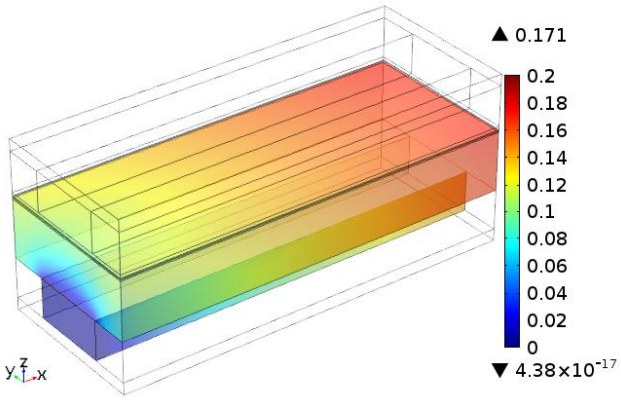

(a)

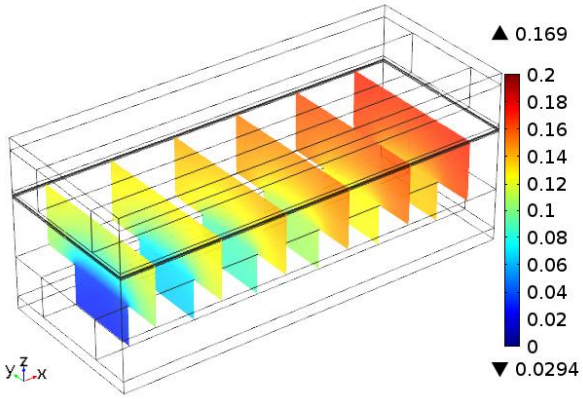

(b)

Figure 5.5 CO_2 molar fraction: (a) volume, (b) slice

As CO is not only the product of MSR reaction but also the reactant of WGSR and CO electrochemical oxidation, it increases firstly due to the dominant MSR reaction. However, as gas flows, it is consumed gradually by electrochemical oxidation which results in the decease of molar fraction showing in Fig.5.4. In addition, CO molar fraction underneath interconnect rib is slightly higher than that underneath channel.

CO_2 molar fraction increases along the gas channel as shown in Fig.5.5 because it is simultaneously produced by WGSR and CO electrochemical oxidation.

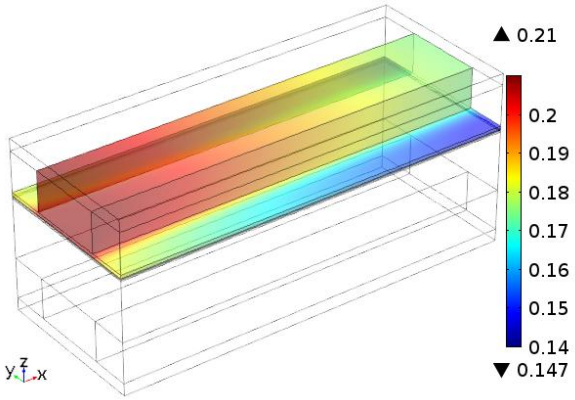

(a)

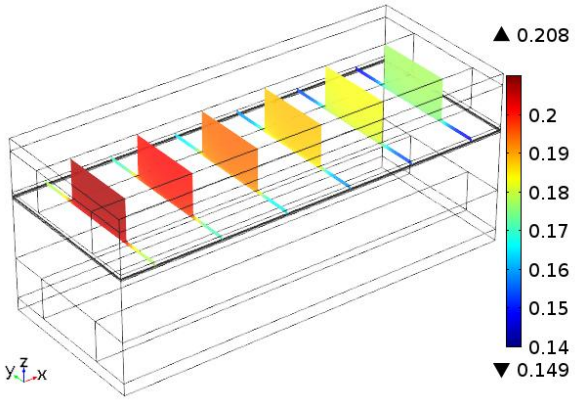

(b)

Figure 5.6 O_2 molar fraction: (a) volume, (b) slice

O_2 molar fraction decreases along the gas flow direction (x direction) because O_2 is consumed by the electrochemical reaction. As interconnect exists in stack, in porous cathode, O_2 molar fraction underneath interconnect rib is obviously lower that underneath channel as shown in Fig.5.6.

As shown in Fig.5.7, temperature distribution in methane fed SOFC is more

uniform than that in H_2 or syngas fed SOFC. In addition, along the gas flow direction (x direction), temperature firstly decreases because of the endothermic MSR reaction, and then increases due to heat from the cell losses. The temperature in the whole cell is lower than the operating temperature, which indicates MSR reaction in methane fed SOFC has cooling effect on the stack. In addition, the uniform temperature distribution further confirms the advantage of methane fed SOFC with internal reforming.

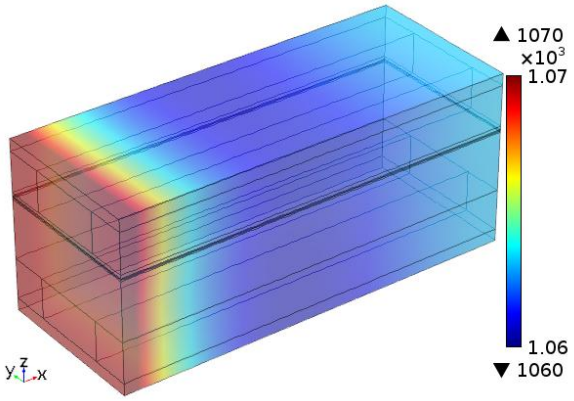

(a)

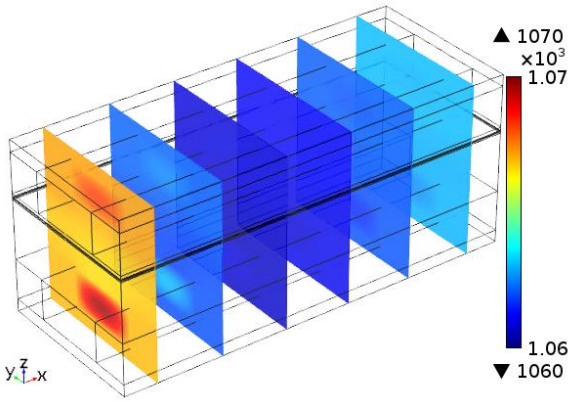

(b)

Figure 5.7 Temperature distribution (K): (a) volume, (b) slice

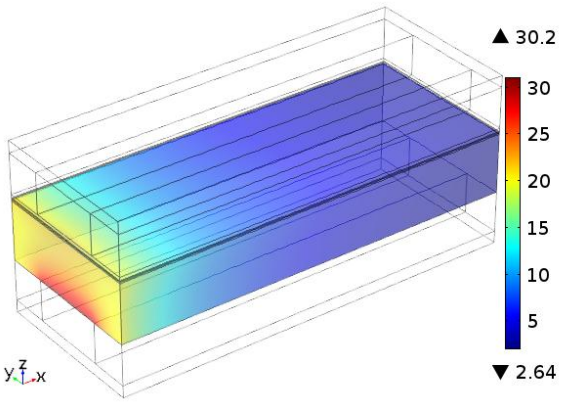

(a)

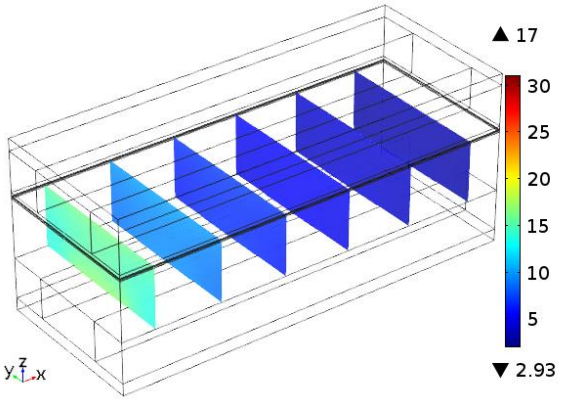

(b)

Figure 5.8 Rate of MSR reaction, R_{MSR} (mol/s/m^3): (a) volume, (b) slice

Figs.5.8 and 5.9 show the rates of MSR reaction and WGSR in the porous anode, respectively. The reactions occur dramatically at the inlet part of anode contributed by high reactants concentration and low products concentration. In addition, the rate of WGSR is much lower than that of MSR reaction which can further provide the proof of the cooling effect on the stack mentioned above. In addition, the reaction rate underneath the rib is slightly lower than that under channel, but the difference is relatively small.

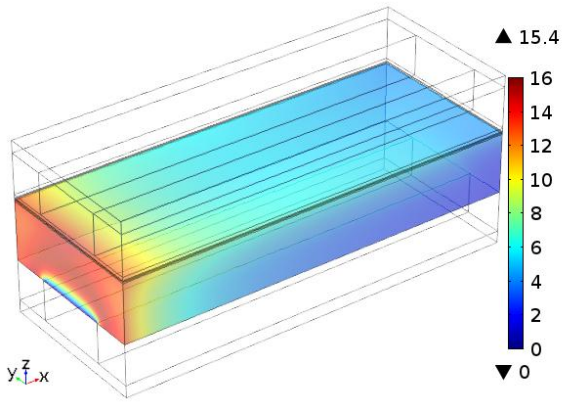

(a)

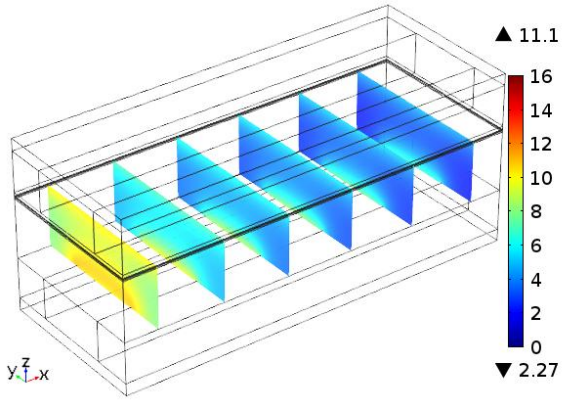

(b)

Figure 5.9 Rate of WGSR, R_{WGSR}(mol/s/m^3): (a) volume, (b) slice

The existence of interconnect rib also influences the current density distribution. As shown in Fig.5.10 the current density underneath interconnect rib is much lower than that underneath channel. Although H_2 and CO are relatively uniform in the x-y cross-section on anode side, O_2 molar fraction underneath interconnect rib, as mentioned above, is much lower underneath interconnect rib which mainly results in this no uniform current density distribution.

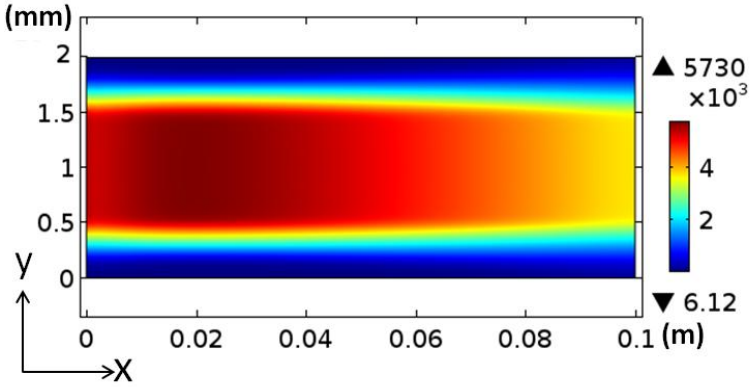

Figure 5.10 Current distribution on the interface of electrode and electrolyte (A/m^2)

In addition, along the gas channel (x direction), the current density firstly increases and then decreases gradually. The current density increases near the inlet where there are sharp increase of H_2 and CO concentration and decrease of H_2O. However, the current density further decreases gradually because both of the gradual decrease in molar fractions of reactants (H_2, CO and O_2) and increase in molar fractions of products (H_2O and CO_2) lower the cell OCV (referring to Eq.(2-2))and also increase the concentration loss (referring to Eqs.(2-16) and (2-17)).

5.2 Parametric studies

5.2.1 Width effect on optimum Ra

As shown in Fig.5.11(a), the variation tendency of optimum Ra for syngas fed SOFC stack is similar with that for H_2 fed SOFC stack. When pitch width W $\leqslant$2.5mm, the optimum Ra is linear with W, while the optimum Ra keeps

constant when W >2.5mm.

The current density decreases with pitch width as shown in Fig.5.11(b), because both of the gas diffusion resistance and electron conducting resistance increase with width increasing.

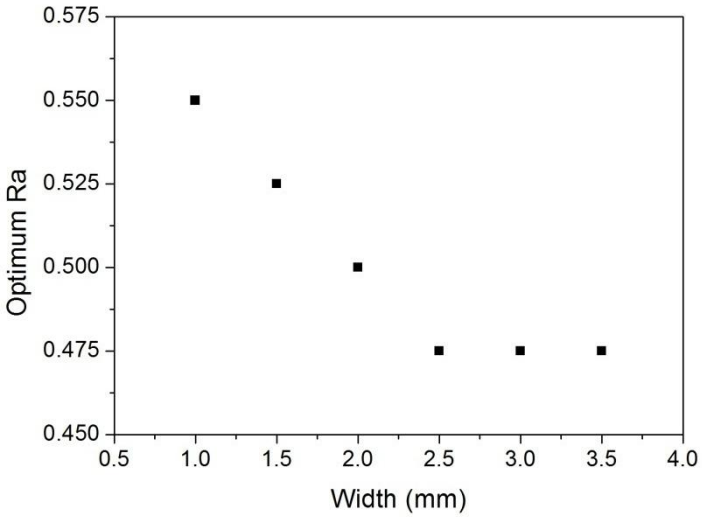

(a)

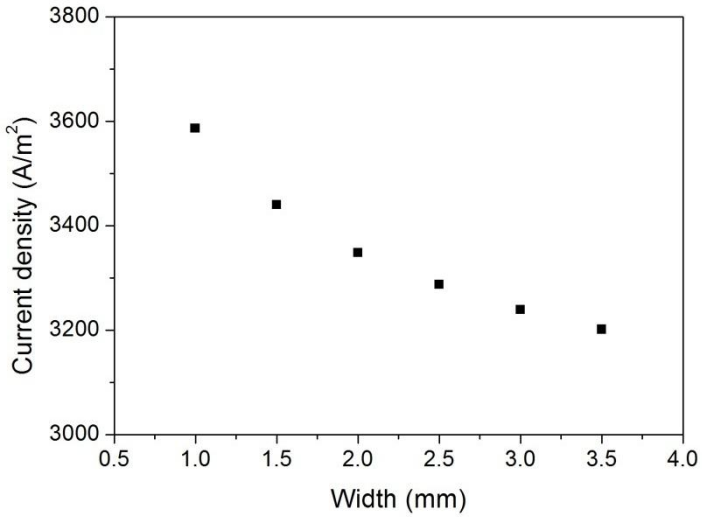

(b)

Figure 5.11 (a) Effect of pitch width W on optimum Ra, (b) current density of SOFC stack with the corresponding optimum Ra

5.2.2 Fuel composition effect on optimum Ra

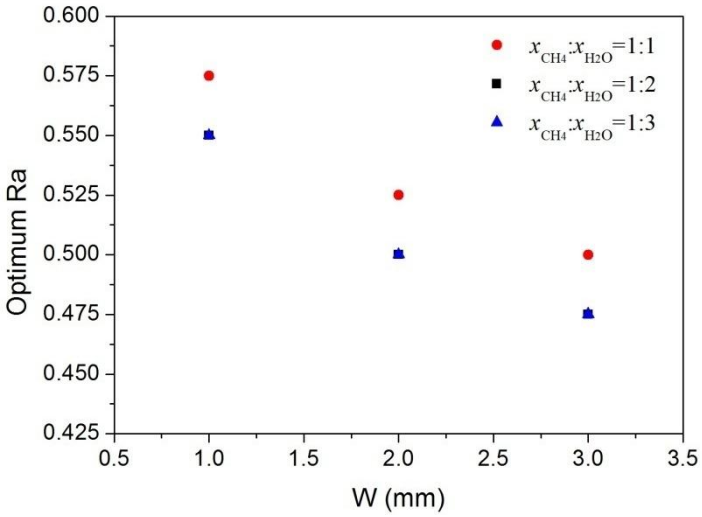

(a)

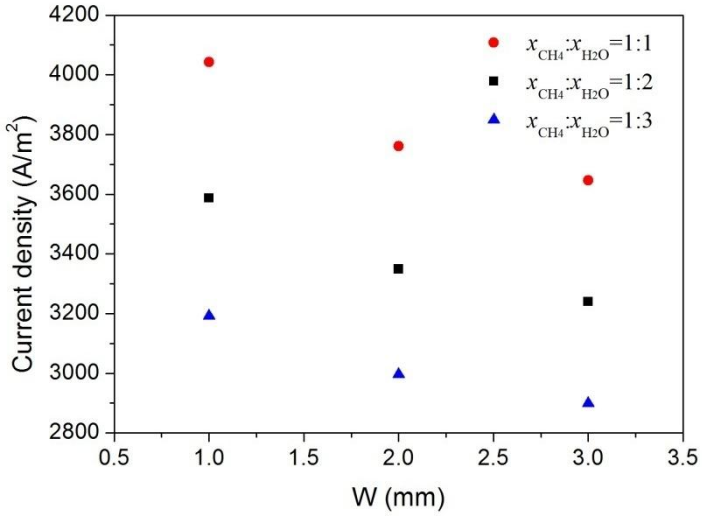

(b)

Figure 5.12 (a) Effect of fuel composition on optimum Ra, (b) current density of SOFC stack with the corresponding optimum Ra

The effect of fuel composition on optimum Ra is discussed. To block carbon deposition in porous anode, the ratio of molar fraction of CH_4 to that of H_2O (Carbon-Steam ratio) should be lower than 1:1. As shown in Fig.5.12 (a), the optimum Ra is increased by 0.025 when Carbon-Steam ratio is utilized. In this

condition, current density is much higher because of comparatively low H_2O molar fraction. Subsequently, the ohmic loss from ASR will be increased which needs wider interconnect rib to balance the increased ohmic loss. However, the fuel composition influences the optimum Ra only when CH_4 molar fraction is 0.5 which is almost the limit condition to prevent carbon deposition. Therefore, the effect of fuel composition can be neglected.

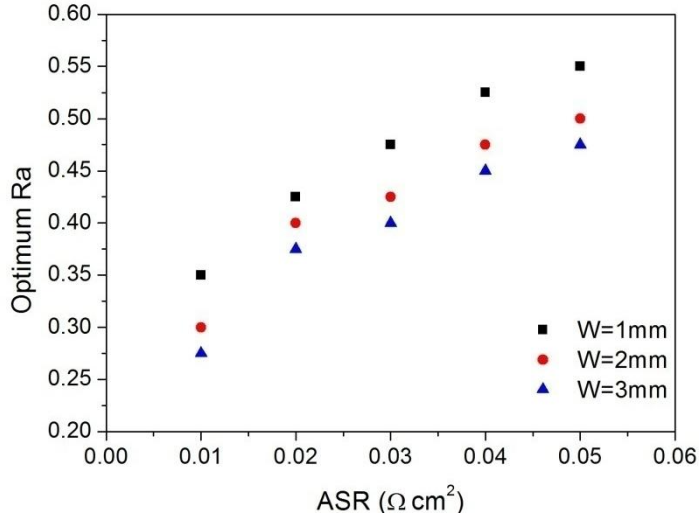

(a)

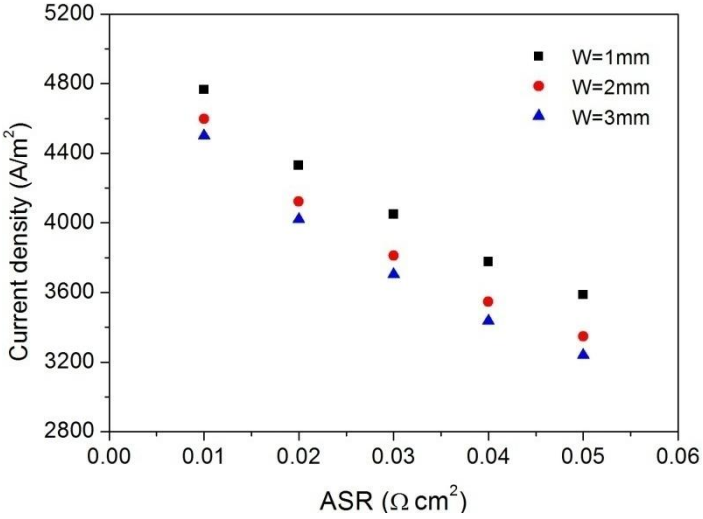

(b)

Figure 5.13 (a) Effect of ASR on optimum Ra, (b) current density of SOFC stack with corresponding optimum Ra varying with ASR

5.2.3 ASR effect on optimum Ra

When ASR increases, the current density decreases due to the increase in ohmic loss which is shown in Fig.5.13 (b). The ohmic loss increases with ASR increasing although the current density decreases with ASR. Due to the increase of ohmic loss with ASR increasing, the interconnect rib width should become larger to balance the increased ohmic loss caused by the increase of ASR. Therefore, as shown in Fig.5.13 (a), the optimum Ra is increasing with ASR. In addition, the relationship between the optimum Ra and ASR can be approximated to be linear.

5.2.4 Cathode porosity effect on optimum Ra

Although the electric conductivity of electrodes decreases with porosity, the current density increases with cathode porosity increasing because the gas diffusion resistance is decreased with larger porosity, as shown in Fig.5.14(b). Since effective electric conductivity of electrode is decreasing when porosity increases. Therefore, the electron conducting resistance becomes bigger when porosity is increasing. In the meanwhile, the ohmic loss caused by contact resistance between electrode and electrolyte also increases when current density increasing (referring to Eq.(2-25)). Therefore, the total ohmic loss will be

increased when porosity increases.

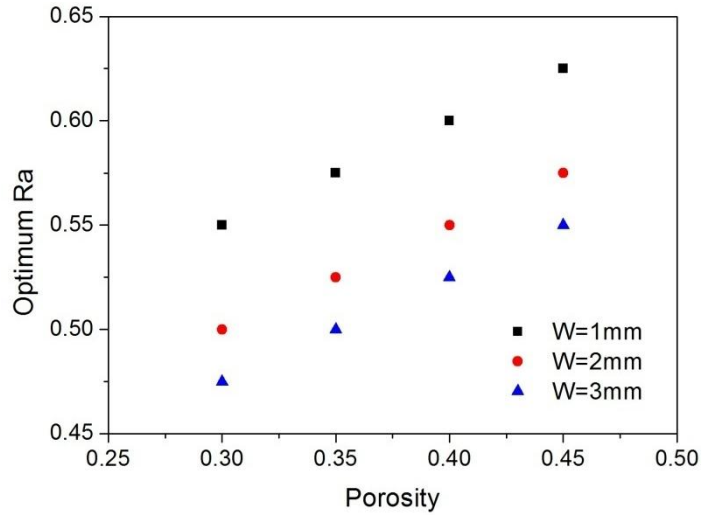

(a)

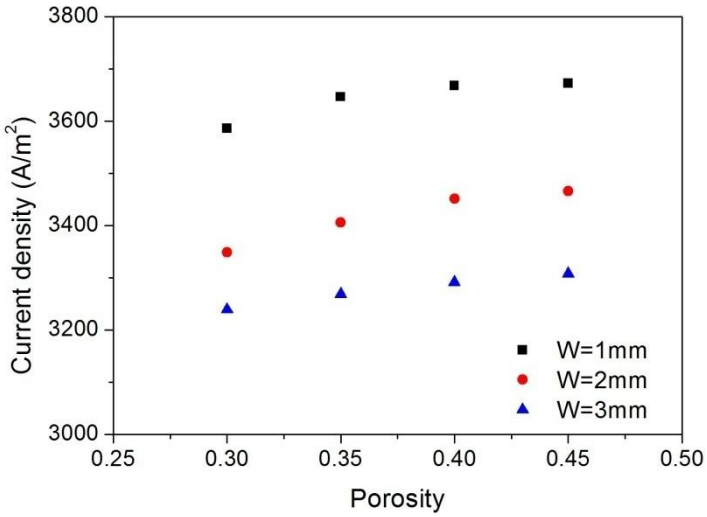

(b)

Figure 5.14 (a) Effect of cathode porosity on optimum Ra, (b) current density of SOFC stack with different cathode porosity and corresponding optimum Ra

However, the gas diffusion resistance will be decreased when porosity increases because the effective gas diffusion coefficient is increasing with porosity (referring to Eqs.(2-35) and (2-36)). On one hand, when porosity increases, the increased electron conducting resistance prefers larger interconnect

rib width to balance the increased ohmic loss. On the other hand, the decreased gas diffusion resistance has some space for interconnect rib width to become larger. Therefore, the optimum Ra increases with the cathode porosity increasing as shown in Fig.5.14(a) and there is linear relationship between the optimum Ra and the cathode porosity.

5.2.5 Optimum rib width Ra_a and Ra_c for stacks with asymmetric geometries

Asymmetric geometric design in methane fed SOFC stack is also considered. Referring to Section 4.2.5, the improvement by this asymmetric geometry may also not be obvious because of high anode concentration overpotential. This can also be proved by the simulated results as shown in Fig.5.15(b). It shows that the asymmetric geometric design can improve methane fed SOFC stack by 1.3% compared to symmetric design. However, this improvement extent by adopting asymmetric geometry in syngas fed SOFC stack is much smaller than that in hydrogen fed SOFC stack.

Similarly to hydrogen or syngas fed SOFC stack, the optimum Ra_a^{asym} is larger than the optimum Ra_a^{sym} and the optimum Ra_c^{asym} is smaller than the optimum Ra_c^{sym}. Also, the SOFC stack achieves best performance when both of optimum anode rib width Ra_a^{asym} and cathode rib width Ra_c^{asym} are utilized in

SOFC stack.

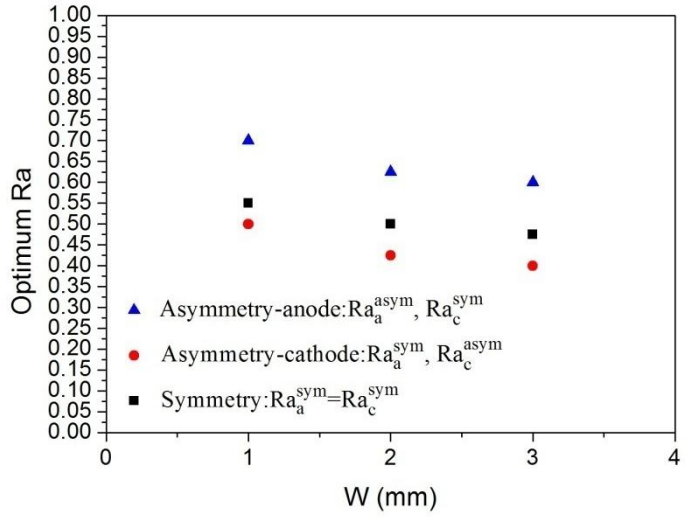

(a)

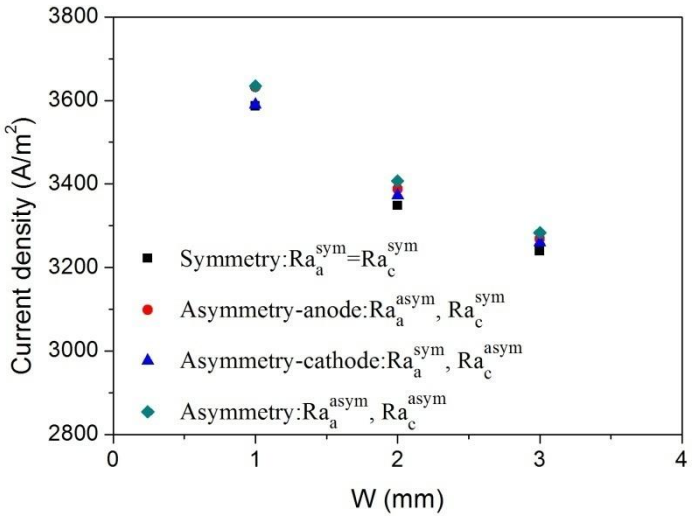

(b)

Figure 5.15 (a) Optimum Ra versus pitch width W for SOFC stacks with symmetric or asymmetric designs, (b) current density of SOFC stacks with corresponding Optimum Ra

5.2.6 Empirical equations for predicting optimum Ra

Basing on the above parametric studies, the optimum Ra is mainly dependent on pitch width, cathode porosity and ASR. Empirical equations are derived and written as follows

$$\mathrm{Ra} = \begin{cases} -0.05\mathrm{W} + 0.25\varepsilon_c - 5\mathrm{ASR} + 0.775, & \text{for W} \le 2.5\ \text{mm} \\ 0.65 + 0.25\varepsilon_c - 5\mathrm{ASR}, & \text{for W} > 2.5mm \end{cases} \quad (5\text{-}1)$$

where W in mm and ASR in $\Omega\,\mathrm{cm}^2$ are required and ε_c is cathode porosity.

Similarly, for methane fed SOFC stack with asymmetric design, the optimum Ra can be estimated by

$$\mathrm{Ra_a} = \begin{cases} -0.1\mathrm{W} + 0.25\varepsilon_c - 5\mathrm{ASR} + 1, & \text{for W} \le 2.5\ \text{mm} \\ 0.75 + 0.25\varepsilon_c - 5\mathrm{ASR}, & \text{for W} > 2.5mm \end{cases} \quad (5\text{-}2a)$$

$$\mathrm{Ra_c} = \begin{cases} -0.05\mathrm{W} + 0.25\varepsilon_c - 5\mathrm{ASR} + 0.7, & \text{for W} \le 2.5\ \text{mm} \\ 0.575 + 0.25\varepsilon_c - 5\mathrm{ASR}, & \text{for W} > 2.5mm \end{cases} \quad (5\text{-}2b)$$

5.3 Conclusions

The modeling of methane fed planar SOFC stack fed with internal reforming reaction is conducted in this chapter. As existence of interconnect rib in SOFC stack, both of the gas diffusion and electron conducting are influenced. Parametric studies are conducted in order to optimize interconnect rib width.

(1) In methane fed SOFC stack with internal reforming, the optimum Ra is linear with pitch width W for W≤ 2.5mm, while the optimum Ra is constant for W>2.5mm.

(2) The optimum Ra is increasing with ASR and the relationship between the optimum Ra and ASR is approximated to be linear.

(3) The optimum Ra is constant on gas composition except for the case

that $x_{CH4}: x_{H_2O} = 1$. However, this influence can be neglected considering that this CH_4 molar fraction of 0.5 is almost the limit condition for preventing carbon deposition.

(4) The optimum Ra is increased with the cathode porosity increasing and there is linear relationship between the optimum Ra and the cathode porosity.

(5) Compared to symmetric design, the asymmetric geometric design can improve methane fed SOFC stack by 1.3%. However, this improvement extent by adopting asymmetric geometry in syngas fed SOFC stack is much smaller than that in hydrogen fed SOFC stack.

(6) Empirical equations are obtained to predict optimum Ra of methane fed SOFC stack, which provides an easy-to-use method for practical geometric designs of syngas fed SOFC stack.

CHAPTER 6 THERMODYNAMIC ANALYSIS OF METHANE-FED SOFC WITH INTERNAL REFORMING

In this chapter, a thermodynamic analysis of methane fed SOFC with oxygen conducting electrolyte and proton conducting electrolyte was conducted. In this study, we not only consider the H_2 electrochemical reaction but CO electrochemical reaction in O-SOFC. This study gives further insight to the methane fed SOFC fabricated with different types of electrolyte.

6.1 Model development

The working principles of H-SOFC and O-SOFC with methane as fuel are summarized in Figs.6.1(a) and 6.1(b), respectively. Both of H-SOFC and O-SOFC are supplied by the mixture of CH_4 and H_2O in anode and air in cathode. Note that the mole ratio of CH_4 and H_2O is 1:2. It is assumed that the methane reacts with water as direct internal reforming (DIR) and then water reacts with CO as water gas shift reaction (WGSR) in anode electrode, written in Eq.(6-1) and (6-2) respectively:

$$CH_4 + H_2O \leftrightarrow 3H_2 + CO \quad (6\text{-}1)$$

$$CO + H_2O \leftrightarrow H_2 + CO_2 \quad (6\text{-}2)$$

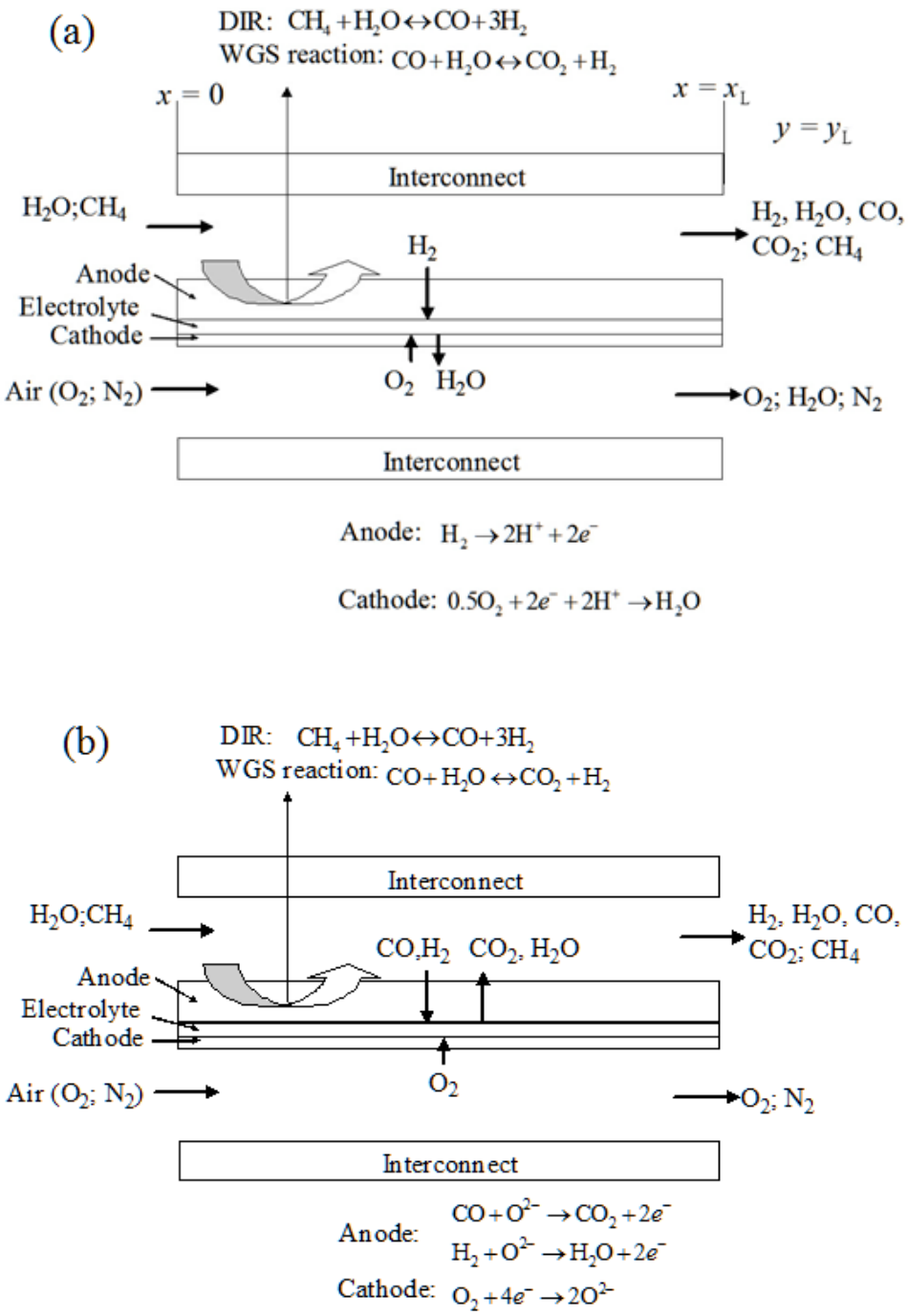

Figure 6.1 Working principle of CH_4-fed SOFC: (a) H-SOFC and (b) O-SOFC

6.1.1 H-SOFC

For the H-SOFC as shown in Fig.6.1(a), H_2 molecules are produced by DIR

and WGSR in the porous anode, and then diffuse toward the interface of anode and electrolyte, where they produces protons and electrons (Eq.(6-3)). Subsequently, protons travel to the cathode side through the proton-conducting electrolyte, while electrons are also transported to the cathode side but via the external circuit. Finally, water steam is produced at the cathode side as oxygen molecules are reduced by the protons and electrons (Eq.(6-4)).

$$H_2 \leftrightarrow 2H^+ + 2e^- \quad (6\text{-}3)$$

$$\frac{1}{2}O_2 + 2H^+ + 2e^- \leftrightarrow H_2O \quad (6\text{-}4)$$

In order to calculate the theoretically thermodynamic efficiency of CH_4 fed SOFCs, the equilibrium potential needs to be evaluated. Based on the thermodynamics of Eqs.(6-3) and (6-4), the equilibrium potential of SOFC can be evaluated:

$$E_{H_2} = E^0_{H_2} + \frac{RT}{2F}\ln\left[\frac{P_{H_2}(P_{O_2})^{0.5}}{P_{H_2O}}\right] \quad (6\text{-}5)$$

where E^0 is the standard equilibrium potential at referenced pressures, representing the Gibbs free energy change of the standard overall fuel cell reaction. P_{H_2}, P_{H_2O}, and P_{O_2} represent the partial pressure (e.g. 0.1 MPa) of H_2 (anode), H_2O (cathode), and O_2 (cathode), respectively, T is reaction temperature (K), R (8.3145 J mol^{-1} K^{-1}) and F (96485 C mol^{-1}) are the ideal gas constant and Faraday constant, respectively.

Therefore, the partial pressures of gas species must be known to calculate

the actual SOFC equilibrium potential. The theoretical calculation of those species partial pressure was already developed in the works of Demin et al. [60] and Assabumrungrat et al.[61], which are adopted in this study: The WGSR and DIR are assumed at equilibrium state due to their fast kinetics, so that the equilibrium constants [60, 61] of WGSR and DIR can be used to calculate the amount of gas species reacted. Considering electrochemical reaction together with DIR and WGSR, the mole number (n) of each gas component at the outlet of SOFC can be formulated as:

Anode outlet:

$$n_{\mathrm{CH_4}} = a - x \tag{6-6}$$

$$n_{\mathrm{CO_2}} = y \tag{6-7}$$

$$n_{\mathrm{H_2}} = 3x + y - c \tag{6-8}$$

$$n_{\mathrm{CO}} = x - y \tag{6-9}$$

$$n_{\mathrm{H_2O}} = b - x - y \tag{6-10}$$

Cathode outlet:

$$n_{\mathrm{H_2O}} = c \tag{6-11}$$

$$n_{\mathrm{O_2}} = d - 0.5c \tag{6-12}$$

where a=1/3, b=2/3, and d = 0.21 respectively denote the mole numbers of CH_4, H_2O, and O_2 at the gas inlets. The letter c is the molar amount of H_2 that is electrochemically consumed (related to current generated and H_2 utilization). x and y are the reacted number of molar DIR and WGSR respectively, of which the

equilibrium constants are below:

$$K_{\mathrm{CH_4}} = \frac{(P_{\mathrm{H_2}})^3 \cdot P_{\mathrm{CO}}}{P_{\mathrm{CH_4}} \cdot P_{\mathrm{H_2O}}} \tag{6-13}$$

$$K_{\mathrm{CO}} = \frac{P_{\mathrm{CO_2}} \cdot P_{\mathrm{H_2}}}{P_{\mathrm{CO}} \cdot P_{\mathrm{H_2O}}} \tag{6-14}$$

The gas partial pressures can be easily calculated from Eq.(6-6) to Eq.(6-12). Another way to calculate equilibrium constants is based on Gibbs change:

$$K = \exp\left(-\frac{\Delta G_{\mathrm{f}}}{RT}\right) \tag{6-15}$$

where ΔG_{f} is the Gibbs energy change of chemical reactions between products and reactants at standard state.

Accordingly, the partial pressures of all gaseous species can be obtained by solving the mass balance equations and the equilibrium equations as mentioned. Details on the calculation procedure can be found in [60, 61, 63] Then the SOFC equilibrium potential is calculated using Eq.(6-5). Therefore, the theoretical work output (W) can also be obtained:

$$W = qE \tag{6-16}$$

where q is the sum of generated electrical charge via electrochemical reactions in SOFC. The maximum efficiency (η) of CH_4 fed SOFC is defined as the ratio of the theoretical work output (W) to the standard formation enthalpy of CH_4:

$$\eta(\%) = \frac{W}{-\Delta H^0} \times 100\% \tag{6-17}$$

For H-SOFC, the efficiency is footnoted as $\eta_{\mathrm{H-SOFC}}$. The fuel utilization is the molar percentage of reacted CH_4 to the inputted CH_4, x/a, and the oxygen

utilization as 0.5*c*/*d* by similar definition.

6.1.2 O-SOFC

Differently in the O-SOFC, O_2 molecules firstly diffuse through the porous cathode, and then react with electrons, producing oxygen ions at the cathode-electrolyte interface (Eq.(6-18)). The produced oxygen ions are further conducted through the dense electrolyte layer to the anode-electrolyte interface. At the anode side, the H_2 and CO molecules both diffuse through the porous anode layer to the anode-electrolyte interface where they meet with oxygen ions and produce H_2O, CO_2 and electrons, as shown in Eqs.(6-19) and (6-20).

$$\frac{1}{2}O_2 + 2e^- \leftrightarrow O^{2-} \tag{6-18}$$

$$H_2 + O^{2-} \leftrightarrow H_2O + 2e^- \tag{6-19}$$

$$CO + O^{2-} \leftrightarrow CO_2 + 2e^- \tag{6-20}$$

It is notably that both H_2 and CO participate in the electrochemical reactions for power generation in O-SOFC. As the H_2O generation site in O-SOFC is the anode side, different from that of H-SOFC, the partial pressure of H_2O in the anode should be used to calculate the Nernst potential for H_2 electrochemical oxidation by Eq.(6-5), Besides, the effect of Nernst potential for electrochemical oxidation of CO should also be considered, defined as:

$$E_{CO} = E^0_{CO} + \frac{RT}{2F}\ln\left[\frac{P_{CO}\,(P_{O_2})^{0.5}}{P_{CO_2}}\right] \tag{6-21}$$

where E^0_{CO} is the standard equilibrium potential.

The electricity output from O-SOFC can be evaluated by adding energy from CO electrochemical oxidation and H_2 electrochemical oxidation:

$$W = q_{co} E_{co} + q_{H_2} E_{H_2} \quad (6\text{-}22)$$

where q_{co} is the electrical current generated by CO electrochemical reaction. The maximum efficiency of O-SOFC (η_{O-SOFC}) can be also defined by Eq.(6-17) with the corresponding W from Eq.(6-22).

The reaction rate of CO electrochemical oxidation in O-SOFC can be evaluated as $r \cdot c$, where r is the ratio of CO oxidation rate to its counterpart: the H_2 oxidation rate (c). According to experimental results of Matsuzaki and Yasuda [31], the H_2 electrochemical oxidation rate is about 1-2 times higher than that of CO electrochemical oxidation. Thus, the value of r in this study is reasonably set to be 0 to 1/3. When r equals to 0, it means that the contribution from CO to the electrochemical reaction is neglected, making the present study reduced to the previous analyses [61].

In order to determine the gas partial pressures in the O-SOFC, the approach for H-SOFC is similarly adopted. The effects of electrochemical reactions, DIR and WGSR on the molar fractions are all fully considered by setting unknown parameters: x and y, and solved by Eqs.(6-6)-(6-10) and Eqs.(6-23)-(6-27) in a

coupled manner:

Anode side:

$$n_{\mathrm{CH_4}} = a - x \tag{6-23}$$

$$n_{\mathrm{CO_2}} = y + rc \tag{6-24}$$

$$n_{\mathrm{H_2}} = 3x + y - c \tag{6-25}$$

$$n_{\mathrm{CO}} = x - y - rc \tag{6-26}$$

$$n_{\mathrm{H_2O}} = b - x - y + c \tag{6-27}$$

Cathode side:

$$n_{\mathrm{O_2}} = d - 0.5c - 0.5rc \tag{6-28}$$

6.2 Solution of models

The model is established based on previous thermodynamic studies [60, 61, 63]. The methodology details can be referred to [61, 63]. The number of moles of H_2O (*b*), CH_4 (*a*), and O_2 (*d*) are specified as the inlet condition. The unknowns *x* and *y* are the reaction extent of the steam reforming and water gas shift reactions, which comply with the reaction equilibrium assumption. In the model, the 20% oxygen utilization factor ((0.5*c*+0.5*rc*)/*d* for O-SOFC and 0.5*c*/*d* for H-SOFC) is assumed with a varying fuel utilization factor *x*/*a* to calculate the maximum theoretically efficiency [60, 61, 63].

6.3 Results and discussion

In this part, the maximum efficiencies of H-SOFC and O-SOFC fed with

CH_4 are compared by parametric simulation. The operating temperature (T) and the oxidation rate ratio of CO to H_2 (r) are varied to investigate their effects on the efficiencies.

6.3.1 Effect of *r*

To investigate the effect of the oxidation rate ratio of CO to H_2 (r) on O-SOFC efficiency, performance simulations are conducted with r changes from 0 to 1/3. During calculation, the operating temperature is fixed as 873K and the oxygen utilization factor is set as 20%. As shown in Fig.6.2, when the electrochemical oxidation of CO is not considered (r=0), the maximum efficiency of H-SOFC is higher than that of O-SOFC, which is in agreement with the previous analysis results in [60]. This is because in H-SOFC water steam is generated in the cathode side thus water will not dilute the hydrogen fuel in the anode side. On the contrary, water is generated in the anode side in O-SOFC. Therefore, the hydrogen concentration in the anode of H-SOFC is higher than that of O-SOFC, which leads to a higher Nernst potential and further a higher maximum efficiency in H-SOFC. However, when the electrochemical oxidation of CO is considered in O-SOFC (r larger than 0), more electricity can be generated through the electrochemical reactions shown in Eq.(6-22). At such situations, the maximum efficiency of O-SOFC is always higher than that of

H-SOFC, even when *r* is only 1/6. Besides, as *r* increases, the advantage of O-SOFC increases, because more CO is involved in the electrochemical reactions in O-SOFC. This finding differs from our common knowledge that H-SOFC always has a higher maximum efficiency than O-SOFC [59-61, 63, 89, 90]. In addition, at high fuel utilization, the efficiency advantage of O-SOFC over H-SOFC becomes more obvious, because more CO electrochemical oxidation is involved. This finding is consistent with literature results in [60, 63].

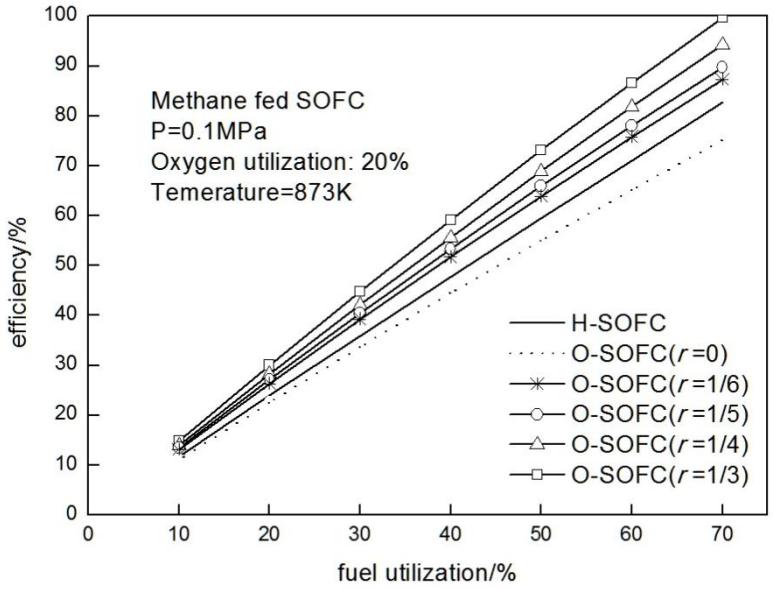

Figure 6.2 Maximum efficiencies of H-SOFC and O-SOFC with different *r*

6.3.2 Effect of *T*

To investigate the effect of operating temperature (*T*) on the maximum efficiencies of H-SOFC and O-SOFC, *T* is changed from 873 K to 1273 K. As shown in Fig.6.3, as *T* increases, the maximum efficiencies decrease, especially at high fuel utilizations. This is because at a high operating temperature, the

equilibrium potentials at standard pressure ($E^0_{H_2}$ and E^0_{CO}) decrease, which in turn causes the decrease of cell efficiency at given fuel utilization.

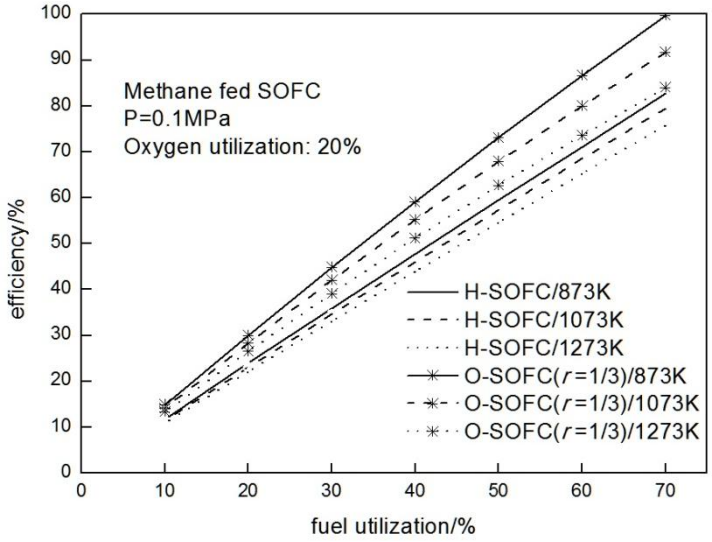

Figure 6.3 Efficiencies of at different *T*

For a better understanding of the difference between O-SOFC and H-SOFC, the efficiency differences ($\eta_{H-SOFC} - \eta_{O-SOFC}$) between H-SOFC and O-SOFC are calculated, as shown in Fig.6.4. When r = 0, ($\eta_{H-SOFC} - \eta_{O-SOFC}$) increases with increasing T and fuel utilization. The maximum efficiency difference can be up to 13% with fuel utilization rate of 70%, which is consistent with results in [59] and [91]. However, as shown in Fig.6.4(b), when r=1/3, ($\eta_{O-SOFC} - \eta_{H-SOFC}$) still increases with increasing fuel utilization, but decreases with increasing *T*. The possible reason for this behavior is that H-SOFC generates more current from hydrogen electrochemical oxidation than O-SOFC at a higher operating temperature (as shown in Fig.6.4(a)), which tends to diminish the difference between O-SOFC and H-SOFC (as shown in

Fig.6.4(b)).

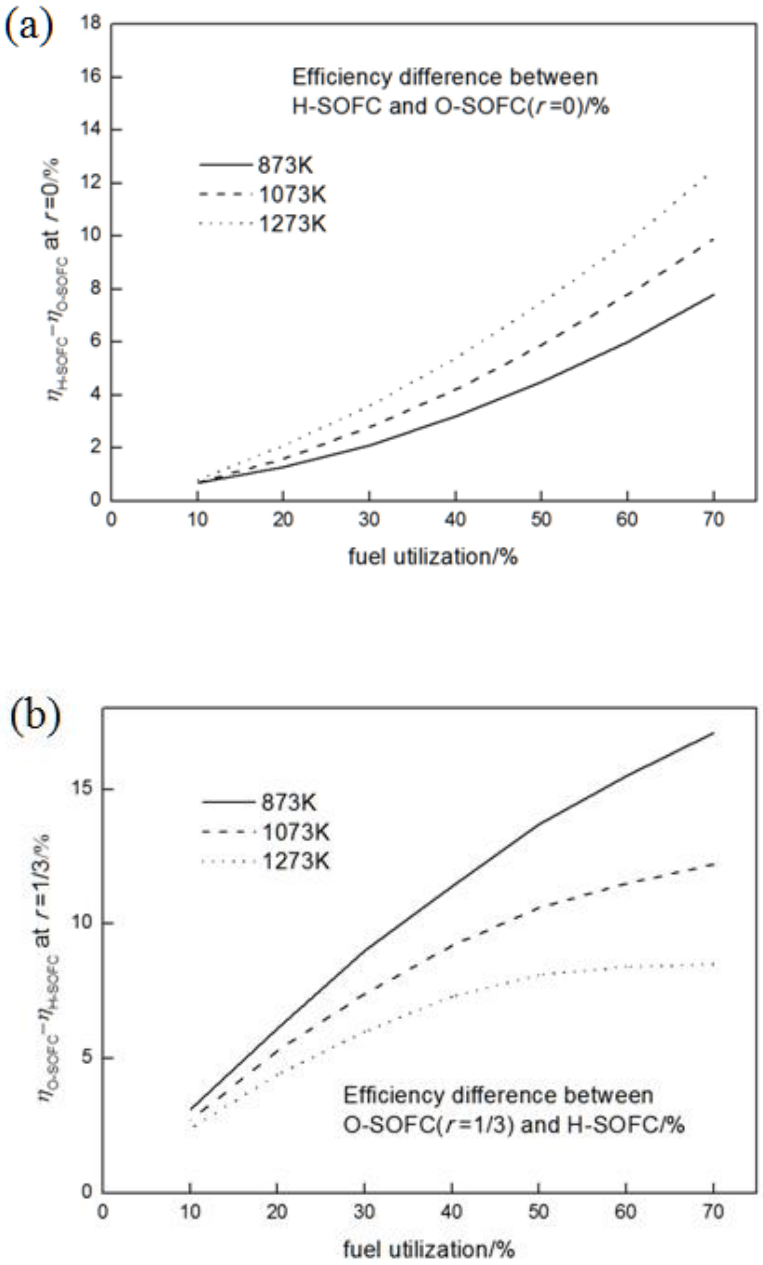

Figure 6.4 Efficiency difference between H-SOFC and O-SOFC:

(a) $\eta_{\mathrm{H-SOFC}} - \eta_{\mathrm{O-SOFC}}$ at r = 0; (b) $\eta_{\mathrm{O-SOFC}} - \eta_{\mathrm{H-SOFC}}$ at r = 1/3

6.4 CONCLUSIONS

To investigate the maximum efficiencies of methane fed H-SOFC and

O-SOFC, a thermodynamic analysis is conducted considering CO electrochemical reaction in O-SOFC. It is revealed that the maximum efficiency of H-SOFC is higher than that of O-SOFC when CO electrochemical reaction in O-SOFC is neglected, which is identical to the results in the previous literature. However, when CO electrochemical reaction in O-SOFC is involved, O-SOFC has higher maximum efficiency than H-SOFC. In addition, the efficiency difference between O-SOFC and H-SOFC increased with the increase of the reaction rate of CO electrochemical reaction and fuel utilization. Moreover, both of the maximum efficiencies of H-SOFC and O-SOFC decrease as temperature increasing. It is also revealed that the value of $(\eta_{\mathrm{H-SOFC}} - \eta_{\mathrm{O-SOFC}})$ increases at r = 0 while the value of $(\eta_{\mathrm{O-SOFC}} - \eta_{\mathrm{H-SOFC}})$ decreases at r = 1/3 when the temperature increases.

CONCLUSIONS

This research work consists of two main parts. In the first part, the study objective is to investigate the effect of interconnect geometry on the SOFC stack performance. As SOFC can be operated using varieties of fuels (i.e. hydrogen, hydrocarbons…) due to its high operating temperature, the mechanisms of involved electrochemical reactions and chemical reactions (if any) in SOFC's porous anode depends heavily on the fuel type. Therefore, the first part of the thesis discusses the three different fueled SOFC stacks using H_2, syngas and methane, respectively. In the second part, a primary thermodynamic study on methane fed SOFC with different electrolytes considering different mechanism of electrochemical reactions is conducted. Conclusions of these two parts are summarized below:

Part 1: A comprehensive three-dimensional model of planar SOFC is developed and validated in **Chapter 2**. This 3D model involves electrochemical reactions, electrons and ions transport, mass transport, gas diffusion, chemical reactions (if any) and heat transfer. In **Chapter 3**, this 3D model is used to investigate the effect of interconnect geometry on the hydrogen fed SOFC stack performance. This 3D model is further validated in H_2 fed stack case, by the comparison of the optimum Ra values between the current model and other

researcher's simulation works under the isothermal assumption. The effect of main affecting factors (pitch width, gas inlet flow rate, ASR and cathode porosity) on the optimum Ra is investigated by series of parametric studies. It is found that when W=2mm, the optimum Ra is 0.5. The optimum Ra is in a linear relation with the pitch width W when W $\leqslant$ 2.5mm, while the optimum Ra is constant when W > 2.5mm. The optimum Ra is increasing with ASR and the relationship between the optimum Ra and ASR can also be approximated to be linear. In addition, the optimum Ra is increased with the increase of cathode porosity and there is linear relationship between the optimum Ra and the cathode porosity. Moreover, a novel asymmetric geometry design of interconnect rib in SOFC stack fed by H_2 is proposed considering the difference of gas diffusion coefficient between gas species in anode side and cathode side respectively. The modeling results indicate that the stack performance can greatly benefit from this novel asymmetric geometry design and the improvement of stack performance can be as high as 7% compared to symmetric design. Based on the parametric studies, empirical equations are derived for predicting optimum Ra values, which provide an easy-to-use guideline for practical geometric designing of SOFC stack. To generalize the results of optimum Ra for stacks with different fuels, SOFC stacks fed by syngas and by methane with internal reforming are also conducted in

Chapter 4 and **Chapter 5**, respectively. It is comparative between H_2 fed SOFC stack and syngas fed SOFC stack because the same operating conditions are utilized. The relations between the optimum Ra and main factors (pitch width, cathode porosity, ASR) in syngas fed SOFCs are found to be similar to that in H_2 fed SOFCs. However, when W=2mm, the optimum Ra for syngas fed SOFC stacks is 0.475 which is lower than that for H_2 fed SOFC stacks. In **Chapter 5,** the optimum Ra of methane fed SOFC stack with internal reforming is investigated. In this study, considering the rate of methane steam reforming, the operating temperature is 800℃ which is higher than that of 700℃ utilized in previous two studies. The modeling results show that the optimum Ra is 0.5 for W=2mm. Moreover, parametric studies indicate the optimum Ra is linearly increasing with ASR and cathode porosity. Asymmetric geometric design is also discussed. This design can also improve stack performance compared to symmetric geometric design. However, this improvement in syngas or methane fed SOFC stack is much smaller than that in hydrogen fed SOFC stack. Empirical equations are also derived to predict optimum Ra values.

Part 2: A simple thermodynamic modeling is conducted to investigate the difference between methane fed H-SOFC and O-SOFC with internal reforming considering different mechanism of electrochemical reactions in porous anode. It

is revealed that the maximum efficiency of H-SOFC is higher than that of O-SOFC when CO electrochemical reaction in O-SOFC is neglected, which is identical to the results in the previous literature. However, when CO electrochemical reaction in O-SOFC is involved, O-SOFC has higher maximum efficiency than H-SOFC. In addition, the efficiency difference between O-SOFC and H-SOFC increased with the increase of the reaction rate of CO electrochemical reaction and fuel utilization. Moreover, both of the maximum efficiencies of H-SOFC and O-SOFC decrease as temperature increasing.

REFERENCES

[1] Brewer WD, Wengenmayr R, Bührke T. Renewable Energy: Sustainable Energy Concepts for the Energy Change: John Wiley & Sons; 2013.
[2] Grove WR. Philos Mag. 1839;14:4.
[3] Nernst WZ. Electrochem. 1899;6:3.
[4] Baur E, Presis H. Electrochem. 1937;43:6.
[5] EG&G Technical Services I. Fuel Cell Handbook (Seventh Edition)2004.
[6] FuelCellToday. The Fuel Cell Industry Review 2013. 2013.
[7] Kee RJ, Korada P, Walters K, Pavol M. A generalized model of the flow distribution in channel networks of planar fuel cells. Journal of Power Sources. 2002;109:148-59.
[8] Recknagle KP, Williford RE, Chick LA, Rector DR, Khaleel MA. Three-dimensional thermo-fluid electrochemical modeling of planar SOFC stacks. Journal of Power Sources. 2003;113:109-14.
[9] Huang CM, Shy SS, Lee CH. On flow uniformity in various interconnects and its influence to cell performance of planar SOFC. Journal of Power Sources. 2008;183:205-13.
[10] Chen D, Zeng Q, Su S, Bi W, Ren Z. Geometric optimization of a 10-cell modular planar solid oxide fuel cell stack manifold. Applied Energy. 2013;112:1100-7.
[11] Lin B, Shi Y, Ni M, Cai N. Numerical investigation on impacts on fuel velocity distribution nonuniformity among solid oxide fuel cell unit channels. International Journal of Hydrogen Energy. 2015;40:3035-47.
[12] Wang G, Yang Y, Zhang H, Xia W. 3-D model of thermo-fluid and electrochemical for planar SOFC. Journal of Power Sources. 2007;167:398-405.
[13] Xia W, Yang Y, Wang Q. Effects of operations and structural parameters on the one-cell stack performance of planar solid oxide fuel cell. Journal of Power Sources. 2009;194:886-98.
[14] Kulikovsky AA. A simple equation for temperature gradient in a planar SOFC stack. International Journal of Hydrogen Energy. 2010;35:308-12.
[15] Yan D, Bin Z, Fang D, Luo J, Wang X, Pu J, et al. Feasibility study of an external manifold for planar intermediate-temperature solid oxide fuel cells stack. International Journal of Hydrogen Energy. 2013;38:660-6.
[16] Burt AC, Celik IB, Gemmen RS, Smirnov AV. A numerical study of cell-to-cell variations in a SOFC stack. Journal of Power Sources. 2004;126:76-87.

[17] Bi W, Chen D, Lin Z. A key geometric parameter for the flow uniformity in planar solid oxide fuel cell stacks. International Journal of Hydrogen Energy. 2009;34:3873-84.
[18] da Conceição L, Dessemond L, Djurado E, Souza MMVM. Thin films of La0.7Sr0.3MnO3−δ dip-coated on Fe–Cr alloys for SOFC metallic interconnect. International Journal of Hydrogen Energy. 2013;38:15335-47.
[19] Morán-Ruiz A, Vidal K, Larrañaga A, Porras-Vázquez JM, Slater PR, Arriortua MI. Laser machining of LaNi0.6M0.4O3−δ (M: Co, Fe) dip-coated on a Fe–22Cr mesh material to obtain a new contact coating for SOFC: Interaction between Crofer22APU interconnect and La0.6Sr0.4FeO3 cathode. International Journal of Hydrogen Energy. 2015;40:8407-18.
[20] Piccardo P, Anelli S, Bongiorno V, Spotorno R, Repetto L, Girardon P. K44M ferritic stainless steel as possible interconnect material for SOFC stack operating at 600 °C: Characterization of the oxidation behaviour at early working stages. International Journal of Hydrogen Energy. 2015;40:3726-38.
[21] Safikhani A, Esmailian M, Salmani MR, Aminfard M. Effect of Ni–Mo addition on cyclic and isothermal oxidation resistance and electrical behavior of ferritic stainless steel for SOFCs interconnect. International Journal of Hydrogen Energy. 2014;39:11210-23.
[22] Shong W-J, Liu C-K, Wu S-H, Liu H-C, Yang P. Oxidation behavior of nickel coating on ferritic stainless steel interconnect for SOFC application. International Journal of Hydrogen Energy. 2014;39:19737-46.
[23] Stygar M, Brylewski T, Kruk A, Przybylski K. Oxidation properties of ferritic stainless steel in dual Ar–H2–H2O/air atmosphere exposure with regard to SOFC interconnect application. Solid State Ionics. 2014;262:449-53.
[24] Ota T, Koyama M, Wen C-j, Yamada K, Takahashi H. Object-based modeling of SOFC system: dynamic behavior of micro-tube SOFC. Journal of Power Sources. 2003;118:430-9.
[25] Wen T-L, Wang D, Tu HY, Chen M, Lu Z, Zhang Z, et al. Research on planar SOFC stack. Solid State Ionics. 2002;152-153:6.
[26] Lin Z, Stevenson JW, Khaleel MA. The effect of interconnect rib size on the fuel cell concentration polarization in planar SOFCs. Journal of Power Sources. 2003;117:92-7.
[27] Liu S, Kong W, Lin Z. Three-dimensional modeling of planar solid oxide fuel cells and the rib design optimization. Journal of Power Sources. 2009;194:854-63.
[28] Bi W, Li J, Lin Z. Flow uniformity optimization for large size planar solid oxide fuel cells with U-type parallel channel designs. Journal of Power Sources. 2010;195:3207-14.

[29] Kong W, Gao X, Liu S, Su S, Chen D. Optimization of the Interconnect Ribs for a Cathode-Supported Solid Oxide Fuel Cell. Energies. 2014;7:295-313.
[30] Andersson M, Paradis H, Yuan J, Sundén B. Three dimensional modeling of an solid oxide fuel cell coupling charge transfer phenomena with transport processes and heat generation. Electrochimica Acta. 2013;109:881-93.
[31] Matsuzaki Y, Yasuda I. Electrochemical Oxidation of H2 and CO in a H2-H2O-CO-CO2 System at the Interface of a Ni-YSZ Cermet Electrode and YSZ Electrolyte. Journal of The Electrochemical Society. 2000;147:6.
[32] Yan XL, Hino R. NUCLEAR HYDROGEN PRODUCTION HANDBOOK: CRC Press; 2011.
[33] Ni M, Leung DYC, Leung MKH. A review on reforming bio-ethanol for hydrogen production. International Journal of Hydrogen Energy. 2007;32:3238-47.
[34] Ni M, Leung MKH, Leung DYC. Theoretical analysis of reversible solid oxide fuel cell based on proton-conducting electrolyte. Journal of Power Sources. 2008;177:369-75.
[35] Dyer PN, Richards RE, Russek SL, Taylor DM. Ion transport membrane technology for oxygen separation and syngas production. Solid State Ionics. 2000;134:21-33.
[36] Rostrup-Nielsen JR. New aspects of syngas production and use. Catalysis Today. 2000;63:159-64.
[37] Wilhelm DJ, Simbeck DR, Karp AD, Dickenson RL. Syngas production for gas-to-liquids applications: technologies, issues and outlook. Fuel Processing Technology. 2001;71:139-48.
[38] Lv P, Yuan Z, Wu C, Ma L, Chen Y, Tsubaki N. Bio-syngas production from biomass catalytic gasification. Energy Conversion and Management. 2007;48:1132-9.
[39] Liu K, Song C, Subramani V. Frontmatter
Hydrogen and Syngas Production and Purification Technologies : Hydrocarbon Processing for H2 Production2009.
[40] Ni M. An electrochemical model for syngas production by co-electrolysis of H2O and CO2. Journal of Power Sources. 2012;202:209-16.
[41] Suwanwarangkul R, Croiset E, Entchev E, Charojrochkul S, Pritzker MD, Fowler MW, et al. Experimental and modeling study of solid oxide fuel cell operating with syngas fuel. Journal of Power Sources. 2006;161:308-22.
[42] Ni M, Leung DYC, Leung MKH. Modeling of methane fed solid oxide fuel cells: Comparison between proton conducting electrolyte and oxygen ion conducting electrolyte. Journal of Power Sources. 2008;183:133-42.

[43] Ni M. Modeling of SOFC running on partially pre-reformed gas mixture. International Journal of Hydrogen Energy. 2012;37:1731-45.
[44] Demin AK, Tsiakaras PE, Sobyanin VA, Hramova SY. Thermodynamic analysis of a methane fed SOFC system based on a protonic conductor. Solid State Ionics. 2002;152–153:555-60.
[45] Peters R, Dahl R, Stolten D. Internal reforming of methane in solid oxide fuel cell systems. Journal of Power Sources. 2002;106:7.
[46] Janardhanan VM, Deutschmann O. CFD analysis of a solid oxide fuel cell with internal reforming: Coupled interactions of transport, heterogeneous catalysis and electrochemical processes. Journal of Power Sources. 2006;162:1192-202.
[47] Zhu H, Kee RJ. Modeling Electrochemical Impedance Spectra in SOFC Button Cells with Internal Methane Reforming. Journal of The Electrochemical Society. 2006;153:A1765.
[48] Ivanov P. Thermodynamic modeling of the power plant based on the SOFC with internal steam reforming of methane. Electrochimica Acta. 2007;52:3921-8.
[49] Laosiripojana N, Assabumrungrat S. Catalytic steam reforming of methane, methanol, and ethanol over Ni/YSZ: The possible use of these fuels in internal reforming SOFC. Journal of Power Sources. 2007;163:943-51.
[50] Nikooyeh K, Jeje AA, Hill JM. 3D modeling of anode-supported planar SOFC with internal reforming of methane. Journal of Power Sources. 2007;171:601-9.
[51] Li J, Kang Y-W, Cao G-Y, Zhu X-J, Tu H-Y, Li J. Nonlinear identification of a DIR-SOFC stack using wavelet networks. Journal of Power Sources. 2008;179:673-82.
[52] Sanchez D, Chacartegui R, Munoz A, Sanchez T. On the effect of methane internal reforming modelling in solid oxide fuel cells. International Journal of Hydrogen Energy. 2008;33:1834-44.
[53] Zhu H, Kee RJ. Two-dimensional model of distributed charge transfer and internal reforming within unit cells of segmented-in-series solid-oxide fuel cells. Journal of Power Sources. 2011;196:7654-64.
[54] Park J, Li P, Bae J. Analysis of chemical, electrochemical reactions and thermo-fluid flow in methane-feed internal reforming SOFCs: Part I – Modeling and effect of gas concentrations. International Journal of Hydrogen Energy. 2012;37:8512-31.
[55] Wang S, Worek WM, Minkowycz WJ. Performance comparison of the mass transfer models with internal reforming for solid oxide fuel cell anodes. International Journal of Heat and Mass Transfer. 2012;55:3933-45.

[56] Wang Y, Yoshiba F, Kawase M, Watanabe T. Performance and effective kinetic models of methane steam reforming over Ni/YSZ anode of planar SOFC. International Journal of Hydrogen Energy. 2009;34:3885-93.
[57] Yang Y, Du X, Yang L, Huang Y, Xian H. Investigation of methane steam reforming in planar porous support of solid oxide fuel cell. Applied Thermal Engineering. 2009;29:1106-13.
[58] Ni M, Leung M, Leung D. Mathematical Modelling of Proton-Conducting Solid Oxide Fuel Cells and Comparison with Oxygen-Ion-Conducting Counterpart. Fuel Cells. 2007;7:269-78.
[59] Demin A. Thermodynamic analysis of a hydrogen fed solid oxide oxide fuel cell based on a proton conductor. International Journal of Hydrogen Energy. 2001.
[60] Demin AK, Tsiakaras PE, Sobyanin VA, Hramova SY. Thermodynamic analysis of a methane fed SOFC system based on a protonic conductor.pdf. Solid State Ionics. 2002;152-153:5.
[61] Assabumrungrat S, Pavarajarn V, Charojrochkul S, Laosiripojana N. Thermodynamic analysis for a solid oxide fuel cell with direct internal reforming fueled by ethanol. Chemical Engineering Science. 2004;59:6015-20.
[62] Jamsak W, Assabumrungrat S, Douglas P, Laosiripojana N, Charojrochkul S. Theoretical performance analysis of ethanol-fuelled solid oxide fuel cells with different electrolytes. Chemical Engineering Journal. 2006;119:11-8.
[63] Ni M, Leung DYC, Leung MKH. Electrochemical modeling of ammonia-fed solid oxide fuel cells based on proton conducting electrolyte. Journal of Power Sources. 2008;183:687-92.
[64] Haanappel VAC, Batfalsky P, Gross SM, de Haart LGJ, Malzbender J, Menzler NH, et al. A Comparative Study Between Resistance Measurements in Model Experiments and Solid Oxide Fuel Cell Stack Performance Tests. Journal of Fuel Cell Science and Technology. 2006;4:11-8.
[65] O'Hayre R, Cha S-W, Colella W, Prinz BF. Fuel Cell Fundamentals2006.
[66] Ni M. Electrolytic effect in solid oxide fuel cells running on steam/methane mixture. Journal of Power Sources. 2011;196:2027-36.
[67] Aguiar P, Adjiman CS, Brandon NP. Anode-supported intermediate temperature direct internal reforming solid oxide fuel cell. I: model-based steady-state performance. Journal of Power Sources. 2004;138:120-36.
[68] Andersson M, Yuan J, Sundén B. SOFC modeling considering electrochemical reactions at the active three phase boundaries. International Journal of Heat and Mass Transfer. 2012;55:773-88.

[69] Patcharavorachot Y, Arpornwichanop A, Chuachuensuk A. Electrochemical study of a planar solid oxide fuel cell: Role of support structures. Journal of Power Sources. 2008;177:254-61.
[70] Costamagna P, Costa P, Antonucci V. Micro-modelling of solid oxide fuel cell electrodes. Electrochimica Acta. 1998;43:375-94.
[71] Chen D, Lin Z, Zhu H, Kee RJ. Percolation theory to predict effective properties of solid oxide fuel-cell composite electrodes. Journal of Power Sources. 2009;191:240-52.
[72] Sanyal J, Goldin GM, Zhu H, Kee RJ. A particle-based model for predicting the effective conductivities of composite electrodes. Journal of Power Sources. 2010;195:6671-9.
[73] Bouvard D, Lange FF. Relation between percolation and particle coordination in binary powder mixtures. Acta Metallurgica et Materialia. 1991;39:3083-90.
[74] Hussain MM, Li X, Dincer I. Mathematical modeling of planar solid oxide fuel cells. Journal of Power Sources. 2006;161:1012-22.
[75] Ferguson JR, Fiard JM, Herbin R. Three-dimensional numerical simulation for various geometries of solid oxide fuel cells. Journal of Power Sources. 1996;58:14.
[76] Hentall PL, Lakeman JB, Mepsted GO, Adcock PL, Moore JM. New materials for polymer electrolyte membrane fuel cell current collectors. Journal of Power Sources. 1999;80:235-41.
[77] Darcy H. Les Fontaines Publiques de la Ville de Dijon1856.
[78] Brinkman HC. A calculation of the viscous force exerted by a flowing fluid on a dense swarm of particles. Flow, Turbulence and Combustion. 1949;1:27-34.
[79] Suwanwarangkul R, Croiset E, Fowler MW, Douglas PL, Entchev E, Douglas MA. Performance comparison of Fick's, dusty-gas and Stefan–Maxwell models to predict the concentration overpotential of a SOFC anode. Journal of Power Sources. 2003;122:9-18.
[80] Veldsink JW, van Damme RMJ, Versteeg GF, van Swaaij WPM. The use of the dusty-gas model for the description of mass transport with chemical reaction in porous media. The Chemical Engineering Journal and the Biochemical Engineering Journal. 1995;57:115-25.
[81] Fuller EN, Schettler PD, Giddings JC. NEW METHOD FOR PREDICTION OF BINARY GAS-PHASE DIFFUSION COEFFICIENTS. Industrial & Engineering Chemistry. 1966;58:18-27.
[82] Ni M. Thermo-electrochemical modeling of ammonia-fueled solid oxide fuel cells considering ammonia thermal decomposition in the anode. International Journal of Hydrogen Energy. 2011;36:3153-66.

[83] Haberman BA, Young JB. Three-dimensional simulation of chemically reacting gas flows in the porous support structure of an integrated-planar solid oxide fuel cell. International Journal of Heat and Mass Transfer. 2004;47:3617-29.
[84] Hussain MM, Li X, Dincer I. Multi-component mathematical model of solid oxide fuel cell anode. International Journal of Energy Research. 2005;29:1083-101.
[85] Todd B, Young JB. Thermodynamic and transport properties of gases for use in solid oxide fuel cell modelling. Journal of Power Sources. 2002;110:186-200.
[86] Kakaç S, Pramuanjaroenkij A, Zhou XY. A review of numerical modeling of solid oxide fuel cells. International Journal of Hydrogen Energy. 2007;32:761-86.
[87] Kim JW, Virkar AV, Fung KZ, Mehta K, Singhal SC. Polarization Effects in Intermediate Temperature, Anode-Supported Solid Oxide Fuel Cells. Journal of The Electrochemical Society. 1999;146:69-78.
[88] Liu S, Song C, Lin Z. The effects of the interconnect rib contact resistance on the performance of planar solid oxide fuel cell stack and the rib design optimization. Journal of Power Sources. 2008;183:214-25.
[89] Sangtongkitcharoen W, Assabumrungrat S, Pavarajarn V, Laosiripojana N, Praserthdam P. Comparison of carbon formation boundary in different modes of solid oxide fuel cells fueled by methane. Journal of Power sources. 2005;142:75-80.
[90] Jamsak W, Assabumrungrat S, Douglas PL, Laosiripojana N, Charojrochkul S. Theoretical performance analysis of ethanol-fuelled solid oxide fuel cells with different electrolytes. Chemical Engineering Journal. 2006;119:11-8.
[91] Demin A, Alderucci V, Ielo I, Fadeev G, Maggio G, Giordano N, et al. Thermodynamic analysis of methane fueled solid oxide fuel cell system. International journal of hydrogen energy. 1992;17:451-8.